Dottorato di Ricerca in Scienze della Terra

Curriculum Geodinamica

Relationships between deep and surface processes in subduction zones: insights from numerical models

Ciclo XXXII

Arthur Briaud

Supervisore
Prof. Franscesca Funiciello
Prof. Claudio Faccenna
Prof. Jeroen van Hunen

Coordinatore Scuola Dottorale
Prof. Paola Tuccimei

Abstract

It is widely accepted that the gravitational instabilities of cold, dense, subducting lithospheres constitute the main driving force for plate tectonics. Unravelling the complex processes of subduction zones which originate from the down-going plate and its interplay with the surrounding mantle remains challenging. Due to the lack of direct observations and measurements of the internal Earth, it is difficult to understand how slabs behave at depth. However, seismological and gravimetric measurements provide indirect evidences about the mantle structure and its movement. On the other hand, petrology and geochemistry provide insights on the composition of the Earth interior. Although, these data may be considered as a snapshot of the ongoing processes. The use of numerical modelling is thus a useful ingredient to provide a dynamic picture of the interior of the Earth, integrating the available indirect observables.

This thesis is focused on: (1) analysing how the surface fingerprint of the upper plate may be affected by the deep slab dynamics, especially once slabs starts to interact with the mantle transition zone. Thanks to 2D numerical models, it is systematically investigated the role of the mantle rheology (Clapeyron slopes and lower mantle viscosity) as well as plate strength (initial thermal age of plates) on the slab dynamics. In the chapter 3, four categories of slab dynamics are found resulting from the combination of the geodynamics variables mentioned above. These slab categories depict that transient slab dynamics (i.e., slab folding, slab avalanche) have a profound impact on the large-scale dynamic topography of the upper plate in time by pulling up and down the upper plate. Additionally, the dynamic topography shows a tilting of the upper plate towards and fromward the trench following the slab folding at depth. (2) 2D numerical outcomes which are exported to the analysis of the Neotethys subduction system, in particular of the central Iran from ~100 to 30 Ma. Results show that the slab folding behaviour into the transition zone is a reasonable scenario for explaining the particular episodic back-arc closure and opening of the central Iran as well as large-marine flooding events in the Eocene and early Miocene, before the onset of the collision. (3) 3D numerical models of subduction with the aim to understand if and how the slab may evolve lateral with simple model of flattening slab into the mantle transition zone. These models demonstrate that the width of the subduction system have an impact on the way that slab propagate down into the mantle in the centre of wide model domain and stagnate on the leading plate edge. Moreover, I highlighted that the lateral

variability of slab morphology from penetrating to stagnation into the mantle transition zone control the dynamic topography of the upper plate. Finally (4) this thesis ends with outlooks about more complex 3D models set-up which may help us to better constrains the lateral variability of deep slab morphology and thus better understand specific surface fingerprints characterizing the natural prototype.

Acknowledgments

First of all, I would like to thank the fourth people that made this thesis possible: Claudio, Francesca, Jeroen and Roberto. Thanks to all of you, it's not easy to find better supervisors and people to work and discuss with. Your enthusiasm and passion for science have been a great source of creativeness as well as motivation to me. Thanks for providing the environment for me to grow up in both professional and personal point of view. I am truly glad to work with you.

Francesca, you always be there, at each time I had a personal issue, a question or some doubts I knew I could ask you. I really thank you for being here during the last three years.

Claudio thank you so much for sharing your wide knowledge about geodynamics, geology and ideas. Talking with you is always a great source of inspiration. I appreciated many times when you were passing in the corridor saying 'Arturo come stai!', that always made me smile.

Jeroen, thanks for the time you put in teaching; your help and patience. Also, thanks for being available for discussions, suggestions when I was at Durham University and after when we were in different countries.

Roberto, it is a special thanks for you. Thanks for your dedication and patience in teaching and helping me about many things. Your help has been essential for me and for this thesis. I enjoyed a lot the time that I spent in Lyon. It has been a fruitful friendship. Also, thanks for being always available for the discussions and suggestions about the professional and personal point of view.

I thank my reviewers, Taras Gerya and Adam Holt whose suggestions helped for improving this thesis.

Most importantly, this thesis has been possible thanks to the SUBITOP network and the computational resources provided by the ARCHER UK National Supercomputing Service. SUBITOP is funding from the European Union's Horizon 2020 research and innovation programme under the Marie Skoldowska-Curie, which involved 10 teams and funded 15 early-stage scientists.

Many thanks to the wonderful friends and people that I found in Rome but also to the Subitopers and Doudou!

A big thank to my family who keeps supporting me and my choices, even though we were far from each other. Also, I enjoyed a lot the time that we spent together when you visited me in Rome.
And, finally, to my brother and sister: Paul, Chloé, I dedicate this thesis.

Table of Contents

Chapter III: Topographic fingerprint of deep mantle subduction

Chapter IV: Deep slab folding and the deformation of the Iranian mobile belt (central Tethys system)

Chapter V: Lateral variability of slab interacting with the mantle transition zone

Chapter VI: Conclusions

Chapter I

Introduction

In this chapter, I present in the first section the general overview on subduction zone. Second, I describe which are the indirect observables that we have to determine to unravel the present-day mantle/slab composition and morphology. This chapter ends by describing the thesis outlines.

1.1 Convergent margins: general features

At lithospheric scale, the seafloor ages are relatively young (<200 Myr) as respect to the age of the Earth (~ 4.5 Ga; Fig. 1.1). This observation led in the 60's to develop the concept of sea-floor spreading (*McKenzie, 1969; Le Pichon, 1968*). This theory considers plate as rigid lids, (e.g., *Gripp & Gordon, 2002; Seton et al., 2012*).

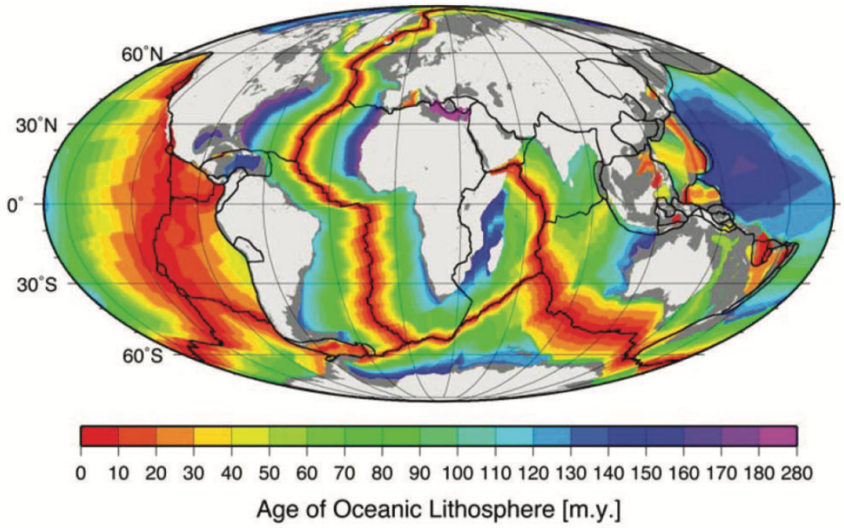

Figure 1.1: Present-day age of the oceanic lithosphere after *Seton et al.* (2012).

However, considering plates as rigid blocks approximate the unavoidable plate deformation. Plates may deform and buckle inland. However, most of the deformation is localized at the plate boundary as mirrored by the strain map of the Earth (Fig. 1.2; *Kreemer, 2003*).

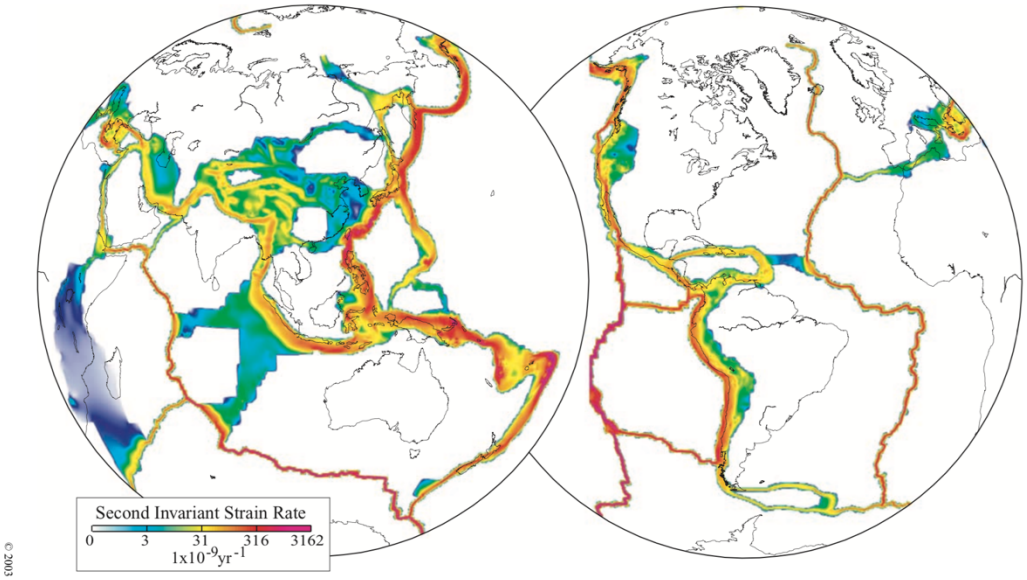

Figure 1.2: Contours of the second invariant of the strain rate field determined using 3000 geodetic velocities world-wide, and Quarternary slip rates in Asia. All white areas are assumed to behave rigidly. The contour scale is quasi-exponential. From *Kreemer* (2003).

If we consider that most of the deformation occur at plate boundaries, divergent margins (i.e., mid-ocean ridges) are considered as the spreading centre. As the oceanic lithosphere moves away from an ocean ridge, it cools, thickens, and becomes denser because of thermal contraction (Fig. 1.3). Even though the rocks of the oceanic crust are positively buoyant compared to the underlying mantle, the colder sub-crustal rocks in the lithosphere become sufficiently dense to make old oceanic lithosphere heavy enough to be gravitationally unstable with respect to the hot mantle. As a result, the oceanic lithosphere founders and begins to sink into the interior of the Earth at ocean trenches (e.g., *King, 2007; Turcotte & Schubert, 2002*). The sink of the oceanic plate in subduction zones are thus, a major component of the dynamic-plate, convecting-mantle system, forming the lid of the top mantle thermal boundary layer of the Earth. Subducting slabs are the thus, a dominant source of gravitational potential energy, that is, the driving force for mantle convection and plate tectonics. (e.g., Fig. 1.3; *Lee & King, 2011*) . In contrast, the ascending mantle convective flow which comes from the hot thermal bottom boundary layer allows the cooling of the Earth's core, leads to release internal radioactivity and participate to drive plate motion (e.g., *Husson, 2012; Turcotte & Schubert, 2002*).

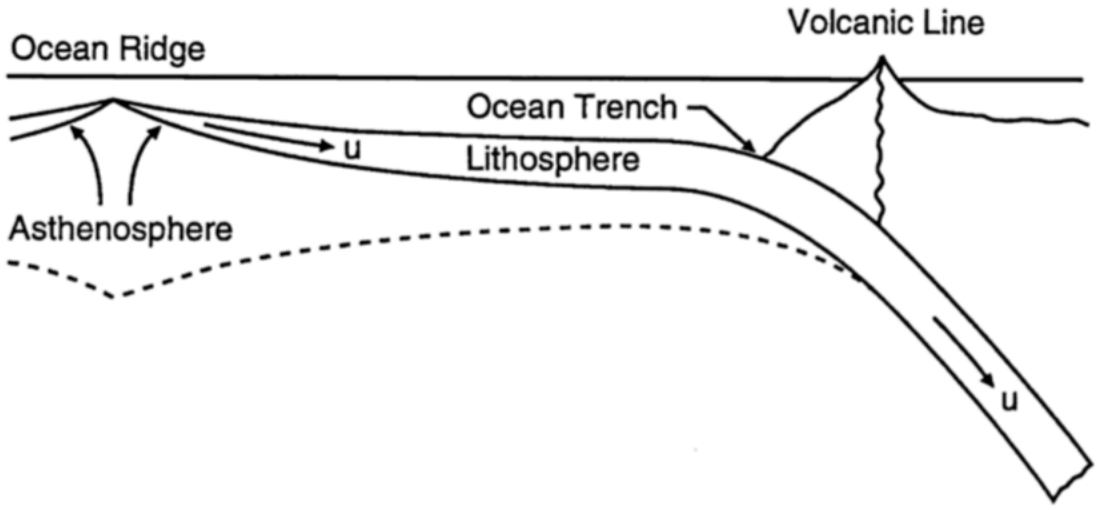

Figure 1.3: Sketch of plate tectonics representing a mid-oceanic ridge and a subduction zone (*Turcotte & Schubert, 2002*).

1.2 Indirect observables of subducting lithosphere

In this section, I introduce some methods which help to figure out the present-day internal structure of the Earth providing indirect observables. First, I introduce how seismology, and in particular tomographic images decipher the shape of slabs and the mantle geometry. Then, I briefly summarize how the geoid signature and the dynamic topography might mirror the processes occurring at depth.

1.2.1 Seismology and tomography

Seismic waves allow to characterize the internal composition of the Earth, but also to determine the major discontinuities at depth. The 1-D PREM model (*Dziewonski & Anderson, 1981*) shows that the mantle density does not increase linearly with depth but instead, increases abruptly (Fig. 1.4). For instance, a density jump is predicted between the upper and lower mantle, of about 300 kg/m^3. In addition, several density jumps are localized into the upper mantle. These jumps may be related to the major phase transitions of minerals.

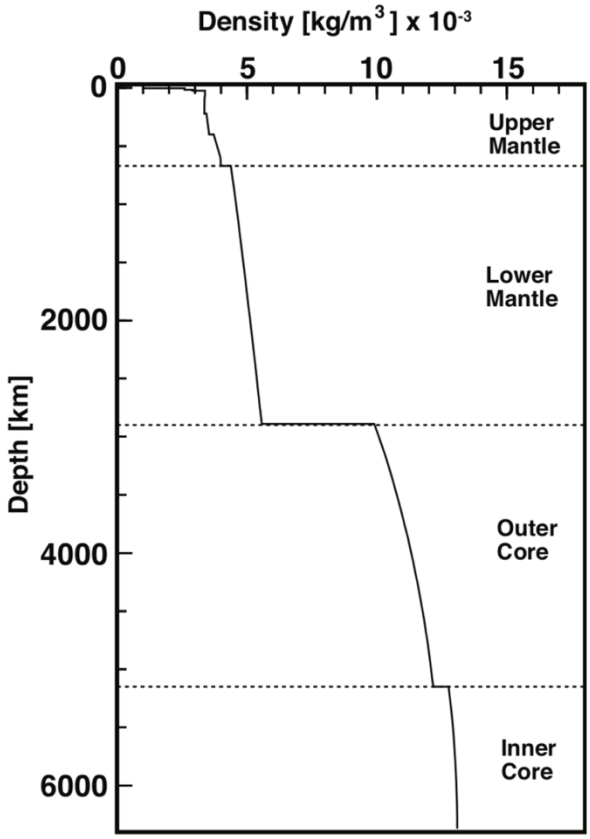

Figure 1.4: Increasing density as function of depth after the PREM model (*Dziewonski & Anderson, 1981*).

Historically, the geometry of slab has been constrained by earthquake hypocenters *(Isacks & Molnar, 1969; Isacks, 1968*). By mapping the hypocenters come out the so called Wadati-Benioff zone of a subduction zone. Wadati-Benioff zones illustrate that slab bend, kink, and thicken (*Gudmundsson & Sambridge, 1998; Hayes, 2012*) highlighting a wide variability of present-day slab geometry (Fig. 1.5). The focal mechanisms allow us to know the subducting inner plate stress field (*Isacks & Molnar, 1971*). At shallow earthquakes depth (60 -300 km depth), slabs are subjected to down-dip extensive stresses while deeper earthquakes (300-700 km) suggest that slabs are progressively under down-dip compressive stresses *(Isacks & Molnar, 1969, 1971*). At about 670 km depth, earthquakes locations suggest that slab may stagnates on the mantle transition zone due to the resisting force of the slab to penetrate into the lower mantle (e.g., *Fukao & Obayashi, 2013*). In addition, some studies about focal mechanisms show that slabs are prone to buckle at the base of the upper mantle (e.g., Myhill, 2012). Between the upper and lower mantle discontinuity, earthquakes do not occur (e.g., *Stark & Frohlich, 1985)*.

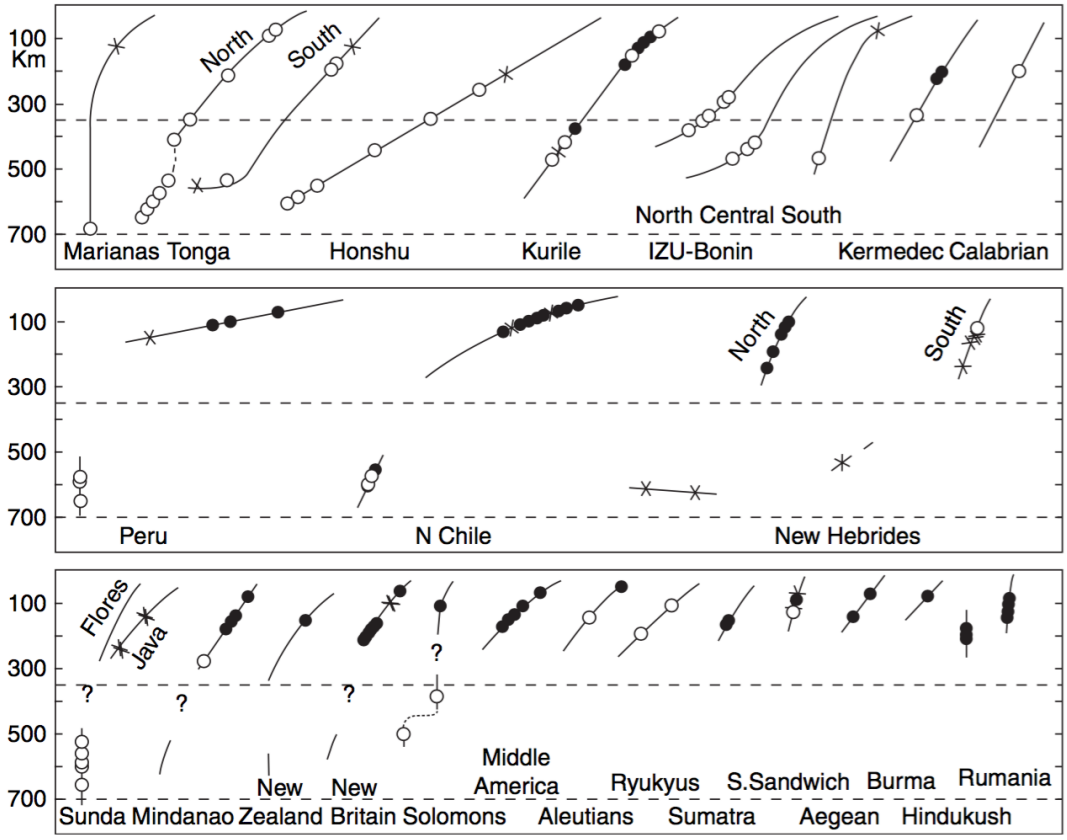

Figure 1.5: A global summary of down-dip compressive stresses calculated from focal mechanisms. The open circle is for down-dip compressive or P axis roughly parallel to the slab dip and the filled circles are down-dip T or tensional axis parallel to slab dip. The line represents the dip and length of the seismicity in the subduction zone From *Isacks and Molnar* (1971).

Tomographic images play an important role to unravel the slab structure, without providing information on the stress field. The large number of tomographic models (e.g., *Bull, et al., 2009; van der Hilst , 1997; www.atlas-of-the-underworld.org*) allow to see that slabs are not 2-D tabular features. Slab dip and morphology are variable (Fig. 1.6; *Goes et al., 2017*): some slabs stagnate at the base of the upper mantle such as in the North-West Pacific *(Fukao & Obayashi, 2013; Fukao, 1992; Zhao, 2009*), some slabs appear to sink directly into the lower mantle up to 2500 km depth, as beneath central America or Marianas. However, tomographic resolutions are often low due to lack of knowledge about the mantle temperature field or the seismic proprieties as well as the poor coverage (e.g., *Becker & Boschi, 2002*). Indeed, the major mantle phase boundary disturb the seismic travel-time (*King, 2007; Li et al., 2008*). Therefore, in some regions, like in Japan, the apparent thinning of the slab into the mantle transition zone might be linked to the seismic travel time anomalies rather than reflecting the thinning of the slab itself (e.g., *King, 2007*).

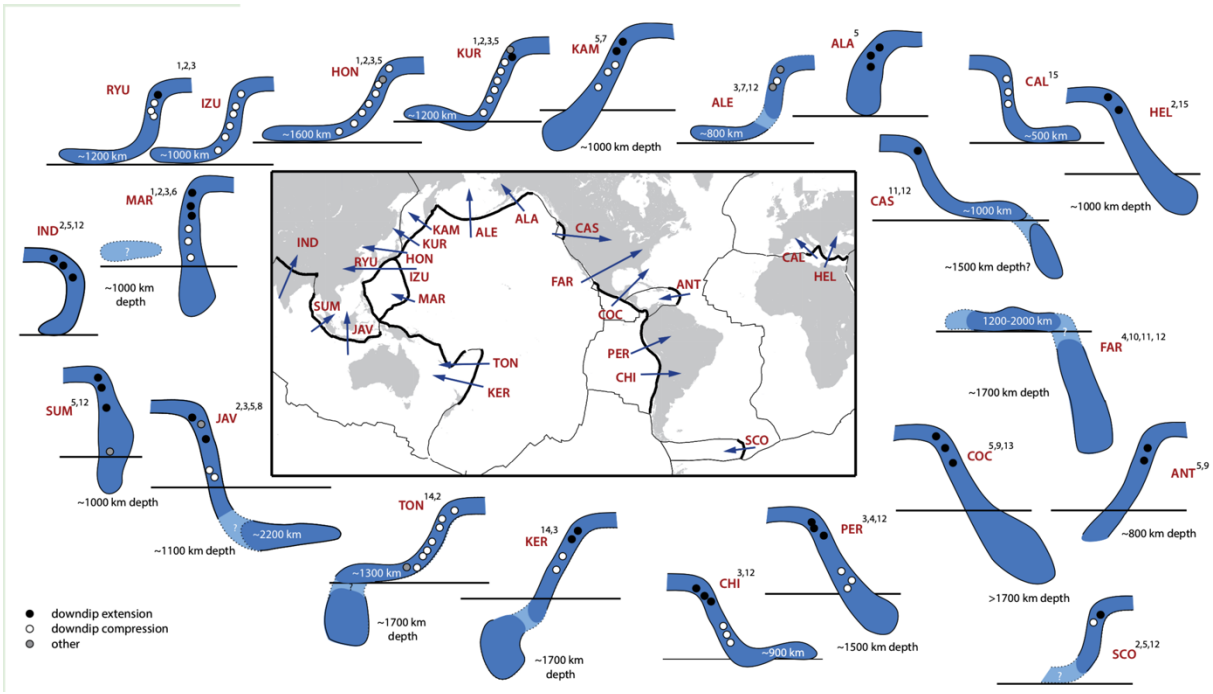

Figure 1.6: Summary of morphologies of transition-zone slabs as imaged by tomographic studies and their Benioff stress state. Arrows on the map indicate the approximate locations of the cross sections shown around the map, with their points in downdip direction. After *Goes et al.* (2017).

1.2.2 Mantle viscosity inferred from post-glacial rebound

The time-dependent vertical motion of crust after the last glaciation is the most used observable providing constrains on the viscosity of the mantle. Indeed, the melting of large ice sheets occurred rather quickly, about 10.000 years ago (Fig. 1.7; *Peltier, 1981*). The ice melting causes re-distribution of load that triggers isostatic adjustment of the lithosphere. Therefore, the re-distribution of load has caused slow flow of the underlying mantle that resulted in the time-dependent vertical crustal motion. Previous studies estimated the slow flow of the mantle at about 10^4 to 10^5 years (e.g., *Karato, 2010*). Approximating the mantle as a Newtonian fluid, without heterogeneities, post-glacial rebound data suggested the mantle viscosity ranges between 10^{20} to 10^{21} Pa s (*Peltier, 1998; Turcotte & Schubert, 2002*). Recent studies consider the mantle as a Newtonian fluid but stratified, suggesting an upper mantle viscosity of ~5×10^{20} Pa s and a lower mantle of ~2×10^{21} Pa s (*Zhong et al., 2007*). Inverted post-glacial redound and long wavelength geoid observations suggest a viscosity increasing between 10^{20} Pa s at the base of the lithosphere to ~10^{22} Pa s at about 2000 km depth (Fig. 1.7; *Mitrovica & Forte, 2004*).

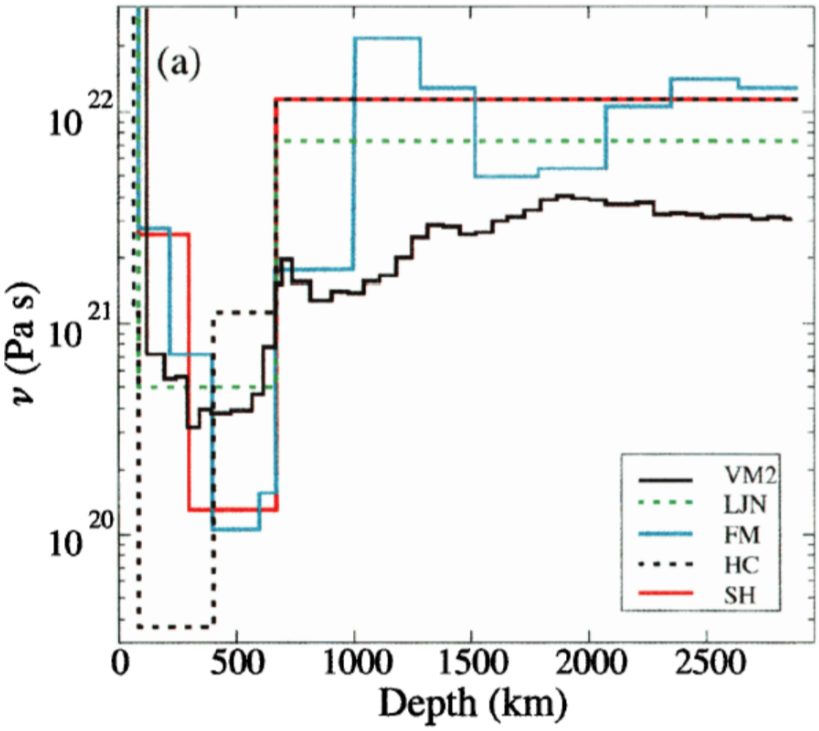

Figure 1.7: Viscosity profile as function of depth inferred from glacial rebound from *Peltier* (1998).

1.2.3 Geoid

The geoid is the surface of constant potential energy (i.e., gravitational energy plus centrifugal potential energy) that coincides (almost) with mean sea level over the oceans. The association between the local maxima of the long-wavelength component of the gravitational potential field (i.e., geoid) and subduction zone has been recognized by many authors (e.g., *Flament, 2013*). If we consider that the mantle is an iso-viscous fluid (Fig. 1.8, middle panel), the geoid over a positive mass anomaly, such as a slab, is negative (*Hager & O'Connell, 1981; Richards & Hager, 1984*). This is because the flow, driven by the mass anomaly (Fig. 1.8), deforms the surface (and the core mantle boundary) creating negative mass anomalies (i.e., long-wavelength depressions). The sum of the contributions from the positive and negative mass anomalies for an hypothetic iso-viscous mantle is negative (and small) (e.g., *Hager, 1984; Ricard et al., 1984*). The amount of surface deformation from the same positive mass anomaly is reduced with a layered viscosity increase with depth (Fig. 1.8, right panel; i.e., the mass anomaly is supported by the stiff layer below) and the resulting anomaly can change sign depending on the viscosity structure (e.g., *Flament, 2013; Hager, 1984; Ricard et al., 1984*). The long wavelength geoid associated to subduction zones requires that slab encounters a resistance to flow at depth, which model as an increase viscosity within a range of factor 30-

100 at the upper-lower mantle discontinuity (e.g., *Hager, 1984; Gurnis, & Moresi, 1996*). Indeed, it is required to produce local geoid maxima over slabs. The lower end-member (~30) is consistent with other geophysical observations that constrain mantle rheology also with postglacial rebound (e.g., *Mitrovica, et al., 1996; Pysklywec & Mitrovica, 1997*). However, the upper end-member (~100) is difficult to reconcile with most of the shape increasing in mantle viscosity models. Indeed, from the geoid observations into subduction zones, models with strong increases in viscosity do not fit with postglacial rebound studies (e.g., *Lambeck & Nakada, 1990*).

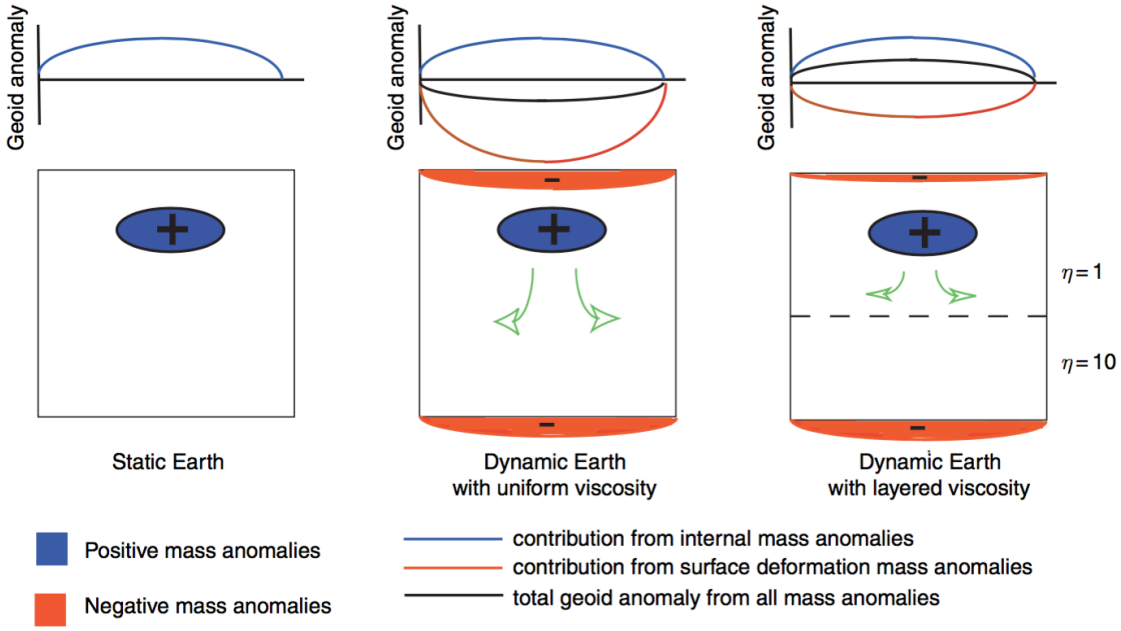

Figure 1.8: Cartoon of the geoid anomaly over a positive mass anomaly for a static (left), iso-viscous (centre) and layered (right) mantle. Blue lines indicate the contribution to the geoid from the mass anomaly, the red lines represent the contribution. From *King* (2007).

1.2.4 Dynamic topography

The topography of the Earth is primarily controlled by lateral differences in the density structure of the crust and lithosphere. In addition to this *isostatic* topography, flow in the mantle induces deformation of its surface leading to *dynamic topography*. This transient deformation evolves over millions of years, occurs at long wavelength (>1000 km), and is relatively small (<2 km) in amplitude (Fig. 1.9; *Zhong & Gurnis, 1992*) . The long-wavelength dynamic topography is recorded by lithospheric plates moving over the mantle flow which in turn, is also transient over million years. As a result, subsidence events are generally followed by uplift and vice versa (*Flament et al., 2013*). Indeed, the fact that dynamic topography is transient

means that it must be recorded over long time periods, over which the preservation potential of the rock record is poor (*Mitrovica et al., 1989*). Indeed, the long-wavelength, low-amplitude dynamic topography signal makes it difficult to isolate in the geological record, which is dominated by shorter-wavelength, larger-amplitude signals such as lithospheric extension or shortening. Another limit on the status of dynamic topography comes from the geological record itself, which is biased toward areas that have been subsiding for long periods of time and have a good preservation potential, as opposed to uplifting areas that are subject to erosion and have a poor preservation potential (*Flament et al., 2014; Steinberger, 2007*). However, strata deposited in a dynamic topography depression also have low long-term preservation potential because dynamic topography is transient. Thus, ancient subduction related dynamic topography is most likely to be represented by unconformities *(Burgess & Moresi, 1999*). As a consequence, the stratigraphic record is the most accessible archive of the dynamic topography signal, and continental interiors that have not undergone deformation for hundreds of millions of years are the most promising places to search for the dynamic topography signal (e.g., *Flament et al., 2013; Gurnis, 1992*).

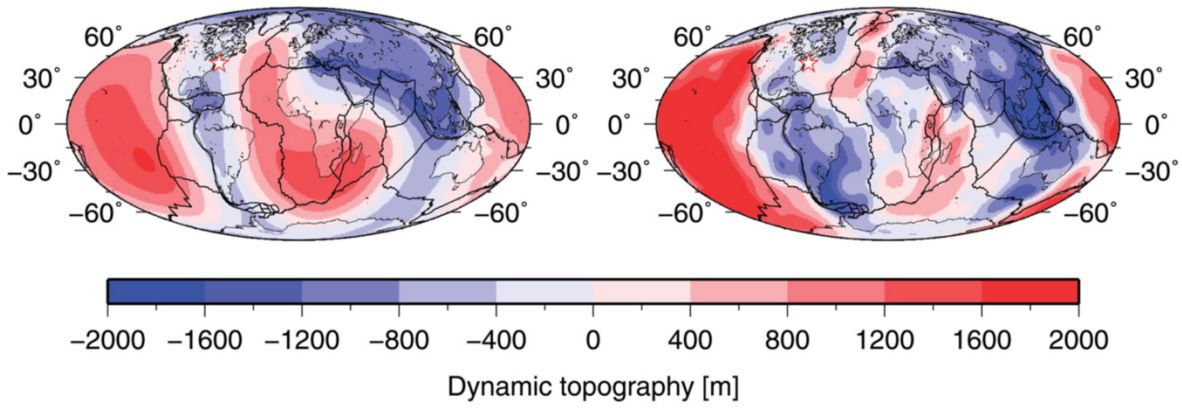

Figure 1.9: Graphical comparison of the present-day dynamic topography (water-loaded in the oceans, air-loaded in the continents, and averaging to zero predicted by *Flament* (2013) on the right and *Steinberger* (2007) on the left.

1.3 Proprieties of the Earth

In this section I introduce first, the state of the art about the lithospheric composition, deformation mechanisms and geometry. Second, I provide an overall view on the composition and the stratification of the mantle from surface to depth.

1.3.1 Lithosphere

An essential feature of plate tectonics is that the lithosphere, remains rigid during long intervals of geologic time (Fig. 1.10). Because of their low temperatures, rocks in the lithosphere resist deformation on time scales of up to billion years. In contrast, the rock beneath the lithosphere is sufficiently hot that solid-state creep occurs. The lithosphere is composed of both mantle and crustal rocks (*Burov, 2011; King, 2001*). The oceanic lithosphere has an average thickness of 100 km, with the uppermost ~7 km being the oceanic crust. The continental lithosphere has an average thickness of about 200 km. Typically, the upper 30 km of the continental lithosphere is continental crust. Because of the positive buoyancy of the continental crust, the continental lithosphere does not subduct. The strength of the lithosphere allows the plates to transmit stresses over geologic time. The plates act thus, as stress guides. Stresses that are applied at the boundaries of a plate can be transmitted through the interior of the plate. The ability of the plates to transmit stress over large distances is a key factor in driving tectonic plates. These stresses are also responsible for some intraplate earthquakes and small amounts of intraplate deformation (*King, 2007*).

Laboratory experiments on rock samples show at low pressure, brittle rock fracture behaviour once the rock material reaches the breakdown threshold. At high pressure, ductile deformation occurs. Between those two end-members, both deformation may occur *(Evans et al., 1990*). Other experiments show at both high temperature and pressure that the type of deformation and the strain state depends on several parameters such as the temperature, grain size or the water contents within the sample. Those parameters are described by laws characterising the type of deformations. The most common law that is used to describe how rock may deform is a power law (see chapter 2; Eq. 2.15; e.g., *Hirth & Kohlstedt, 1995; Regenauer-Lieb & Yuen, 2003*).

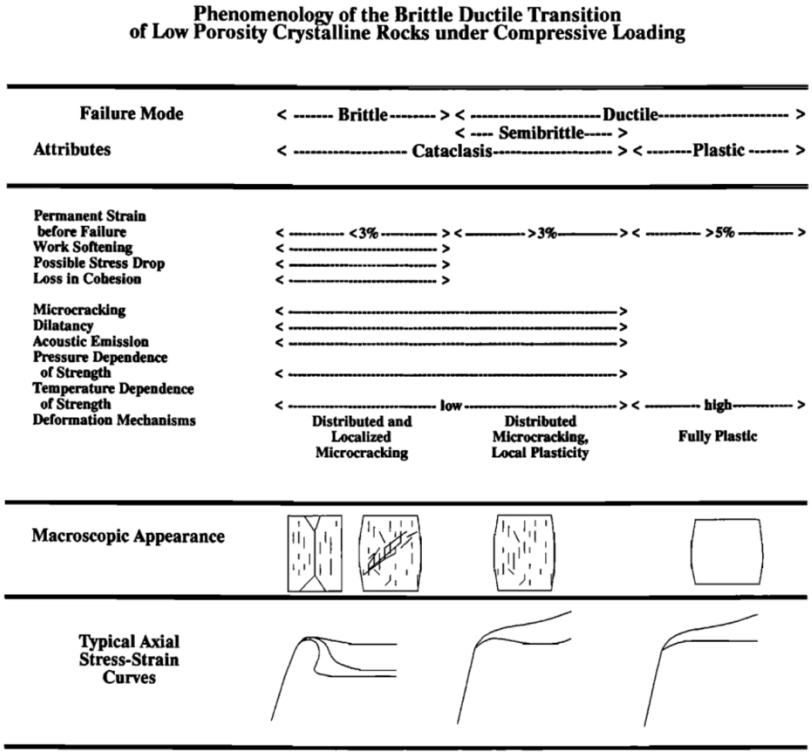

Figure 1.10: Schematic diagram illustrating the phenomenology of the brittle-ductile transition. After *Evans et al.* (1990)

Other experimental studies consider that the temperature and the pressure determine how do the lithospheres may deform. Typically, the strain rate linked to geodynamics processes range from 10^{-14} to 10^{-16} s^{-1}. The strength envelope in Figure 1.11 illustrates how the differential stress (in MPa) could affect the rock behaviour as function of depth. Figure 1.11 from *Kohlstedt et al.* (1995) proposes that the differential stress control the deformation of the oceanic and continental lithosphere by considering a strain rate of 10^{-15} s^{-1}. Both curves show different mechanical behaviour as function of depth. For instance, oceanic lithosphere is brittle down to 10 km depth. Beyond 40 km depth, the resistance to deformation decreases with depth. Here, authors propose that the maximal resistance to deform is about 800 MPa at 600°C. However, a wide number of models have been proposed for stress and strength envelopes for the continental and oceanic lithosphere (e.g., *Evans et al., 1990; Kohlstedt et al., 1995*).

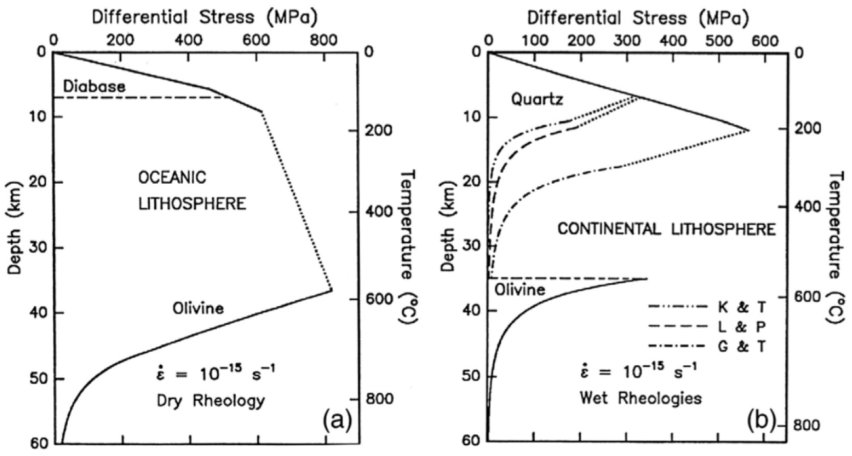

Figure 1.11: Example of strength envelopes for oceanic and continental lithospheres. A dry olivine is used to simulate the rheology of an oceanic lithosphere (panel a) . The wet quartzite is used to simulate the rheology of a continental lithosphere (panel b) (see *Kohlstedt et al.* (1995) for details).

1.3.2 The upper mantle

Due to the increase in temperature and pressure, the upper mantle rocks are viscous (e.g., *Turcotte & Schubert, 2002; Karato and Wu, 1993*). According to laboratory experiments, the viscosity of the mantle depends on both dislocation and diffusion creep mechanism (*Karato and Wu, 1993*). Those mechanisms are sensitive to the pressure, temperature, hydrated or dry conditions of the mantle or by Peierls mechanism (*Kameyama et al., 1999*). Form both mechanisms, the strong dependence of the viscosity on the activation volume, which is not well constrained, especially for dislocation creep mechanism (*Karato & Wu, 1993*). Indeed, a strong variation in viscosity against depth is clearly seen for dislocation creep while it more stable for diffusion creep (Fig. 1.12).

Karato & Wu (*1993*) suggest strong variations in upper mantle viscosity with depth for dislocation creep mechanism whereas the viscosity increases linearly with depth for diffusion creep mechanism (Fig. 1.12c-f). This study estimates that the mean viscosity for a hydrated mantle induced by diffusion creep is about 10^{20} Pa s between 100 to 400 km depth and 10^{21} Pa s for a dry mantle. In contrast, dislocation creep induces variation in viscosity with depth leading to low viscosity zone beneath the lithospheres. Authors propose that the upper creep mechanism is dominated by dislocation between 100 to 200 km depth and below by diffusion.

Other studies (*Hirth & Kohlstedt, 2003*) propose that the dehydration of the slab into the uppermost part of the mantle generates a weak mantle wedge, inducing weak viscosity zone with viscosity ranges from 10^{17} to 10^{21} Pa s (Fig. 1.12g).

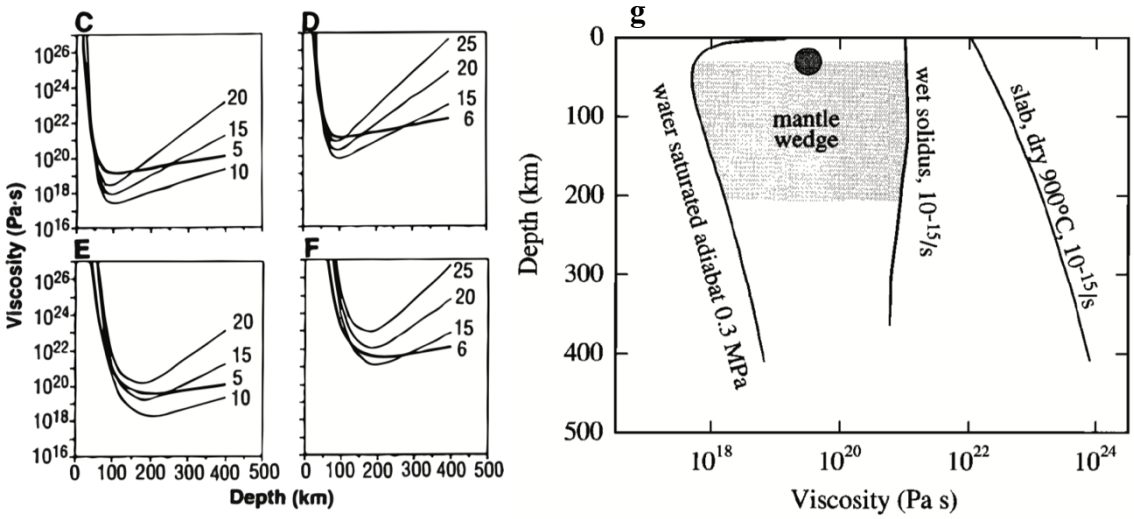

Figure 1.12: left: depth variation of the effective viscosity for different geotherms and a range of activation volumes for dislocation creep. (C) hot and wet mantle; (D) hot and dry mantle; (E) cold and wet mantle and (F) cold and dry mantle from *Karato and Wu* (1993). Right, mantle wedge and slab effective viscosity estimations from *Hirst and Kohlsedt* (2003).

1.3.3 The mantle transition zone

The mantle transition zone is a thick layer within the mid-mantle. Due to the increasing temperature and pressure within the mantle, mineral changes occur and are defined by the Clapeyron slopes (e.g., *Christensen, 1995*). Phase transformations of minerals within slabs have a significant impact on subduction dynamics (e.g., *Christensen, 1995; Ita & King, 1998*). Far from the subduction zones, the composition of the mantle is assumed as follows:

- The depth of about 410 km depth (corresponding to the 1600°C isotherm) corresponds to the olivine to wadsleyite transformation, where the density become greater about $\Delta\rho = 280\ \mathrm{kg/m^3}$ (Fig. 1.13; e.g., *Turcotte & Schubert, 2002; Karato 2003; Goes et al., 2017*;). The Clapeyron slope of the mineral transformation corresponds to a positive topography.
- Deeper, between 410 km and 670 km depth, wasdleyite transforms progressively into ringwoodite (Fig. 1.13; e.g., *Katsura & Ito, 1989*).

- At about ~670 km depth the thermal gradient is about 1700°C (Fig. 1.13). The Ringwoodite transforms into Perovskite and Magnesiowustite. The density contrast associated with the phase changes give a negative Clapeyron slope of about $\Delta\rho = 400\ kg/m^3$ (e.g., *Karato et al., 2000; Turcotte & Schubert, 2002*).

Additionally, some joint inversions models (e.g., *Mitrovica and Forte, 2004*) show that a jump in viscosity close to 670 km depth occur. Indeed, the geoid signature (section 1.2.3) above subduction zones indicates a sharp increase in viscosity of a factor 30–100. This jump is required to explain smaller-scale geoid structure around subduction zones (*Goes et al., 2017; King, 2002; Tosi et al., 2009*).

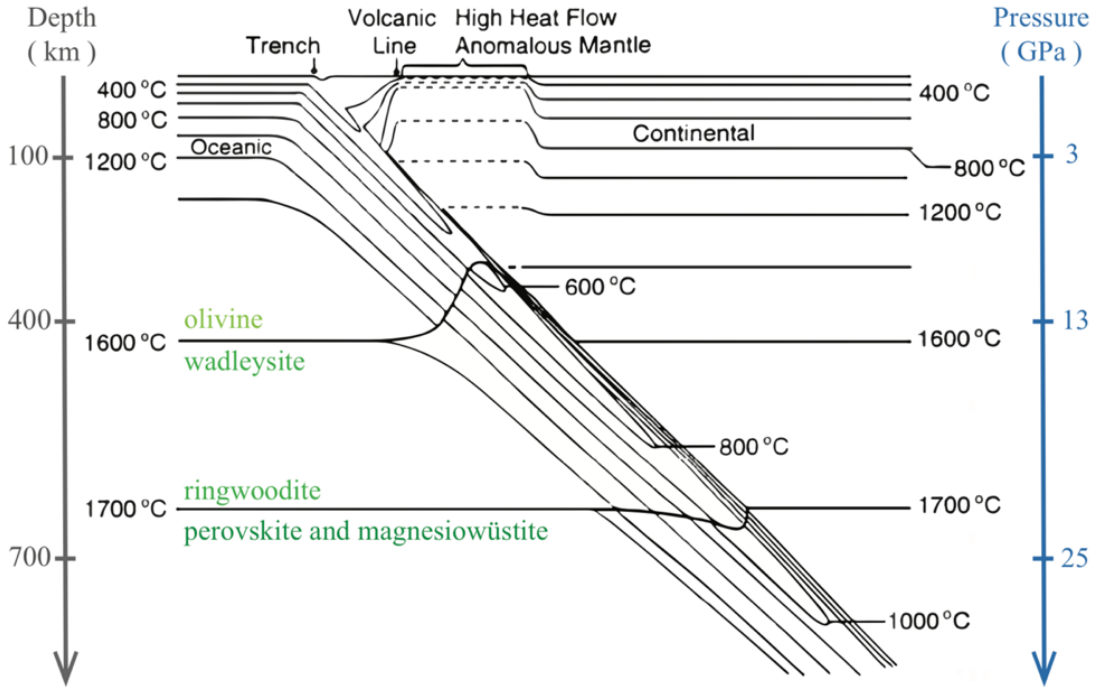

Figure 1.13: After *Turcotte & Schubert* (2002). Thermal and pressure gradient of subduction zone implying a subducting plate, continental overriding plate and the metastable transformation of the Olivine to heavier phases at depths.

1.3.4 The lower mantle

Only few constraints resulting from high-pressure experiments (*Karato, 2010*) allow us to know the lower mantle structure and composition. Uncertainties come out from the lower mantle proprieties, such as the activation and energy volumes under high pressure and temperature conditions which render viscosity estimates of unknown accuracy.

Other studies estimate the mantle viscosity profile from a joint geophysical inversion of mantle structure, the geoid, and/or vertical surface motion data associated to ice sheet (un)loading and sea level change, heat flow, or dynamic surface topography (*Čížková et al., 2012; Forte & Mitrovica, 1996; Panasyuk & Hager, 2000; Pari & Peltier, 1995; Ricard & Vigny, 1989; Steinberger & Calderwood, 2006)*. These studies resulted in wide range of viscosity (Fig. 1.14) which reflect the weak sensitivity of the data and models for (depth) variations in lower mantle viscosity (*Čížková et al., 2012*).

Čížková et al. (2012) proposed a new approach in order to overcome the lack of understanding about the lower mantle viscosity. This approach consists in 2D numerical simulations to figure out how fast are remnant, slabs into the lower mantle. They found that the gradual viscosity increase characterizing the viscosity profiles reduces the sinking velocities of the subducted lithospheres in the deep lower mantle. Their results fit with previous study of (*Van Der Meer et al., 2010*) which shows that the absolute plate motion may be an indicator of deep slab sinking velocity at about ~2 cm/yr**.** *Čížková et al.* (2012) demonstrate that the sinking velocity of slab is very sensitive to the viscosity of the lower mantle and thus provide constraint about on lower mantle viscosity. Thus, they estimate the averaged lower mantle viscosity of about $5x10^{22}$ Pa s.

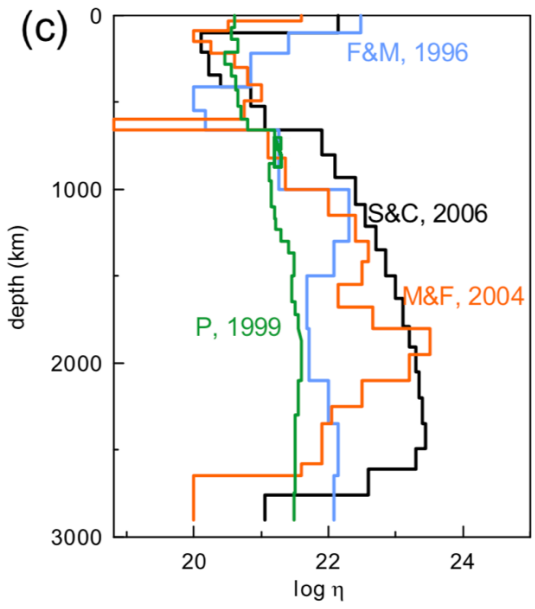

Figure 1.14: Viscosity profiles based on the joint inversion of the geoid and postglacial rebound data. *Forte and Mitrovica (1996), Peltier (1999), Mitrovica and Forte (2004), Steinberger and Calderwood (2006).* See *Čížková et al.* (2012) for details.

1.4 Influences of the mantle and plate rheology on slab dynamics

Subduction dynamics is strongly controlled by the plate and mantle rheology which involve thermal, chemical and mechanical processes. Hence, to model how slab may be affected by mantle and plate heterogeneities some assumptions are made. Those assumptions may be described as conceptual, mechanical model of subduction zone. Figure 1.15 highlights how the plates and mantle may act onto the slab as resisting of driving forces.

From the surface, the bending of the slab at the plate interface induces resisting force to slab penetration into the mantle (e.g., *Becker et al., 1999*). Also, the intraplate resistance between the upper and lower plates induces resisting force on the slab behaviour at depth (e.g., (*McKenzie, 1977*). In contrast, the ridge push acts as a far field tectonic force associated to the topography variation from the ridge to the trench and acts as a driving force to slab penetration (Fig. 1.15 ; e.g., *Forsyth & Uyedat, 1975*).

At depth, the cold subducting lithosphere sinks into the upper mantle, driven by its negative buoyancy which acts as a driving force (i.e., thermal buoyancy; e.g., *Forsyth and Uyeda, 1975*). The mantle drag beneath plates and surrounding the slab results in a viscous mantle resistance which decelerates the slab sinking velocity. At About 410 km depth, metastable mineral transformation from the olivine to waldeylite may produces and increasing in slab density (phase buoyancy). Within the cold slab, the 410 km depth metastable transformation of the olivine may be kinetically postponed. Hence, the increasing force due to the 410 km depth Clapeyron slope may be reduced (*Rubie & Ross, 1994*).

In contrast, at about 670 km depth, the metastable mineral transition from wasldeylite to post-spinel decreases the density of the slab (phase buoyancy). Those strong variations in slab density triggered by Clapeyron slopes (Chapter 3) may deform and buckle the slab at depth (e.g., *Agrusta et al., 2017; Čížková & Bina, 2019; Goes et al., 2017*). In addition, the slab anchoring induces by the viscous lower mantle may hampers the slab propagation at greater depth (Fig. 1.15).

How the resisting and driving forces affect the slab dynamics at depth, the slab may behave differently between two end-members: from stagnating into the mantle transition zone to penetrating into the lower mantle (e.g., *Agrusta et al., 2017; Čížková & Bina, 2019; Ribe, 2003*).

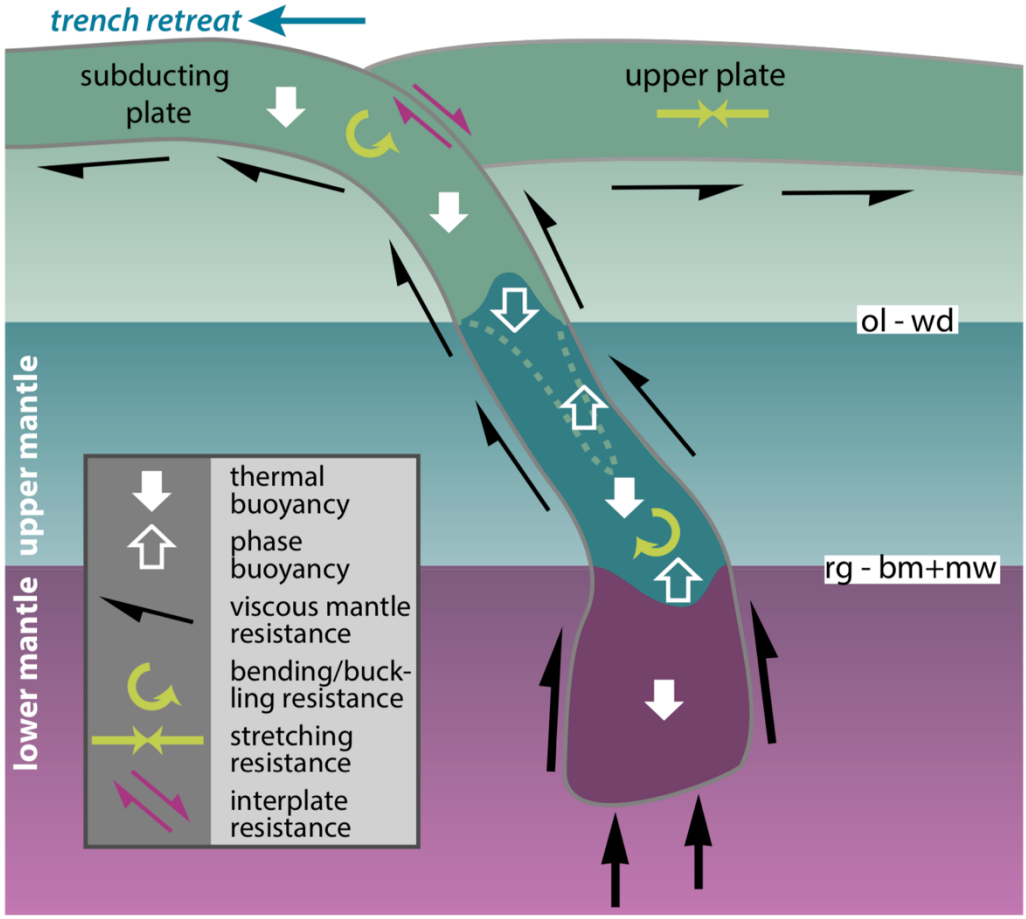

Figure 1.15: Schematic diagram showing the main forces that affect how slabs interact with the transition zone. The slab sinks driven by its negative thermal buoyancy (white filled arrows). Sinking is resisted by viscous drag in the mantle (black arrows) and the frictional/viscous coupling between the subducting and upper plate (pink arrows). To be able to sink, the slab must bend at the trench. This bending is resisted by slab strength (curved green arrow). From *Goes et al.* (2017).

1.5 Sensitivity of the upper plate topography

The upper plate surface topography is strongly affected by the rheological and mechanical proprieties of the slab, plates and the mantle (e.g., *Crameri et al., 2017; Crameri & Lithgow-Bertelloni, 2017*).

Numerical models from *Crameri et al.* (2017) show that the bending of the slab, the slab buoyancy, the mantle viscosity and the plate strength play a crucial role into the regional subduction zone topography. They found that the shallow-depth slab dip and the slab buoyancy dominate most regional surface topography signal (Fig. 1.16). The back-arc depression caused by a shallow-dipping slab is shown to merge with the trench depression for steeper dipping slabs. They show that abnormally deep back-arc depressions generally observed in numerical

models are prevented with a combination of a low-viscosity mantle wedge and steeply dipping shallow slabs. The island-arc elevation and the lateral extent of the back-arc depression are exceptions to this trend. The island-arc and the lateral back-arc depression are mainly controlled by horizontal, tectonic stresses and thus mainly by the strength of the plate. Overall, a strong plate produces more viscous bending dissipation which dampens the topographic amplitudes by converting short-wavelength mantle stresses into long-wavelength surface deflections. The radial mantle viscosity adds a nonnegligible, intermediate contribution to the topographic amplitude over the short period. A longer slab, another important geometric feature, induces a larger flow cell in the mantle wedge enhancing a shallow flow toward the slab. This causes more compression in the plate above through viscous coupling, which pronounces the island-arc.

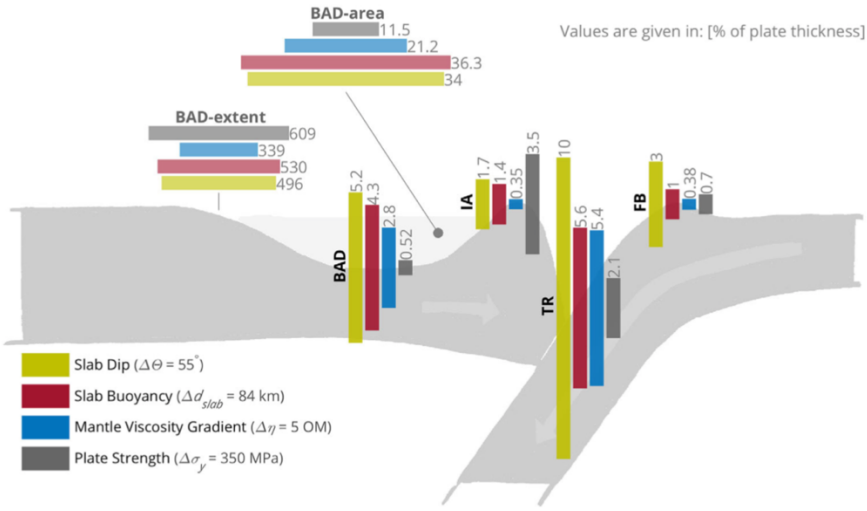

Figure 1.16: Overview over the potential range over which individual subduction parameters can spatially alter the individual topographic features of a collisional plate boundary on an Earth-like planet. The height of a bar indicates the maximal spatial variation occurring in the experiments presented here over an Earth-like parameter range given in the figure legend. Values are given in percentage of plate thick- ness. The individual topographic features indicated are fore-bulge height (FB), trench depression (TR), island-arc height (IA), and back-arc depression (BAD), extent (BAD-extent), and area (BAD-area). From *Crameri et al.* (2017).

Crameri and Lithgow-Bertelloni (2017) show also that the dynamic interaction of the slab with the upper/lower mantle transition zone affects large-scale upper plate topography. Thanks to models which includes an upper-mantle viscosity jump, the 670km depth phase transition within single sided-subduction, they find that the upper plate tilts towards the subduction as soon as such a sub-vertical slab interacts with the lower mantle. This upper plate tilting is

induced by large subduction-induced flow cell underneath the upper plate due to the displacement of higher- viscosity material in the lower mantle (Fig. 1.17).

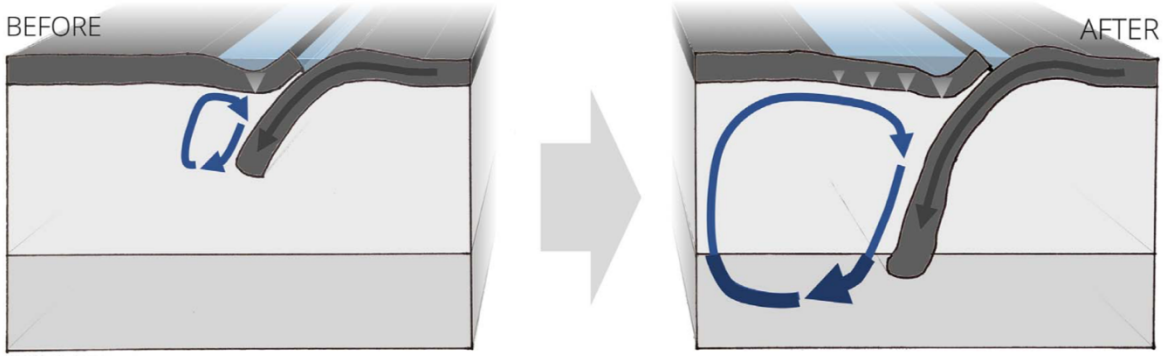

Figure 1.17: Schematic illustration comparing the slab dynamics before and after slab-transition zone interaction. The left panel indicates an incipient subduction zone before slab-transition- zone interaction with only small-scale subduction-induced mantle flow, and no large-scale upper plate tilt. The right panel indicates a mature subduction zone after slab-transition-zone interaction and resulting excitation of the high-viscosity lower mantle which leads to a significantly larger, subduction-induced mantle return flow cell. The onset of the large-scale mantle flow causes an abrupt increase in continental-scale upper-plate tilt and inundation. From *Crameri and Lighgow-Bertelloni* (2017).

Hence, at regional and large scales, the surface topography of the upper plate is sensitive to both plate and mantle parameters. It is thus, important to constrain models with indirect and direct observable from the present-day Earth in order to continue to explore how the deep interior may control the large scale topography.

Thesis outline

The aim of this work is to unravel how the slab behaves at depth and the resulting surface fingerprints around subduction zones. In particular, I start study how slab morphology changes by tuning rheological features and geometrical parameters. Then, I perform more complex models in order to understand how the surface topography of subduction zone is affected by deep slabs dynamics. Finally, I export the numerical outcomes to decipher the history of the central Neotethys subduction zone.

The thesis is structured in 6 Chapters. After this Introduction (Chapter1), I present the numerical method and the applied techniques in the Chapter 2. Then, I analyse the role of the mantle rheology and the initial plate strength on the slab morphology and the related surface kinematics and dynamic topography as obtained from 2D numerical models (Chapter 3). In Chapter 4, I apply numerical results to the central Neotethys subduction system which has been active from ~100 Ma to 30 Ma. Finally (Chapter 5), I develop 3D models that allow to explore the variability of slab morphology into the mantle transition zone and the resulting dynamic topography. The thesis ends with the general conclusion (Chapter 6).

Chapter II

Numerical method and applied techniques

Since we cannot directly observe the ongoing processes of the Earth interior, we have to lean on indirect measurements such as geological observations, geochemical signatures from volcanism and geophysical approaches like seismology and gravity. However, most of those tools provide information about the present-day state of Earth's interior and they do not give information about the long-term evolution of geodynamical processes. The numerical methods are useful to simulate mantle flow and to model plate tectonic mechanisms, and they allow to study the mantle processes in a time-dependent manner. This chapter describes the methodology used to study the subduction zones dynamics. First, the governing equations that rule the physical system and the numerical method applied will be introduced. Secondly, the applied rheology and compositional models are defined. The third section deals with the topography formulation and the applied general boundary conditions. The chapter ends showing the general model set up and the resolution test.

2.1 Governing equations

On the geological time scale, the Earth's mantle behaves like a highly viscous fluid, and it can be described by a system of fluid dynamic conservation equations. The thermo-compositional convection model is governed by the equations describing the conservation of mass, momentum, energy and composition for an incompressible fluid under extended Boussinesq approximation (*Christensen & Yuen, 1985; Ita & King, 1998*), with infinite Prandtl number, without internal heating. The Boussinesq approximation (BA) implies that the density differences are neglected except in the buoyancy term of the momentum equations (Eq. 2.3). The BA is usually applied to mantle convection, and with this approximation, the internal buoyancy forces arising from the density variations within the model drive the system. For the purpose of this thesis, the density variation driving the flow results from thermal and compositional changes:

$$\Delta\rho(T, \mathrm{C}, \Gamma) = \rho_0 \sum_{\mathrm{i}} \frac{\delta\rho_{\mathrm{i}}}{\delta\rho_0} \overline{\Gamma_i} + \frac{\Delta\rho_{\mathrm{c}}}{\rho_0} - \alpha_0(\overline{T} - \overline{T_0}) \qquad 2.1$$

Symbols and values are given in Table 2.1. Each *i* is the phase transition transformation that turns the mantle into a denser phase, expressed by the density increase $\delta\rho_i$. The thermal difference comes from the temperature differences (T-T_0) where the reference expansion coefficient α_0 is considered constant. The lithosphere is thus, considered as the cold, dense and therefore, negatively buoyant, top boundary layer of the domain. The density variation derives

from the composition of the crust ρ_c= *2700kg/m³* and the mantle ρ_0= *3300kg/m³* are also considerate.

For the incompressible fluid, the conservation of mass is described with a divergence-free velocity field, as follows,

$$\nabla . \bar{\mathbf{u}} = 0 \tag{2.2}$$

The conservation of momentum is described by the Stokes equations and it represents the balance between the pressure, viscous and body forces acting within the system:

$$-\nabla \bar{p} + \nabla\left(\bar{\eta}(\nabla\bar{\mathbf{u}} + \nabla\bar{\boldsymbol{u}}^{\boldsymbol{T}})\right) = \overline{\alpha_z}\,\mathrm{Ra}\bar{T} + \mathrm{RaC} + \sum_{n=1}^{n}\mathrm{Rb_i} + \bar{\Gamma}_i \tag{2.3}$$

The conservation of energy is described in the temperature field:

$$\left[1 + \sum_{i=1}^{n}\left(\frac{d\bar{\Gamma}_i}{d\bar{z}}\,\bar{\gamma}_i^{\,2}\,\frac{\mathrm{Rb_i}}{\mathrm{Ra}}\,\mathrm{Di}(\bar{T} + \bar{T}_s)\right)\right]\left(\frac{\delta\bar{T}}{\delta\bar{t}} + \bar{\mathbf{u}}\cdot\nabla\bar{T}\right) =$$

$$\nabla^2\bar{T} - \left[1 + \sum_{i=1}^{n}\left(\frac{d\bar{\Gamma}_i}{d\bar{z}}\,\bar{\gamma}_i\frac{\mathrm{Rb_i}}{\bar{\alpha}_z\,\mathrm{Ra}}\right)\right]\bar{\alpha}_z\,\mathrm{Di}(\bar{T} + \bar{T}_s)\bar{\mathbf{u}}_z + \frac{\mathrm{Di}}{\mathrm{Ra}}\,\bar{\boldsymbol{\sigma}}\,\bar{\boldsymbol{\varepsilon}} \tag{2.4}$$

The conservation of the composition is defined as follows,

$$\frac{\delta C}{\delta \mathbf{t}} + \bar{\mathbf{u}}\nabla C = 0 \tag{2.5}$$

Where, $\bar{\boldsymbol{u}}, \bar{\gamma}_i, \bar{P}, \bar{T}, \bar{T}_s, \bar{t}, \bar{z}, \bar{\alpha}_z, \bar{\boldsymbol{\sigma}}, \dot{\bar{\boldsymbol{\varepsilon}}}$ and $\bar{\eta}$ are the dimensionless (indicated by the upper bar) velocity, Clapeyron slope of *i*th phase transition, pressure, temperature, surface temperature, time, depth, coefficient of thermal expansion, stress, strain rate and viscosity. The thermal expansion coefficient is depth dependent and defined as $\alpha_z = \exp(-1.1z)$, where z is the depth (*Tosi et al., 2013*).

Ra, $\mathrm{Rb_i}$ and $\mathrm{Ra_c}$ are the thermal Rayleigh number, buoyancy Rayleigh number and compositional Rayleigh number, respectively. They are defined as follows;

$$\mathrm{Ra} = \frac{\alpha_0\rho_0\Delta T H^3}{\kappa\eta_0} \tag{2.6}$$

$$\mathrm{Rb_i} = \frac{\delta\rho_c g H^3}{\kappa\eta_0} \quad 2.7$$

$$\mathrm{Ra_c} = \frac{g(\rho_c - \rho_m)H^3}{\kappa\eta_0} \quad 2.8$$

D_i is the dissipation number which characterizes the heat transfer capacity in the system.

$$\mathrm{D_i} = \frac{\alpha_0 \rho_m H}{C_p} \quad 2.9$$

In equation 2.3, Γ correspond to the harmonic phase function (*Agrusta et al., 2014*), describing the relative fraction of the heavier phase is described by the phase, which varies from 0 to 1 with respect to pressure and temperature field as follows,

$$\Gamma_i = \frac{1}{2}\left[1 + \sin\left(\pi \frac{\bar{z} - \bar{z}_1 - \bar{\gamma}_1(\bar{T} - \bar{T}_1)}{\bar{d}_1}\right)\right] \quad 2.10$$

where d_i is the vertical width of the transition i, is Clapeyron slope at the equilibrium, and z_i and T_i are the depth and the temperature of the phase transition at equilibrium conditions.

Symbol	Parameter	Unit	Value
	Governing equations		
H	Box height	km	3000
ΔT	Potential temperature drop	K	1623
C	Composition	-	-
ρ_0	Reference density	$kg \cdot m^{-3}$	3300
ρ_c	Continental crust reference density	$kg \cdot m^{-3}$	2700
ρ_m	Mantle reference density	$kg \cdot m^{-3}$	3300
$\Delta\rho_c$	Continent reference density	$kg \cdot m^{-3}$	2700
g	Gravity	$m \cdot s^{-2}$	9.8
α_0	Surface thermal expansion	K^{-1}	3×10^{-5}
α_z	Thermal expansion depth dependency	K^{-1}	-
κ	Thermal diffusivity	$m^{-2} \cdot s^{-1}$	10^{-6}
η_0	Reference viscosity	Pa·s	10^{20}
C_P	Heat capacity	$J \cdot kg^{-1} \cdot K^{-1}$	1250
R	Gas constant	$J \cdot mol^{-1} \cdot K^{-1}$	8.314
	Mantle phase transition parameters		
γ_i	Clapeyron slope transitions at equilibrium (i)	$MPa \cdot K^{-1}$	-
z_i	Transition equilibrium depth	km	-
d_i	Transition width equilibrium	km	20
T_i	ol-wd transition potential temperature	K	1423

Table 2.1: Governing equations parameters

2.2 Numerical method

For nonlinear and time-dependent thermo-compositional convection problems, the governing equations can only be solved numerically. For this study I used the finite element numerical code CITCOM (*Wang et al., 2015; Zhong et al., 1996*), because the finite element method (FEM) is extremely robust in treating complex material proprieties and geometries, and CITCOM allows to solve the equations in 2D and 3D Cartesian domain.

The CITCOM allows to solve the momentum equation (Eq. 2.3) coupled with the incompressibility constraint (Eq. 2.2) (*Moresi & Solomatov, 1995*). Hence, the mass and momentum equations may be written in the following matrix form:

$$\mathrm{Au} + \mathrm{Bp} = \mathrm{f} \qquad 2.11$$

$$\mathrm{B^T u} = 0 \qquad 2.12$$

where A is the "stiffness' matrix; u is a vector of unknown velocities; b is the discrete gradient operator; p is a vector of unknown pressure; and f is a vector composed of the body and boundary forces acting on the fluid. The parameters A, B and f are obtained using a standard finite element formulation with linear velocity and constant shape function.

Equation 2.11 can be transformed by multiplying B^TA^{-1} and using the equation 2.12 to remove the unknown velocities:

$$\mathrm{B^T A^{-1} Bp} = \mathrm{B^T A^{-1} f} \qquad 2.13$$

This is the Uzawa algorithm and it is solved using an iterative conjugate gradient method. The conservation of energy (Eq. 2.4) is solved using a streamline upwind Petrov-Galerkin method (*Brooks & Hughes, 1982*).

The Lagrangian tracer particles are used to carry the composition within the model domain in a time-depend manner (*van Hunen et al., 2002*). This method is applied to solve the equation 2.5. A large number of tracers per element is initial in place at t=0 Myr in a uniform, random spatial distribution into the model domain. Hence, every element must contain a minimum particle density for the success of the method. However, the dispersion of particles may occur in the presence of strong velocity gradients due to locally, high viscosity contrasts,

and to avoid significant gaps or clustering in the particle distribution the CVI method is applied (*Wang et al., 2015*). These particles are advected within the solid flow at each time step and then, interpolated to the integration points of the element. The composition function, *C* is included within a range of *C= [0;1]*, where *C=1* represents the crustal material while *C=0* is the mantle material. The resulting spatial distribution of tracers during the model computation leads to determine the density of the mantle and plate materials, which in turn, define the buoyancy forces.

The Lagragian tracers and the marcher-in-cell methods are also used to advect the temperature to solve the advection term in energy equations (Eq. 2.4) and avoid temperature numerical diffusion (*Gerya & Yuen, 2003*).

2.3 Rheological laws

Mantle and the overlying lithospheres are the key-parameters of the plate tectonics. Despite the uncertainties related to the mantle and plate rheology, measurements inferred from post-glacial redound and geoid anomalies can help to get an overview the Solid-Earth state.

Within the frame of geological timescales, the mantle behaves like a fluid. To first order, it is assumed that the mantle deforms as a viscous fluid under temperature and stress dependency. Laboratory studies have shown that the mantle olivine minerals may deform according to two main mechanisms: the diffusion and the dislocation creep mechanisms *(Hirth & Kohlstedt, 1995; Karato et al., 1986; King, 2016*).

The flow law that rules a single-state creep mechanism in the mantle is defined in (*Karato & Wu, 1993*), as follows (Table 2.2);

$$\dot{\varepsilon} = A\,\tau^{m} d^{-n} \left[\frac{E+pV}{RT}\right] \qquad 2.14$$

On one hand, the diffusion creep mechanism is limited by the diffusion of atoms or vacancies through the grains that compose the mineral. Here, the stress-dependence is linear (n=1), while the grain-size does matter (m=2-3). On the other hand, the dislocation creep mechanism, the deformation within the mineral is limited by the dislocation of the atoms into the mineral.

Therefore, the stress dependence is non-linear (n=3-5), while the grain size does not act onto this mechanism (m=0). See table 2.2 for parameters meanings.

From the equation 2.14, the viscosity can be deduced from the following relationship;

$$\eta = \frac{\tau}{\dot{\varepsilon}} \qquad 2.15$$

Hence, by replacing into the equation 2.15 the strain rate from the equation 2.14, we obtain;

$$\eta = A^{\left(\frac{-1}{m}\right)} \varepsilon^{\left(\frac{1-n}{n}\right)} \exp\left[\frac{E+pV}{nRT}\right] \qquad 2.16$$

Both diffusion and dislocation creep mechanisms act on the upper mantle. According to the equation 2.16, we define an effective viscosity calculated at each node of the elements. Hence, the effective viscosity is the minimum of the viscosity deriving from the diffusion or dislocation creep mechanisms (Table 2.2).

$$\eta_{eff} = \min\left(\eta_{diff}, \eta_{disl}\right) \qquad 2.17$$

According to the measurements of post glacial rebound *(Forte & Mitrovica, 1996; Sigmundsson, 1991*), geoid anomalies (*Hager et al., 1985; Haxby & Turcotte, 1978; Richards & Hager, 1984*), and seismic azimuthal anisotropy *(Behn et al., 2004; Hess, 1964; Richards & Hager, 1984*) the average viscosity of the upper mantle is admitted to be within the range of 5×10^{19} Pa s to 10^{21} Pa s. In light of this, we use the reference mantle viscosity for our models of 10^{20} Pa s. However, this reference viscosity is not constant in time, it changes since the viscosity is stress and temperature-dependent (Eq. 2.16).

The rheology of the lithospheres behaves differently due to the temperature variations from the surface to the base of the lithosphere. It conducts two modes of deformations; brittle and ductile. From the surface to the base of lithospheres, the temperature and pressure become higher, leading to a gradient from brittle to ductile deformation. For our models, the use equations 2.18 and 2.19 are taken for lithospheres.

At low temperature and mainly close to the surface the lithosphere may deform by brittle rheologies and its viscosity is defined as follows;

$$\eta = \frac{\sigma_y}{\dot{\varepsilon}_{II}} \qquad 2.18$$

σ_y is the yield strength, defined as;

$$\sigma_y = \min(\sigma_0 + fcP_0, \sigma_{max}) \quad 2.19$$

Where σ_{max} is the maximum yield strength and $\sigma_0 + fc\ P_0$ is the Byerlee law (*Byerlee, 1978*). With the surface yield strength; *fc* the friction coefficient and p_0 the lithostatic pressure (Table 2.2).

Thus, the Byerlee viscosity can be expressed as;

$$\eta_{Byerlee} = \frac{\min(\sigma_0 + fcP_0, \sigma_{max})}{\dot{\varepsilon}_{II}} \quad 2.20$$

The Byerlee viscosity is thus, considered to be integrated into the effective viscosity of the model. The equation 2.17 becomes;

$$\eta_{eff} = \min(\eta_{diff;disl}, \eta_{Byerlee}) \quad 2.21$$

In order to avoid non-realistic surface strength due to the strong temperature-dependence of the viscosity, at T=0°C; a maximum viscosity η_{max} of 10^{24} Pa s is imposed.

Symbol	Parameter	Unit	Value
	Rheological parameters		
	Creep mechanism		
ε	Strain	s^{-1}	-
τ	Yield stress	MPa	-
d	Grain size	m	-
m	Grain size exponent	-	-
n	Viscosity stress exponent	-	-
A	Pre-exponential flow law parameter	Pa s	-
E	Activation energy	$J \cdot mol^{-1}$	-
V	Activation volume	$m^3 \cdot mol^{-1}$	-
p	Pressure	Pa	-
R	Gas constant	$J \cdot mol^{-1} \cdot K^{-1}$	8.314
T	Temperature	K	-
η	Viscosity	Pa s	-
	Byerlee's plastic deformation		
σ_y	Yield strength	MPa	
ε_{II}	2^{nd} invariant of the strain rate	s^{-1}	-
f_c	Friction coefficient	-	0.2
σ_{max}	Maximum yield strength	MPa	300
σ_0	Surface yield strength	MPa	20
P_0	Lithostatic pressure	MPa	-

Table 2.2: Rheological laws parameters

2.4 Topography formulation

The surface topography of the Earth originates from crustal thickness lateral variations and the underlying mantle dynamics. To define the surface topography, we need to evaluate the vertical stress at the surface using the boundary flux method (*Zhong et al., 1993*). This method has been proven to be accurate to study the long wave-length topography, larger than 1000 km (*Crameri et al., 2012; Zhong et al., 1996*).

In our models, the surface stress can be translated into an effective surface topography using the density contrast between the lithosphere and the surface media such as the water on the subducting plate and the air on the continental part (Table 2.3).

$$\mathrm{H_{surf}}(\mathrm{x}, \mathrm{z}=0) = \frac{\overline{\sigma_{zz}}(\mathrm{x},\mathrm{z}=0)\eta_0 \frac{\kappa}{\mathrm{H}^2}}{\Delta\rho \mathrm{g}} \qquad 2.22$$

Where H_{surf} is the surface topography, σ_{zz} is the dimensionless normal stress at top of the model, $\Delta\rho$ is the density contrast between lithospheres and the media (e.g., water or air), η_0 is the viscosity reference, κ is the thermal diffusivity and H the box height (Table 2.1). We calibrate the surface topography against the present-day average depth of mid-oceanic ridges about 2.9 km depth.

We consider the dynamic component of the topography as the non-isostatic part, which can be related to the underlying mantle flow. To obtain the dynamic topography, we remove the isostatic part form the total topography (Eq. 2.22).

$$\mathrm{H_{dyn}}(\mathrm{x}, \mathrm{z}=0) = \mathrm{H_{surf}}(\mathrm{x}, \mathrm{z}=0) - (\mathrm{Iso_{sub}} + \mathrm{Iso_{up}}) \qquad 2.23$$

Iso_{sub} is the isostasy of the subducting plate;

$$\mathrm{Iso_{sub}} = \frac{\int_0^{z_c} \mathrm{g}\,\rho_\mathrm{m}\mathrm{T}(\mathrm{z})\mathrm{dz}}{\Delta\rho_\mathrm{w}\mathrm{g}} \qquad 2.24$$

whereas Iso_{up} is the isostasy of the upper plate, obtained by the vertical stress due to the thermal and compositional variations;

$$\mathrm{Iso_{up}} = \frac{\int_0^{z_c}(\mathrm{g}\,\rho_\mathrm{m}\mathrm{T}(\mathrm{z}))+(\mathrm{gC}\Delta\rho_\mathrm{c})\mathrm{dz}}{\Delta\rho_{\mathrm{air}}\mathrm{g}} \qquad 2.25$$

Z_c is the integration depth assuming a compensation level at 300 km depth (*Turcotte & Schubert, 2002*), $\Delta\rho_w$ is the density contrast between water and mantle ($\Delta\rho_w = \rho_m - 1000$) and $\Delta\rho_{air}$ for $\Delta\rho_{air}=\rho_m$.

Symbol	Parameter	Unit	Value
	Topography's parameters		
σ_{zz}	Surface stress	MPa	-
η_0	Reference viscosity	Pa·s	10^{20}
κ	Thermal diffusivity	$m^{-2}\cdot s^{-1}$	10^{-6}
H	Box height	km	3000
$\Delta\rho$	Density variation	$kg\cdot m^{-3}$	-
ρ_m	Mantle reference density	$kg\cdot m^{-3}$	3300
$\Delta\rho_w$	Density contrast between water and mantle	$kg.m^{-3}$	2300
$\Delta\rho_{air}$	Density contrast between air and mantle	$kg.m^{-3}$	3300
g	Gravity	$m\cdot s^{-2}$	9.8
Z_c	Compensation level depth	km	300
C	Continental crust composition	$kg\cdot m^{-3}$	2700
H_{surf}	Effective surface topography	km	-
Iso_{sub}	Subducting plate isostasy	km	-
Iso_{up}	Upper plate isostasy	km	-
H_{dyn}	Dynamic topography	km	-

Table 2.3: Topography's parameters.

2.5 General boundary conditions

All models are performed in a Cartesian geometry. The box domain has a depth of 3000 km which correspond to the depth of the whole mantle from the surface to the core-mantle boundary. All boundaries are considered as an impermeable barrier to flow in the Cartesian box. Hence, the mantle convection is considered to be restricted by the size of the model domain.

To model the large-scale convection in the whole mantle, a stratified mantle sub-divide the mantle into the upper mantle from 0 to 670 km depth and the lower mantle from 670 to 3000 km depth. The 670 km depth discontinuity is considered as a combination of jump of viscosity of few orders of magnitude with the 670 km depth mantle phase transition. The viscosity contrast provides a resisting force to the slab penetration due to the strong coupling between the slab and the lower mantle viscosity (e.g., *Čížková & Bina, 2013*). The endothermic phase transition of the walsdeylite to post-spinel generates positive buoyancy forces that gets the slab ponding, at least temporarily into the upper mantle (*Agrusta et al., 2017; Christensen & Yuen, 1985*). The combination of both may inhibits the flow between the two mantle domains. In order to get a more realistic upper mantle rheology, the 410 km depth exothermic phase transition is also present. This discontinuity is characterized by the transformation of the Olivine into walsdeylite, leading to negative buoyancy force which enhances the slab pull force (e.g., *Agrusta et al., 2017; Christensen, 1995*).

In the subduction zones, strong deformations are mostly accommodated between the subducting and upper plates. In this zone, the stress is localized along a lithospheric fault. Near the surface, the strain is accommodated along the thrust where the shear is localized, producing earthquakes (*Cloos, 1992; Kohlstedt et al., 1995*). To perform model of subduction zone it is necessary to model this feature which decouples both lower and upper plates (*Satolli et al., 2014; Zhong & Gurnis, 1992*). To model the thrust fault, a narrow thin weak layer is added at the top of the subducting plate from the mid-ocean ridge and extends down to 200 km depth, following the arc-shape of the slab. This weak zone has a viscosity of 4 orders of magnitude less that the maximum viscosity of the plates in order to decouple both plates.

To study how slab behaves at depth and the resulting surface fingerprints, it is necessary that the upper and lower plate are able to move self-consistently with respect to the dynamic of the slab at depth. Indeed, the trench migration is a response to the underlying dynamic of the

slab and the mantle convection cell (e.g., *Agrusta et al., 2017; Christensen, 1996; Funiciello et al., 2003; Goes et al., 2017; Mao & Zhong, 2018*). For this reason, the possibility of the trench to move self-consistently with respect to the underlying dynamics is major and has to be included in the numerical model. Since one of the aims of this work is to unravel how the surface fingerprints of subduction zone may be affected by the slab dynamics at depth, the initial set up of models is chosen for each study case and it will be described in more detail in the following chapters.

For all model set up, a temperature field is initially defined. The thermal boundary conditions are 273 K at the surface and 2773 K at the bottom of the system. Hence, the thermal buoyancy generates a density contrast between the lithospheres and the underlying mantle.

The upper plate is mobile thanks to a MOR has been imposed on the right-hand side of the models. The upper plate extends from the right side of the model to the trench.

To avoid the problem of subduction initiation, the slab extends down to 200 km depth to provide the first slab pull force which drive the subduction system without imposed external forces. An initial slab bending radius the slab in imposed of 500 km. I choose this specific bending radius thanks to natural data which show that the present-day mean radius of slabs is of about 500 km (*Lallemand et al., 2005*).

The oceanic lithosphere follows the half space cooling model for a given plate age (*Turcotte & Schubert, 2002*) which increase from 0 Ma at the mid ocean ridge to the trench for a given age. On the subducting plate a mid-ocean ridge (MOR) is also imposed in order to keep the lower plate mobile (*Turcotte & Schubert, 2002*). A thin low viscosity layer of 10^{20} Pa s is present down to 200 km depth in order to facilitate the decoupling between the plates.

The size of the numerical domains in 2D and 3D ranges from 4500 to 9000 km wide and 3000 km deep. The rectangular non-uniform grid contains 2880 elements x 472 elements, where the element size varies from 2.5 km to 7.5 km. The highest resolution grid (2.5x2.5 km^2) is localized vertically from 0 km to 210 km depth and horizontally between -5250 km to 900 km. The

mechanical boundary conditions are free slip on all the boundaries; hence the flow is driven only by the internal buoyancy forces.

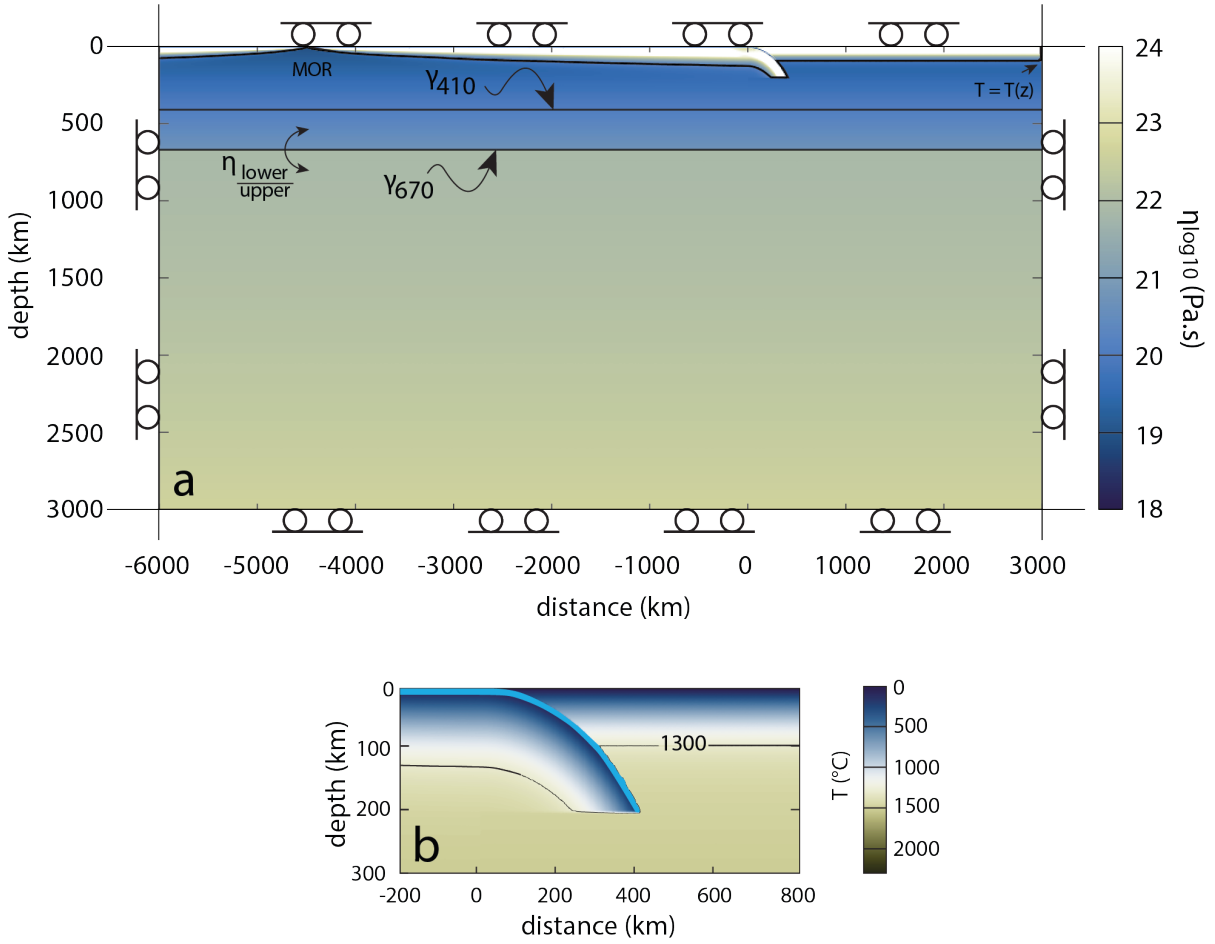

Figure 2.18: General Sketch of the model domain at t=0 Ma of a subducting lithosphere with an initial age at the trench of 100 Ma. The background colour indicates the viscosity, while the two horizontal black lines (γ_{410}, γ_{670}) represent the equilibrium position of the phase boundaries of olivine-wadsleyite at 410 km depth and the post-spinel transition at 670 km depth. The mid oceanic ridges (MOR) of the subducting plate and T=T(z) on the upper plate edge are also indicated. $\eta_{upper/lower}$ indicates the upper/lower mantle viscosity increases. Little rollers on the box sides represent the free slip boundary conditions. (b) Zoom-in on the subduction system. Background colour corresponds to the initial temperature conditions. Thick light-blue layer represents the weak layer that decouples the plates. Black solid line represents the 1300°C isotherm.

2.6 Resolution test

I performed three 2D numerical models of ocean-ocean single sided subduction zones to test the influence of the grid resolution on slab dynamics during slab free fall into the down to 1000 km depth (Fig. 2.19).

Simulations were computed on a 4500×3000 km^2 box discretized using a rectangular grid, with different finest grid sizes (2.5×2.5 km^2, 5×5 km^2, and 10×10 km^2). Mechanical boundary conditions are free slip on all the sides. The initial thermal structure of the lithosphere follows the half space cooling model (*Turcotte and Schulbert, 2002*). The initial thermal age of plates at the trench is set to 100 Ma which leads to a 100 km thick lithosphere. The thermal boundary conditions are 273 K at the surface and 2773 K at the bottom. The viscosity is pressure and temperature dependent. The reference viscosity of the box is set to 1×10^{20} Pa s. Two olivine phase transitions are assumed at 410 km depth (the ol-wd (γ_{410})) and at 670 km depth (rg-post-spinel (γ_{670})), set up at +2.5 MPa/K and -2.0 MPa/K, respectively (Fig. 2.19). The density increases for a mantle composed of 100 wt% of olivine associated with the phase changes are $\Delta\rho_{410}$ = 250 kg/m^3 and $\Delta\rho_{670}$ = 350 kg/m^3 for γ_{410} and γ_{670}, respectively. To determine the trench velocity, I track the trench position (with the initial location at x = 0 km) and its trench velocity (V_t = dXt/dt, positive if the trench advances with respect to the upper plate). For the subducting plate velocity, I measure the mean horizontal velocity of the lower plate from both 500 km far from the mid ocean ridge and from the trench (Fig. 2.19). To determine the slab thickness into the mantle transition zone, I track both sides of the slab density when reached the base of the upper mantle. I take also in this measurement of topography deflection triggered by the 670 km depth Clapeyron slope.

I use the model computed with the finest resolution grid (2.5 km^2) as reference model to evaluate the results obtained on more coarse meshes.

The dependence of the solution on the mesh size has been tested by increasing the cell size but keeping constant the ratio between the smallest and the largest sizes (equal to 1:3). Hence, I test mesh sizes of 2.5×7.5 km^2, 5×15 km^2 and 10×30 km^2. The slab thickness at the base of the upper mantle as well as the subducting plate velocity (Fig. 2.19d-e) are not particularly affected by the mesh size, since the error is less than 1%. In contrast, the trench velocities are more influenced by the mesh even if the associated variations do not exceed 10%

(Fig. 2.19f). A more coarse mesh size leads to a faster the trench motion. However, the overall slab morphology does not change significantly between the finest and coarsest meshes (Fig. 2.19a-c).

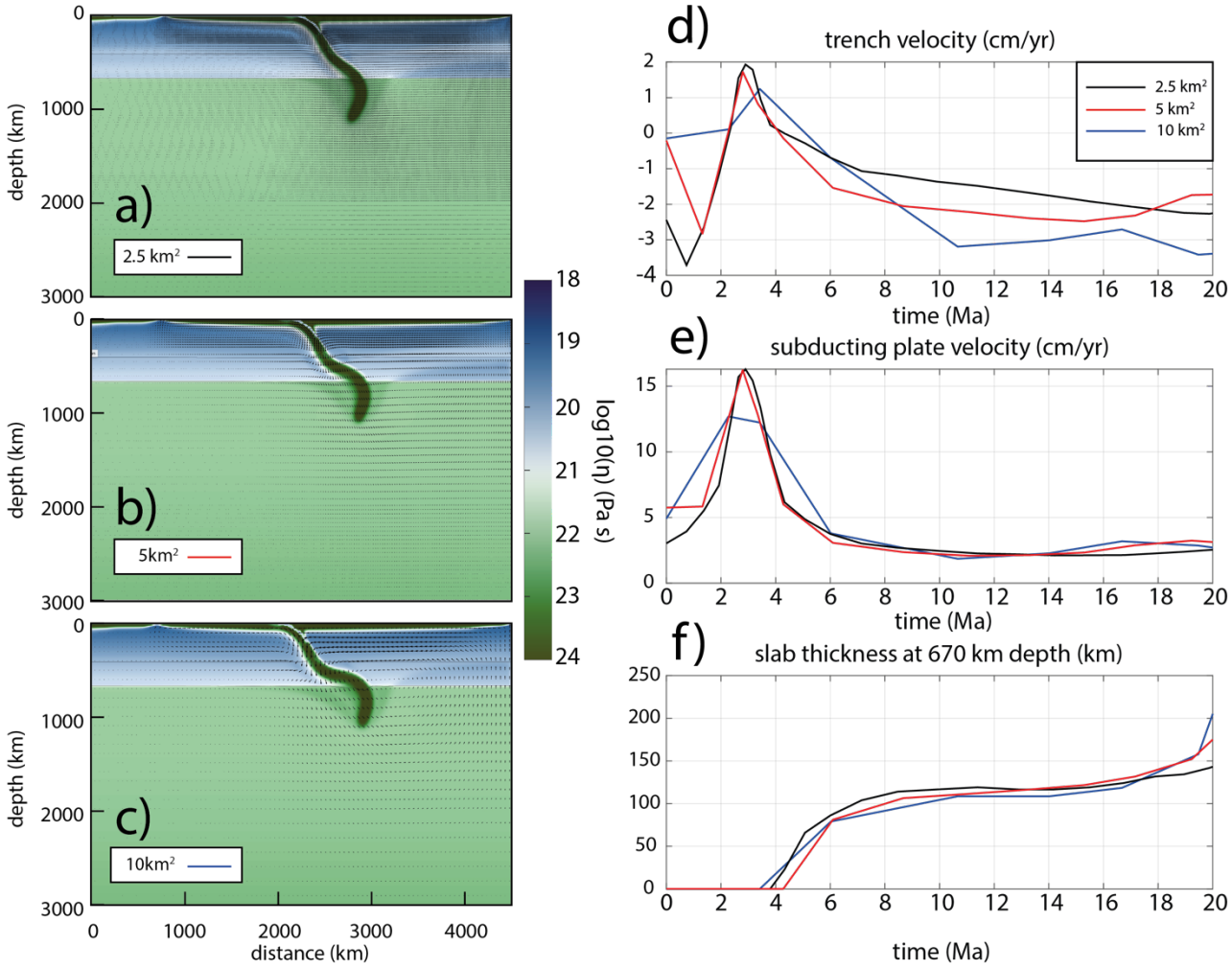

Figure 2.19: a, b, and c snapshots of models at 20 Ma. Model a) is the finest mesh resolution of 2.5 km^2. b) and c) coarser meshes of 5km^2 and 10km^2, respectively. Background colours is the viscosity. d), e) and f) are the diagnostic parameters.

Chapter III

Topographic fingerprint of deep mantle subduction

Abstract

The dynamic topography links with the mantle structures at various temporal and spatial scales. However, it is still unclear how it relates to the dynamics of subducting lithosphere when plates reach the mantle transition zone and lower mantle. Seismic tomography images show how slab morphologies vary from sinking sub-vertically into the lower mantle, to lying flat above the upper-lower mantle discontinuity, to thickening in the shallow lower mantle. These slab shapes have been considered to be the result of variable interaction of the slab with the upper-lower mantle discontinuity at ~670 km depth. Previous studies show that periodic deep slab dynamics can explain a variety of enigmatic geological and geophysical observations such as periodic variations of the plate velocities, trench retreat and advance episodes and the scattered distribution of slab dip angle in the upper mantle. In this study, we use two dimensional subduction models to investigate the surface topography expression and its evolution during the slab transition zone interaction. Our models show that topography does not depend on slab morphology; indeed, the dynamic topography cannot distinguish between a slab sinking straight into the lower mantle and slab stagnation at the upper-lower mantle boundary. However, topographic oscillations are related to episodes of the trench advance and retreat, which in turn are linked to the slab folding behaviour at transition zone depths. Our results suggest that the surface transient signal observed by geological studies could help to detect deep subduction dynamics.

3.1 Introduction

Topography is the product of processes occurring over diverse temporal and spatial scales, and the processes that shape the surface can be considered as the combination of three ingredients: the surface processes, the lithospheric isostatic adjustment and the deep mantle dynamics. The surface processes are mainly linked to tectonic and geomorphic processes (e.g., *Pérez-Peña et al.,* 2010; *Sembroni et al.,* 2016). Crustal and lithosphere deformation is accommodated by isostatic component, which is stable over long timescales, causing lateral density variations of the crust and the lithosphere which are balanced by rapid vertical adjustments (e.g., *Husson & Ricard,* 2004; *Kaban et al.,* 2004; *Watts,* 1978). Dynamic topography is related to stress acting at base lithosphere due to mantle convection and produce a transient signal on the surface (e.g., *Arnould et al.,* 2018*; Forte et al.,* 1993; *Gurnis,* 1990; *Hager & Richards,* 1989; *Lithgow-Bertelloni,* 1997; *Lithgow-Bertelloni & Silver,* 1998; *Liu & Gurnis,* 2010; *Mitrovica et al.,* 1989; *Panasyuk et al.,* 2000*; Zhong & Gurnis,* 1994). The dynamic topography is thus, expected to be particularly significant during subduction inducing vigorous mantle flow (e.g., *Duretz et al.,* 2011*; Mitrovica et al.,* 1989*; Zhong & Gurnis,* 1994). Slab shallowing, for example, is expected to produce down-warping of the upper plate and consequent marine transgression (e.g., *Gurnis,* 1990; *Liu et al.,* 2008; *Mitrovica et al.,* 1989). Variations in slab dip angle associated to slab folding, are correlated with oscillation of surface topography (*Cerpa et al.,* 2014; *Cerpa et al.,* 2015; *Guillaume et al.,* 2009; *Martinod et al.,* 2016), whereas downward tilt of the upper plate towards the subduction trench have been shown to be due to the interaction of the slab with the upper lower mantle discontinuity (*Crameri & Lithgow-Bertelloni,* 2017; *Hager,* 1984).

Seismic tomography shows that the cold lithosphere has a wide variability of dips and shapes at the both upper and lower mantle depths. In particular, at the base of the upper mantle, slabs appear either sink straight in the lower mantle or lay down horizontally above upper/lower mantle discontinuity (about 670 km) or even deeper around 1000 km (*Fukao & Obayashi,* 2013; *Van Der Meer et al.,* 2010; *Ricard et al.,* 1993; *Sigloch & Mihalynuk,* 2013). Several studies have highlighted the likely mechanisms that may control this slab variability at transition zone and lower mantle depth and it has been generally accepted that the viscosity contrast between the upper/lower mantle together with the endothermic ringwoodite to post spinel transition at 670 km depth hampers slabs penetration if subduction is accompanied by trench retreat (*Agrusta et al.,* 2017; *Christensen,* 1996; *Čížková & Bina,* 2013; *Garel et al.,* 2014; *Kincaid &*

Olson, 1987; *Mao & Zhong,* 2018). Moreover, the apparent thickening of some slabs into the lower mantle may be explained by the folding of slabs as soon as they start to interact with the mantle transition zone (MTZ) (*Běhounková & Čížková,* 2008; *Lee & King,* 2011; *Tosi et al.,* 2015). Indeed, Sigloch & Mihalynuk (2013) suggest that the thick lower mantle anomalies below the North America may be indicators of a remnant slab that piled up almost vertically near the MTZ before breaking and sinking into the lower mantle. Slab buckling and folding may be induced by strong slab pull forces linked to the 410 km discontinuity (i.e., olivine to wadsleyite (ol-wd) transition) and by a strong barrier to slab penetration due to the post-spinel phase transition (*Běhounková & Čížková,* 2008), by the reduction of the thermal expansivity with depth (*Tosi et al.,* 2015), or by the deformation of young and weak subducting plates *(Agrusta et al., 2018; Garel et al., 2014*).

Here, we use 2D numerical models to define the large-scale topography evolution of the upper plate during subduction. Our result indicates the deformation of the slab into the transition zone and its subsequent lower mantle penetration is marked by a specific topography fingerprint that can be used as a proxy of deep mantle slab dynamics.

3.2 Numerical approach and model setup.

3.2.1 Governing equations and model setup.

Single-sided subduction, lithospheric models are performed using CITCOM code (*Moresi & Gurnis,* 1996; *Wang et al., 2015*). The code uses the finite element method to solve the system of conservation of mass, momentum and energy equations for an incompressible fluid under the extended Boussinesq approximation (*Christensen & Yuen, 1985*), infinite Prandtl number, and without internal heating

$$\nabla \cdot \bar{\mathbf{u}} = 0 \tag{3.1}$$

$$\nabla[\bar{\eta}\,(\nabla\bar{\mathbf{u}} + \nabla\bar{\boldsymbol{u}}^{\boldsymbol{T}})] - \nabla \cdot \bar{P} = \bar{\alpha}_z\,\mathrm{Ra}\bar{T} - \mathrm{Ra_c}\sum_{i=1}^{n}\mathrm{Rb_i}\Gamma_i \tag{3.2}$$

$$\left[1 + \sum_{i=1}^{n}\left(\frac{d\bar{\Gamma}_i}{d\bar{z}}\,\bar{\gamma}_i^{\,2}\,\frac{\mathrm{Rb_i}}{\mathrm{Ra}}\,\mathrm{Di}(\bar{T} + \bar{T}_s)\right)\right]\left(\frac{\delta\bar{T}}{\delta t} + \bar{\mathbf{u}}\cdot\nabla\bar{T}\right) =$$

$$\nabla^2\bar{T} - \left[1 + \sum_{i=1}^{n}\left(\frac{d\bar{\Gamma}_i}{dz}\,\bar{\gamma}_i\,\frac{\mathrm{Rb_i}}{\bar{\alpha}_z\,\mathrm{Ra}}\right)\right]\bar{\alpha}_z\,\mathrm{Di}(\bar{T} + \bar{T}_s)\bar{\mathbf{u}}_z + \frac{\mathrm{Di}}{\mathrm{Ra}}\,\bar{\boldsymbol{\sigma}}\,\bar{\boldsymbol{\varepsilon}} \tag{3.3}$$

$$\frac{\delta C}{\delta t} + \bar{\mathbf{u}}\cdot\nabla C = 0 \tag{3.4}$$

where $\bar{\boldsymbol{u}}, \bar{\gamma}_i, \bar{P}, \bar{T}, \bar{T}_s, \bar{t}, \bar{z}, \bar{\alpha}_z, \bar{\boldsymbol{\sigma}}, \dot{\bar{\boldsymbol{\varepsilon}}}$ and $\bar{\eta}$ are the dimensionless (indicated by the upper bar) velocity, Clapeyron slope of i^{th} phase transition, pressure, temperature, surface temperature, time, depth, coefficient of thermal expansion, stress, strain rate and viscosity (Table 3.1). The parameters Ra, $\mathrm{Rb_i}$, $\mathrm{Ra_c}$ and Di are the thermal Rayleigh number, the boundary Rayleigh numbers associated with the phase transition, the compositional Rayleigh number, which represents the density variation between the continent and the underlying mantle, and the dissipation number, respectively. They are defined as follows:

$$\mathrm{Ra} = \frac{\alpha_0\,g\,\rho_m\Delta T\,H^3}{\kappa\,\eta_0};\ \mathrm{Rb_i} = \frac{g\,\Delta\rho_i\,H^3}{\kappa\,\eta_0};\ \mathrm{Ra_c} = \frac{g(\rho_c - \rho_m)\,H^3}{\kappa\,\eta_0};\ \mathrm{Di} = \frac{\alpha_0\,\rho_m H}{C_p} \tag{3.5}$$

The definition and the values of the parameters in Eq. 3.5 are listed in Table 3.1. The thermal expansion coefficient is defined as $\alpha_z = \exp(-1.1z)$, with z the depth in kilometres (*Tosi et al., 2013*). The advection term in the energy equation (Eq. 3.3) and the composition C (Eq. 3.4) are solved with the marker-in-cell method (*Gerya & Yuen, 2003*), where markers are advected at each time step by the solid flow and interpolated to the finite element integration points.

Mantle phase transitions are included in the models using a harmonic phase function (*Agrusta et al., 2014*). The relative fraction of the heavier phase is described by the phase function Γ, varying from 0 to 1 with respect to pressure and temperature, as follows:

$$\Gamma_i = 0.5 \left[1 + \sin\left(\pi \frac{\bar{z} - \bar{z}_i - \bar{\gamma}_i (\bar{T} - \bar{T}_i)}{\bar{d}_i} \right) \right] \quad 3.6$$

where $\bar{d}_i$ is the vertical width of the transition i, $\bar{z}_i$ and $\bar{T}_i$ are the depth and the temperature of the phase transitions at equilibrium conditions (Table 3.1).

The rheological model is assumed to be a combination of a diffusion creep and a pseudo brittle Byerlee rheology (*Agrusta et al., 2017*). The effective viscosity is thus, calculated from the viscosity of individual mechanisms (Eq. 3.7):

$$\eta_{eff} = \min\left(\eta_{diff}, \eta_{Byer} \right) \quad 3.7$$

with

$$\eta_{diff} = A_{upper,lower} \exp\left(\frac{E_{upper,lower} + PV_{upper,lower}}{RT} \right) \quad 3.8$$

and,

$$\eta_{Byer} = \frac{\min\left(\sigma_0 + f_c P, \sigma_{max} \right)}{\dot{\varepsilon}_{II}} \quad 3.9$$

The subscripts upper and lower refer to the upper and lower mantle respectively (Eq. 3.8). The others meaning for the parameters are shown in Table 3.1. For numerical stability, we consider a maximum viscosity of 10^{24} Pa s.

To define the effective long-wavelength surface topography we need to evaluate the vertical stress (σ_{zz}) at the surface, which is done using the consistent boundary flux method proposed by *Zhong et al.* (1993). This method has been proven to be accurate to study long wavelength topography (larger than 1000 km; *Crameri et al., 2012; Zhong et al., 1996*).

The surface normal stress can be translated into an effective surface topography using the density contrast between lithosphere and the surface media (i.e., water for the oceanic part and air for the continental part) using (*Turcotte & Schubert, 2002*):

$$H_{surf}(x, z = 0) = \frac{\overline{\sigma_{zz}}(x, z=0)\, \eta_0\, \kappa / H^2}{\Delta\rho\, g} \quad 3.10$$

Where H_{surf} is the surface topography, σ_{zz} is non-dimensional normal stress at the surface, $\Delta\rho$ the density contrast between lithospheres and the media (e.g., water or air), μ_0 the reference viscosity, κ the thermal diffusivity and H, the box height (Table 3.1). We calibrate the surface topography against the present-day average depth of the mid-ocean ridges about 2.9 km depth.

In this study we consider the dynamic component of the topography as the non-isostatic part, which can be related to the mantle flow. To obtain the dynamic component we remove the isostatic component from the total topography (Eq. 3.10).

$$H_{dyn}(x, z=0) = H_{surf}(x, z=0) - Iso_{subd} + Iso_{upper}) \quad 3.11$$

Iso_{subd} is the isostatic component associated to the subducting plate:

$$Iso_{subd} = \int_{z=0}^{z_c} g\, \rho m\, \alpha T(z)\, dZ / (\Delta\rho_w\, g) \quad 3.12$$

whereas Iso_{upper} is the isostatic component of the upper plate, obtained by vertical stress due to the thermal and compositional part:

$$Iso_{upper} = \int_{z=0}^{z_c} (g\, \rho_m\, \alpha T(z) + g\, C\, \Delta\rho_{cc})\, dZ / (\Delta\rho_{air} g) \quad 3.13$$

Zc is the integration depth by assuming a compensation level at 300 km depth, $\Delta\rho_w$ is the density contrast between mantle and water ($\Delta\rho_w = \rho_m - 1000$), and $\Delta\rho_{air}$ for mantle and air ($\Delta\rho_{air} = \rho_m$).

Symbol	Parameter	Unit	Value
	Global parameters		
H	Box height	km	3000
ΔT	Potential temperature drop	K	1350
$\Delta\rho_c$	Continental crust reference density	$kg \cdot m^{-3}$	2700
ρ_m	Mantle reference density	$kg \cdot m^{-3}$	3300
g	Gravity	$m \cdot s^{-2}$	9.8
α_0	Surface thermal expansion	K^{-1}	3×10^{-5}
κ	Thermal diffusivity	$m^{-2} \cdot s^{-1}$	10^{-6}
η_0	Reference viscosity	Pa·s	10^{20}
C_P	Heat capacity	$J \cdot kg^{-1} \cdot K^{-1}$	1250
R	Gas constant	$J \cdot mol^{-1} \cdot K^{-1}$	8.314
	Rheological model parameters		
	Diffusion creep		
$A_{upper,lower}$	Pre-exponential upper mantle	Pa s	1.87×10^9
	Pre-exponential lower mantle		2.29×10^{14} to 6.87×10^{15}
E	Activation energy upper mantle	$J \cdot mol^{-1}$	3×10^5
	Activation energy lower mantle		2×10^5
V	Activation volume upper mantle	$m^3 \cdot mol^{-1}$	5×10^{-6}
	Activation volume lower mantle		1.5×10^{-6}
	Byerlee's plastic deformation		
f_c	Friction coefficient	-	0.2
σ_{max}	Maximum yield strength	MPa	300
σ_0	Surface yield strength	MPa	20
	Mantle phase transition parameters		
$\gamma_{ol\text{-}wd}$	Clapeyron slope ol-wd transition	$MPa \cdot K^{-1}$	2.5 to 5
$\gamma_{post\text{-}spinel}$	Clapeyron slope wd/rd-ps transition	$MPa \cdot K^{-1}$	-0.5 to -3
$z_{ol\text{-}wd}$	ol-wd transition equilibrium depth	km	410
$z_{post\text{-}spinel}$	post-spinel transition equilibrium depth	km	670
$d_{ol\text{-}wd}$	ol-wd transition width	km	20
$d_{post\text{-}spinel}$	post-spinel transition width	km	20

$T_{ol\text{-}wd}$	ol-wd transition potential temperature	K	1423
$T_{post\text{-}spinel}$	post-spinel transition potential temperature	K	1423
$\Delta\rho_{ol\text{-}wd}$	ol-wd transition density contrast	$kg{\cdot}m^{-3}$	250
$\Delta\rho_{post\text{-}spinel}$	Post-spinel transition density contrast	$kg{\cdot}m^{-3}$	350

Table 3.1: Model parameters.

The size of the numerical domain is 9000 km wide and 3000 km deep (Fig.3.1b). The rectangular non-uniform grid contains 2880 x 472 elements where the element size varies from 2.5 km to 7.5 km. The highest resolution grid (2.5x2.5 km^2) is localized vertically from 0 to 210 km depth and horizontally between -5250 km to 900 km. The mechanical boundary conditions are free slip on all boundaries; hence the flow is driven only by internal buoyancy forces. The use of free-slip surface boundary appropriately simulates the large-scale (long-wavelength; $>10^3$ km) surface, dynamic and isostatic topography. However, this method fails to predict the short-wavelength ($<10^3$ km) topography variation as well as the topography resulting from the viscous plate bending (*Crameri et al., 2012*). The surface free-slip boundary is thus, suitable for studying the large-scale topography of the upper plate. The thermal boundary conditions are 273 K at the surface and 2773 K at the bottom. On the right-hand side a mid-ocean ridge (MOR) profile has been imposed, whereas a zero-heat flux has been imposed on the left-hand side (Fig. 3.1b). The temperature initial condition represents a subducting plate extended from the MOR, which is located at x = -4500 km, to the trench situated at x = 0 km, with a given age at the trench following the half space cooling model (*Turcotte & Schubert, 2002*). To avoid subduction initiation complications, an initial slab is present down to 200 km depth with a bending radius of 500 km (Fig. 3.1c). The upper plate extends from the right side to the trench, with a constant, initial thermal thickness of about 100 km. A continental crust is present on the upper plate with a thickness of 30 km with a density of 2700 kg/m^3. On top of the subducting plate, a 7.5 km thick low viscosity layer of 10^{20} Pa s is present down to 200 km depth in order to facilitate the decoupling between the plates (Fig. 3.1c).

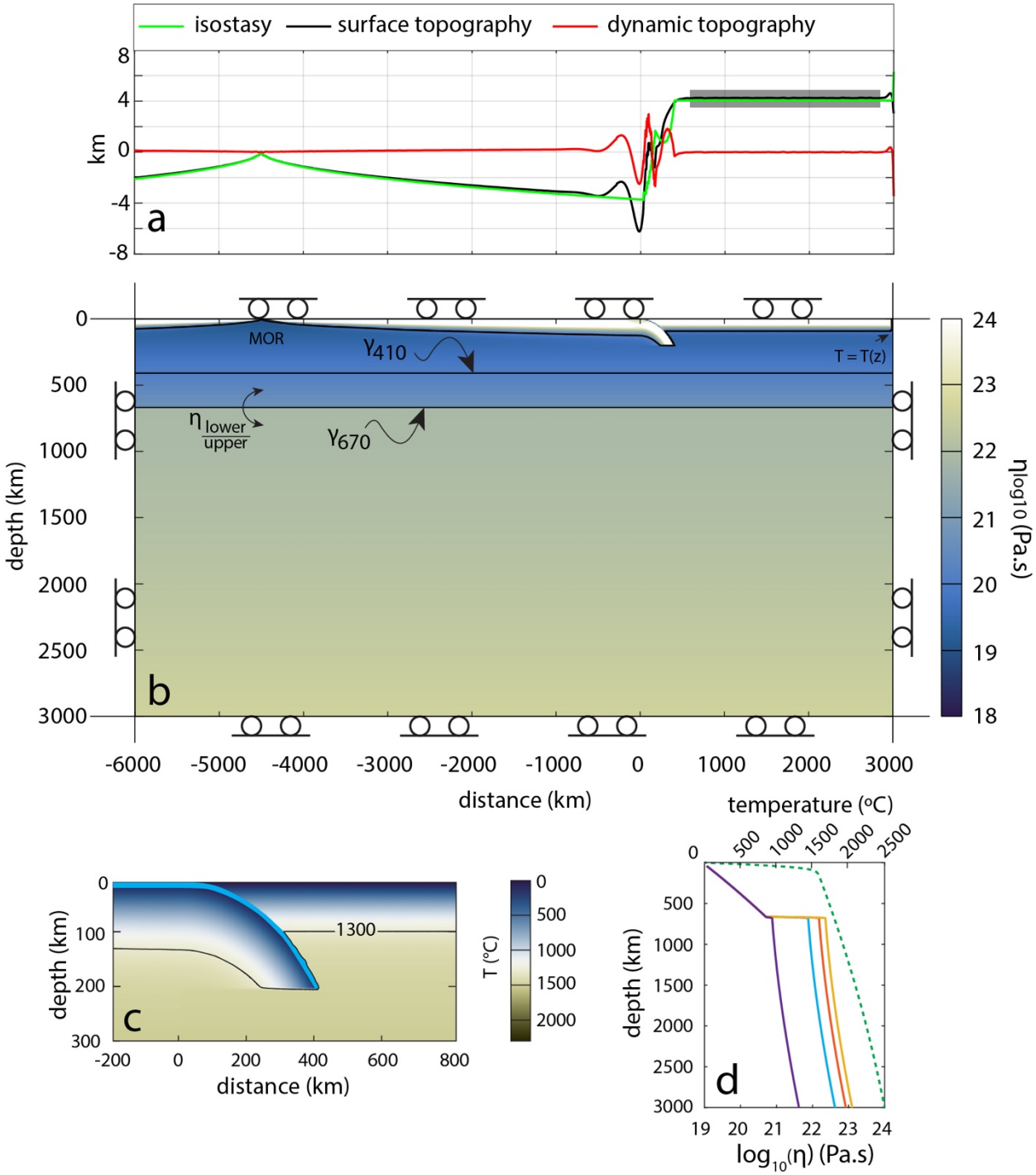

Figure 3.1 : (a) Surface topography (km) in black, with the isostatic and dynamic components in green and red, respectively, for the model domain at t=0 Ma. The grey area corresponds to the measured mean topography (large-scale) of the upper plate.(b) Sketch of the model domain at t=0 Myr of a subducting lithosphere with an initial age at the trench of 100 Myr. The background colour indicates the viscosity, while the two horizontal black lines (γ_{410}, γ_{670}) represent the equilibrium position of the phase boundaries of olivine-wadsleyite at 410 km depth and the post-spinel transition at 670 km depth. The mid oceanic ridges (MOR) of the subducting plate and null heat-flux upper plate edge are also indicated. $\eta_{upper/lower}$ indicates the upper/lower mantle viscosity increases. Little rollers on the box sides represent the free slip boundary conditions. (c) Zoom-in on the subduction system. Background colour corresponds to the initial temperature conditions. Thick light-blue layer represents the weak layer that decouples the plates. Black solid line represents the 1300°C isotherm. (d) Viscosity (solid lines) and temperature (dashed line) MOR profiles used in this study.

3.2.2 Investigated parameters

The aim of this work is to investigate the impact of the slab-upper/lower mantle discontinuity interaction on the surface topography. A combination between mantle (i.e., viscosities, phase transformations) and slab properties (i.e., strength and buoyancy) determines the slab behaviour at the mantle transition zone (*Agrusta et al., 2017; Christensen, 1996; Garel et al., 2014*). We systematically vary these parameters.

Two olivine phase transitions are assumed at 410 km depth (the ol-wd (γ_{410})) and at 670 km depth (rg-post-spinel (γ_{670})). We investigate a Clapeyron slope range of ol-wd from +2.5 MPa/K to +5.0 MPa/K, and of post-spinel from -3.0 MPa/K to -0.5 MPa/K (e.g., *Faccenda & Zilio, 2017*). The density increases for a mantle composed of 100 wt% of olivine associated with the phase changes are $\Delta\rho_{410}$ = 250 kg/m^3 and $\Delta\rho_{670}$ = 350 kg/m^3 for γ_{410} and γ_{670}, respectively (e.g., *Faccenda & Zilio, 2017*). The averaged upper mantle (averaged between 0 km and 670 km depth) viscosity is set to be about 10^{20} Pa s at mantle temperature. The averaged viscosity of the lower mantle (averaged between 670 km and 3000 km depth) is within a range of 10^{21} to 5x10^{22} Pa s (*Čížková et al., 2012; Forte et al., 2002*). The initial subducting plate age (i.e., A_{plate}), regulating the slab strength and buoyancy, is varied between 25 Ma and 150 Ma (Table 3.2). To determine whether the trench advances or retreats with respect to the upper plate during the subduction evolution, we track the trench position (with the initial location at x = 0 km) and its trench velocity (V_t = dXt/dt, positive if the trench moves towards the subducting plate). We consider the convergence velocity, defined as $V_{conv} = V_{subd} - V_t$, (with V_{subd} the subducting plate velocity) as a proxy to the slab pull force. For the topographic investigations, we observe throughout our models, sharp variations along of the surface topography. This topographic variations are due to the sharp transition in density between the continental crust and the ocean once the upper plate moves towards the subducting plate. To avoid this issues, we ignore these artefacts. We thus, measure the average surface topography (Eqs. 3.11-3.13) on the central part of the upper plate, between 800 km from the trench and x = 2200 km in time. Our study then focuses on the large-scale topographic variation of the upper plate (H_{surf}, H_{dyn}). We also measure the dynamic topography rate ($Dyn_{rate} = dH_{dyn}/dt$).

In order to discriminate between different slab behaviours and morphologies interactions, we define two diagnostic measured quantities. The following quantities are evaluated starting from the time the slab reaches 670 km depth (t_{670}), which roughly indicates the time when the slab begins to interact with the upper/lower mantle discontinuity. We measure the width of the

slab in the transition zone (W_{slab}) and the maximum slab depth (Z_{slab}) over time (Fig. 3.2a). Those measurements will help us to separate our models into different slab categories. A slab that sinks straight into the lower mantle will display a relatively constant W_{slab}, close to the initial thickness of the subducting plate and will display an increase of Z_{slab} through time (Category 1, Fig. 3.2). A slab that stagnates in the transition zone will show a nearly linear increase of the W_{slab} and a relatively constant (Z_{slab}) (Category 2, Fig. 3.2). A slab folding while passing through the mantle transition zone will show oscillations of W_{slab} and a constant increase of Z_{slab} (Category 3, Fig. 3.2). Finally, a slab that will buckle and stagnate for a while in the transition zone, before sinks in the lower mantle, will show an increase of W_{slab} together with an almost constant Z_{slab} (similar to the Category 2), during the period of stagnation and buckling, followed by a decrease of W_{slab} and increases of Z_{slab}, for the period of lower mantle sab sinking (Category 4, Fig. 3.2). For the example of category 4 shown in figure 3.2 the lower mantle sinking occurs at ~60 Myr. W_{slab}, Z_{slab} and t_{670} are used to define the two dimensionless values t_{fold} and D. t_{fold} is defined as:

$$t_{fold} = \frac{t_{slab}}{t_{670}} \quad 3.14$$

where t_{slab} corresponds to the time needed by the slab to stagnate, and it is the time during which (W_{slab} - <W_{slab}>)>0 is satisfied, with <W_{slab}> the arithmetic average of W_{slab} in time and space. t_{fold} indicates thus, how much slab material it trapped in the transition zone and for how long.

The second parameter D is the ratio between the rate at which the slab accumulates in the MTZ, and the rate at which the slab sinks in the lower mantle ($D=(dW_{670}/dt)/(dz/dt)$).

$$D = \frac{W_{slab}(t_{end}) - W_{slab}(t_{670})}{Z_{slab}(t_{end}) - Z_{slab}(t_{670})} \quad 3.15$$

with t_{end}, the final time of the simulations. D is similar to the parameter defined by *Agrusta et al.* (2018), and it indicates whether the slab is more prone to sink in the lower mantle or to get trapped in the mantle transition zone. A slab that does not accumulate into the MTZ will have both t_{fold} and D less than 1. On the contrary, these variable will be larger than 1 for a hypothetical slab that will be trapped or interacting for longer time into MTZ.

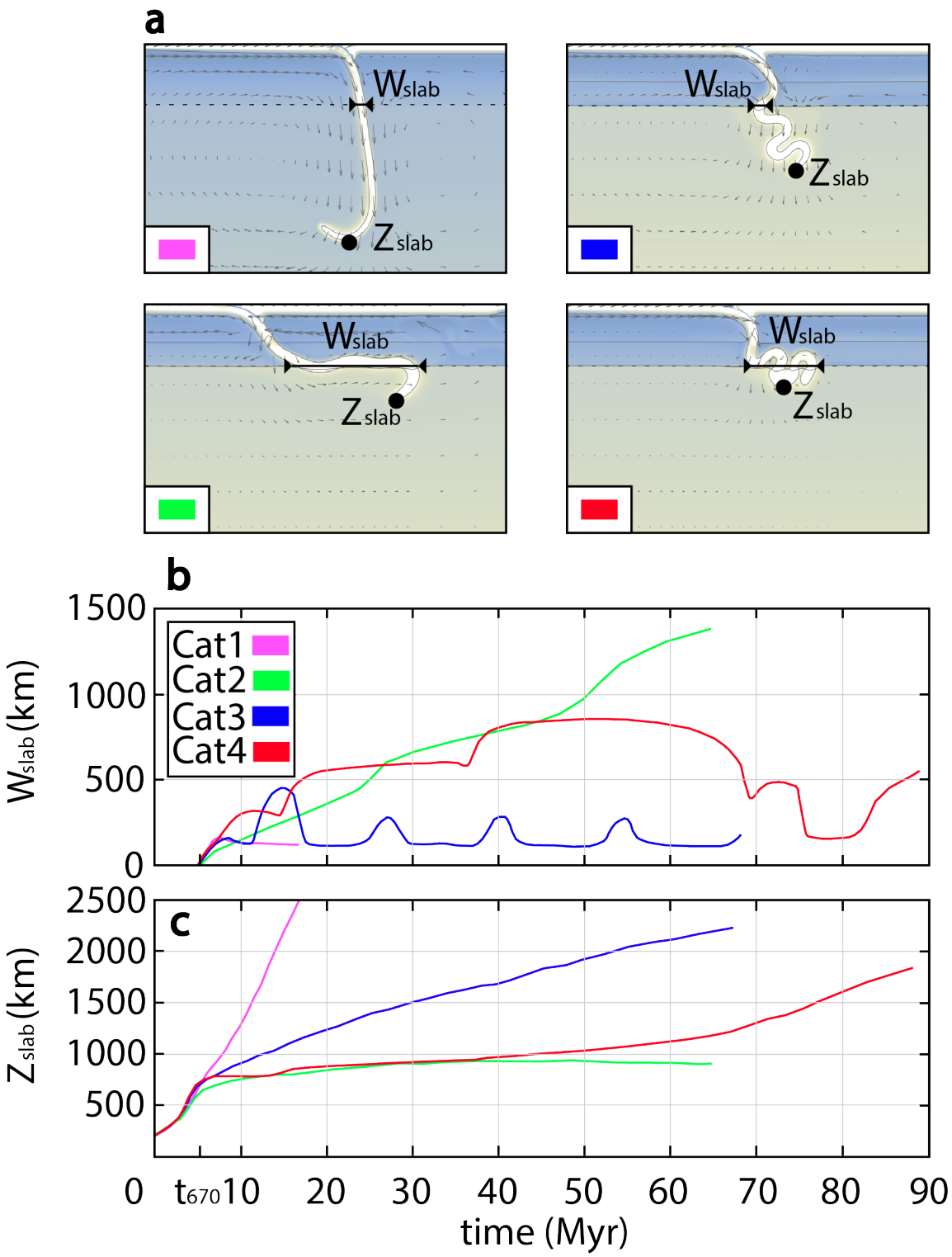

Figure 3.2 : a) Snapshots of four slab-MTZ interaction modes, and with the definition used to measure the width of the slabs at 670 km (W_{slab}) and slab tip depth (Z_{slab}). b) W_{slab} and c) Z_{slab} through times for the four cases in (a).(Cat1) Category1: slab sinking straight into the lower mantle (Cat2) Category2: slab flattening into the MTZ; (Cat3) Category3: folding slab through the whole mantle; (Cat4) Category4: slab folding into the MTZ and slab avalanche.

3.3 Results

We performed 33 simulations (Table 3.2) of self-consistent single-sided 2D subduction with the aim to study the expression of the slab dynamics on the surface. In this section we first describe a reference model of a slab sinking straight into the lower mantle in a simplified setup that does not include mantle phase transitions and presents a relatively weak lower mantle (with an averaged viscosity of 10^{21} Pa·s) (Table 3.2). Next, we systematically modify the reference model by changing the strength of the ol-wd and rg-to-post-spinel transitions (γ_{410}; γ_{670}), the prefactor term for the lower mantle viscosity (A_{lower}), and the initial age of the subducting plate (A_{plate}).

In order to describe the deep slab evolution and the corresponding surface expression, we describe the evolution of the model during three distinct phases (e.g., *Funiciello et al., 2003*), corresponding to three states of slab sinking in the mantle. The 1st phase corresponds to the interval in which the slab sinks through the upper mantle and last until the slab reaches the 670 km depth discontinuity at the t_{670}. The 2nd phase occurs during the slab interaction with the upper/lower mantle boundary at 670 km depth when the slab tip depth is stagnating between 670 and 1000 km depths. The 3rd phase is after slab interaction with the 670 km depth discontinuity when the slab propagate deeper into the lower mantle (Fig. 3.2).

Model number	γ_{410} (MPa/K)	γ_{670} (MPa/K)	A_{lower} (Pa s)	A_{plate} (Ma)	t_{670} (Ma)	W_{slab} (km)	Z_{slab} (km)	Category
0	0	0	$2.29x10^{14}$	100	6.0	126	2271	1
1	+2.5	-0.5	$2.29x10^{15}$	100	6.0	168	1628	1
2	+2.5	-1.0	$2.29x10^{15}$	100	6.0	211	1574	1
3	+2.5	-1.5	$2.29x10^{15}$	100	6.1	256	1500	1
4	+2.5	-2.0	$2.29x10^{15}$	100	6.0	1446	1111	2
4c	+2.5	-2.0	$6.87x10^{15}$	100	6.0	1387	923	2
4g	+2.5	-2.0	$2.29x10^{15}$	150	5.8	1502	1187	2
5	+2.5	-2.5	$2.29x10^{15}$	100	6.0	1368	1042	2
6	+2.5	-3.0	$2.29x10^{15}$	100	6.0	843	931	2
7	+3.0	-1.5	$2.29x10^{15}$	100	6.0	266	1252	1
8	+3.0	-2.0	$2.29x10^{15}$	100	6.0	1275	1088	2
9	+3.5	-3.0	$2.29x10^{15}$	100	6.0	646	884	3
10	+4.0	-0.5	$2.29x10^{15}$	100	6.0	354	1236	3
11a	+4.0	-2.0	$2.29x10^{14}$	100	6.0	248	1642	1
11b	+4.0	-2.0	$2.29x10^{15}$	100	6.0	578	1679	3
12	+4.0	-2.5	$2.29x10^{15}$	100	6.0	612	1433	3
13	+4.0	-3.0	$2.29x10^{15}$	100	6.0	639	908	3
14	+5.0	-0.5	$2.29x10^{15}$	100	6.0	369	1590	3
14e	+5.0	-0.5	$2.29x10^{15}$	50	6.2	356	1401	3
14f	+5.0	-0.5	$2.29x10^{15}$	150	5.9	341	1770	3
15	+5.0	-1.0	$2.29x10^{15}$	100	6.1	432	1644	3
15c	+5.0	-1.0	$6.87x10^{15}$	100	6.0	526	1260	3
16	+5.0	-1.5	$2.29x10^{15}$	100	6.0	476	1606	3
17a	+5.0	-2.0	$2.29x10^{15}$	100	6.0	526	1260	3
17c	+5.0	-2.0	$6.87x10^{15}$	100	6.1	627	1135	3
17f	+5.0	-2.0	$2.29x10^{15}$	150	5.7	560	1668	3
18	+5.0	-2.5	$2.29x10^{15}$	100	6.0	587	1221	3
19a	+5.0	-3.0	$2.29x10^{14}$	100	6.0	167	1650	1
19b	+5.0	-3.0	$2.29x10^{15}$	100	6.0	861	1832	4
19c	+5.0	-3.0	$4.58x10^{15}$	100	6.1	1011	1472	4
19d	+5.0	-3.0	$6.87x10^{15}$	100	6.1	1406	1213	4

19e	+5.0	-3.0	$2.29x10^{15}$	25	6.4	570	1966	4
19f	+5.0	-3.0	$2.29x10^{15}$	50	6.3	703	1950	4
19g	+5.0	-3.0	$2.29x10^{15}$	150	5.8	905	1934	4

Table 3.2: List of models with their input variables: phase transition, lower mantle and the initial age of the plate at the trench (A_{plate}). Output variables including: the maximal values of slab length (W_{slab}) and depth (Z_{slab}), the time to reach the 670 km discontinuity (t_{670}) and the category to which each slab is belonging to**.**

3.3.1 Reference model

Previous models have shown that both a weak lower mantle viscosity and a weak mantle endothermic transition (γ_{670}) facilitate slab penetration in the lower mantle (*Goes et al., 2017*). Hence, our reference model is characterized by the absence of mantle phase transitions and a relatively weak lower mantle, with an initial subducting plate of 100 Ma (Table 3.2, model 0).

During the 1st phase, the slab sinks freely into the upper mantle until it reaches the base of the upper mantle (Fig. 3.3a). The dynamic topography profile remains flat around 0 km without significant lateral variations in space (Fig. 3.3a top). During this phase, the convergence velocity (V_{conv}) accelerates from 2 cm/yr to ~5 cm/yr, suggesting an increase in the slab pull force (Fig. 3.3d). At the surface, the trench moves towards the upper plate with velocity (V_t) passing from 4 cm/yr to 2.5 cm/yr (Fig. 3.3f). The topography of the upper plate during this phase remains roughly constant through time, with an averaged elevation (H_{surf}) of 1 km above the sea level with a negligible averaged dynamic component (H_{dyn} = 0 km) (Fig. 3.3c, e).

After penetrating into the lower mantle, the slab shows a sub-vertical and linear morphology with a folded tip edge due to the slight increasing lower mantle viscosity (Fig. 3.3b). Yet, the dynamic profile along the upper plate remains stable but pulled down to ~0 km elevation (Fig. 3.3b top). During the slab descent, the V_{conv} increases up to ~ 10 cm/yr (Fig. 3.3d), while, V_t suggests trench advance (Fig. 3.3f). The large-scale surface topography of the upper plate (H_{surf}) decreases through time, until reaches about 800 m above the sea level at end of the simulations (t_{end}) (Fig. 3.3c). The same trend is observed on the dynamic topography that shows a slow subsidence of 200 m over 7 Myr (Fig. 3.3e).

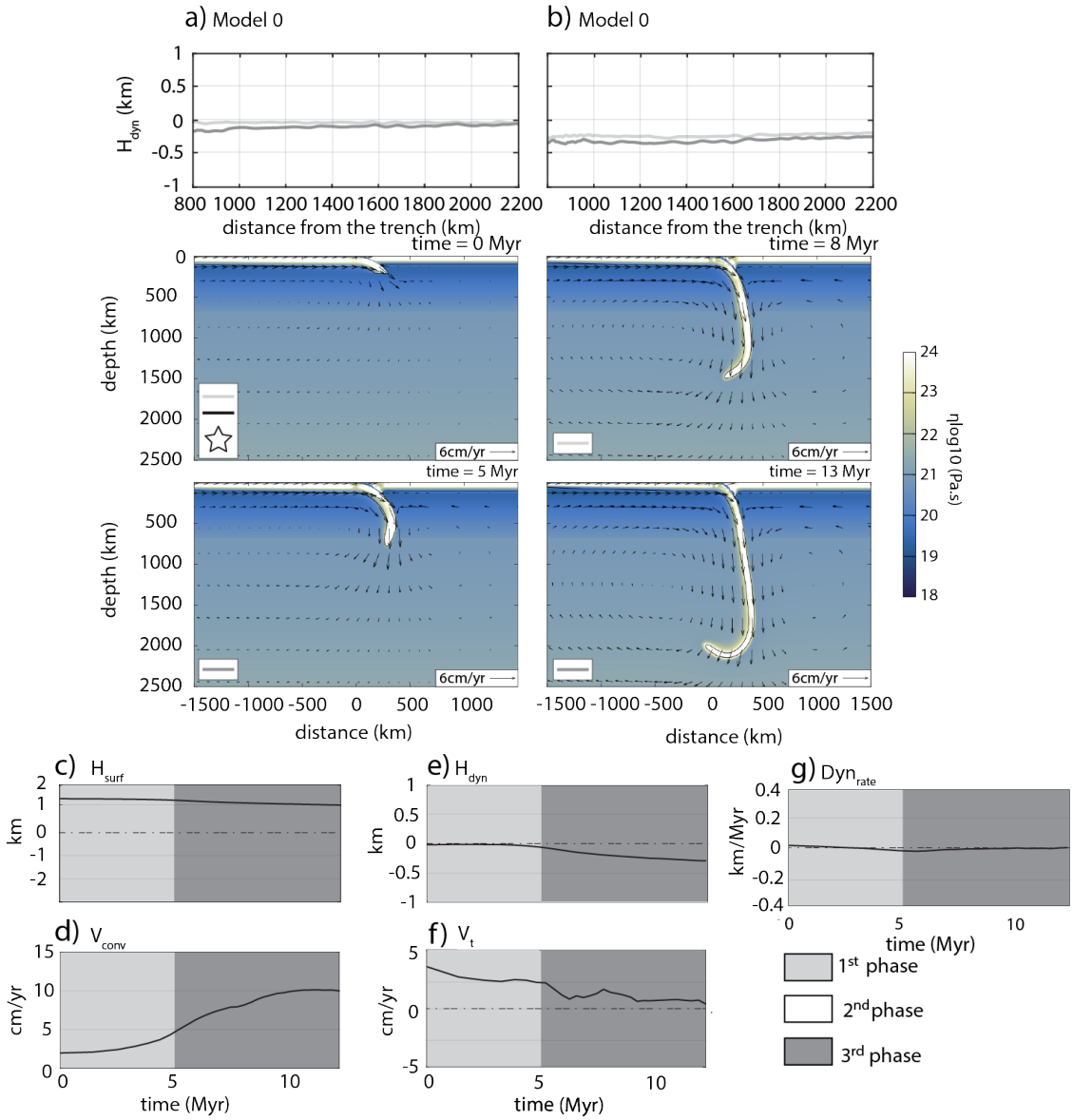

Figure 3.3 : (a, b) Selected time steps in the evolution of the reference model 0 (Table 3.2). Top: zoom in dynamic topography space and time domain. Bottom: zoom into the slab morphology. The colour represents the viscosity and the arrow the velocity field. The black solid line contour is the 1300 °C isotherm. Box in the bottom left corner shows the symbol that refers to the regime diagram in Figure 4.The dark and light grey symbols indicate the dynamic topography top plots. Time series of the surface topography (c), convergence velocity (d), dynamic topography (e), trench velocity (f), and the dynamic rate of the upper plate (g) of the current models.

3.3.2 Slab dynamics categories

The subduction behaviour at depth varies due to changes in the following geodynamical parameters with respect to the reference model: A_{plate}, γ_{410}, γ_{670} and lower mantle viscosity (hereafter indicated by the prefactor A_{lower}) (Table 3.2). To categorise slab interaction modes depending on the mantle and plate properties, we draw a diagram based on the output variables t_{fold} and D (Fig. 3.4). The models fall in four main categories:

- (Category 1, 'undisturbed slab') for $D < 1$ and $t_{fold} < 1$ the slab penetrates almost undisturbed in the lower mantle (similar to the reference model).

- (Category 2, 'flat slab') for $D > 1$ and $t_{fold} > 1$ the slab does not penetrate in the lower mantle.

- (Category 3, 'folding slab') for $D < 1$ and $1 < t_{fold} < 6$ the slab penetrates in the lower mantle, with folding episodes.

- (Category 4 'buckling slab and avalanche') for $D < 1$ and $t_{fold} > 6$ the slab, before to sink in the lower mantle, it gets trapped in mantle transition zone while folding.

We delineate $t_{fold} \approx 6$ as an arbitrary choice. Indeed, we observe throughout our models that $t_{fold} \approx 6$ is the limit between category 3 and category 4.

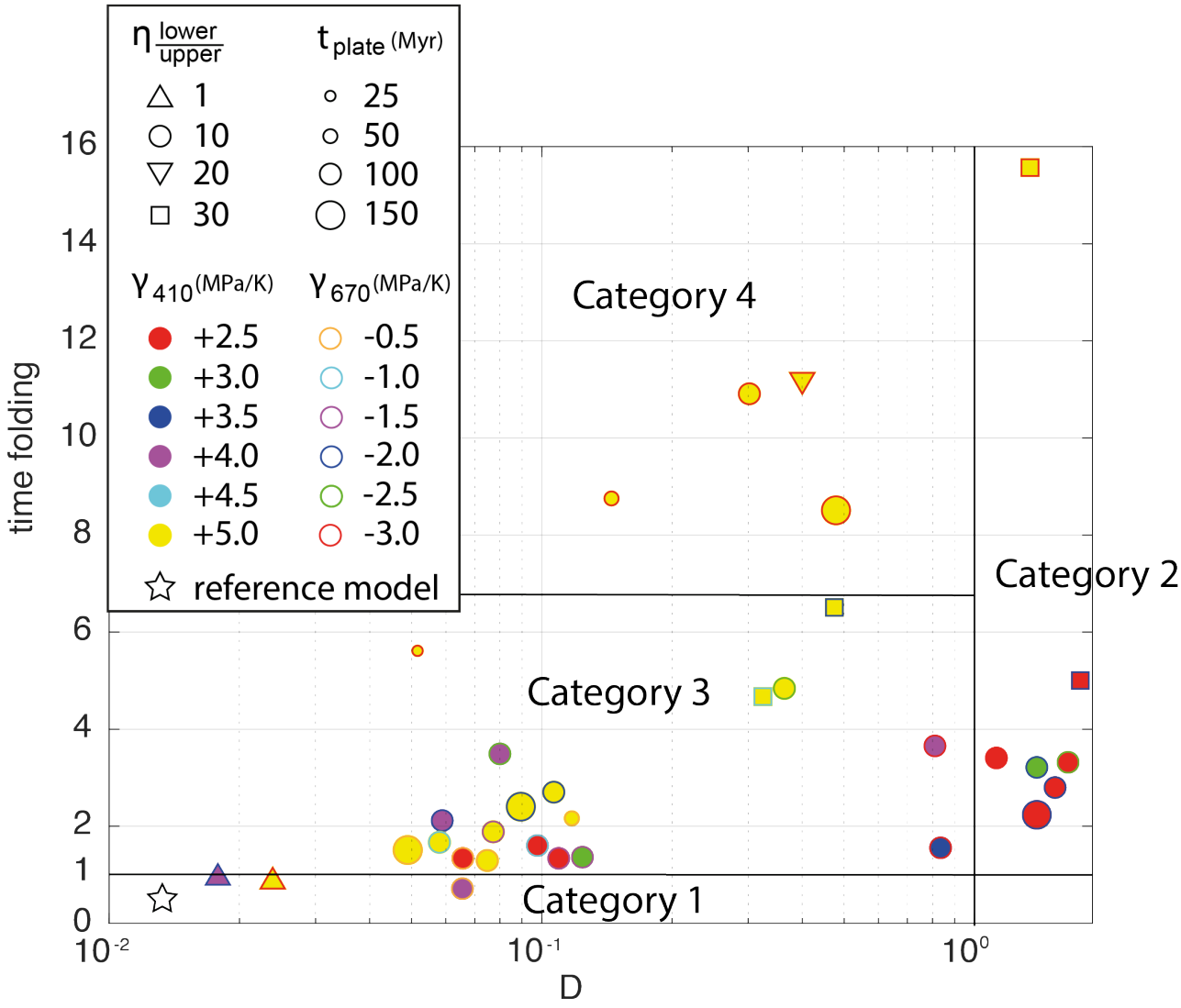

Figure 3.4 : Diagram plotting t_{fold} (time folding) against D. How indicate in the legend box: The shape of the symbols represents the lower mantle viscosity. The size of the symbols represents the initial subducting plate age (A_{plate}). The colour of the symbols represents the strength of ol-wd transition (γ_{410}). The colour of the edges of the symbols represents the strength of post-spinel transition (γ_{670}). Dashed black lines represent the domain borders: straight slab (category 1), flat slab (category 2), and folded slab (category 3).

A regime diagram summarising how the relative behaviour of slabs changes with phase-transitions strengths at the 410 km and 670 km depths is shown in Figure 3.5. Subducting plate age and lower mantle viscosity seem to give a weak contribution to cluster the slab categories, and we will describe their influence on the next sections. There are quite tight ranges of plausible conditions over which undisturbed slabs (Category 1), flattening slabs (Category 2) and buckling and flushing slabs (Category 4) are expected. In contrast, there is a quite wide range over which the folding slab behaviour exist (Category 3).

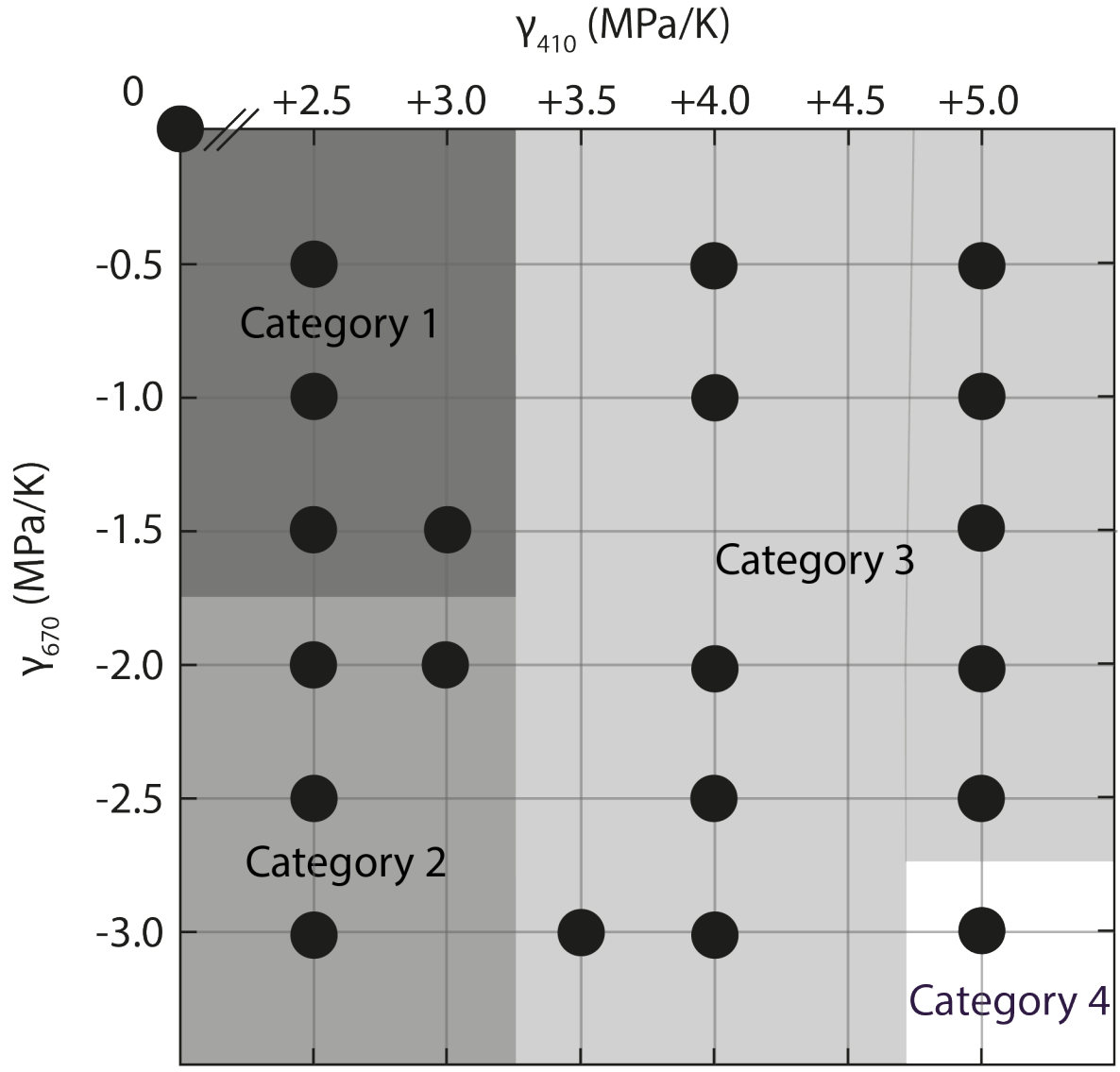

Figure 3.5 : Regime diagram plotting γ_{410} against γ_{670} at either fixed lower mantle viscosity (A_{lower} = 2.29x10^{15} Pa s) and A_{plate}=100 Myr. Each circle corresponds to a model. Shaded areas corresponds to slab categories : straight slab (category 1), flat slab (category 2), and folded slab (category 3) and folded and avalanche slab (category 4). These areas derive from the figure 3.4.

3.3.3 Undisturbed slab (category 1)

This undisturbed sinking category includes slabs that neither fold nor accumulate into the mantle transition zone, and their morphologies remain similar to the reference model, displaying a sub-vertical morphology extended from the surface to lower mantle (Fig. 3.6). We found that the simulations in this category are obtained with the lowest lower mantle viscosity (viscosity with prefactor A_{lower}<2.89x10^{14} Pa s) (Fig. 3.6; Table 3.2, models 0, 1, 10 and 19a). As expected, a weak lower mantle does not provide enough resisting force to make the slabs stagnate into the upper mantle which agrees with previous studies (e.g., *Agrusta et al., 2017*;

Mao & Zhong, 2018). The general evolution of those slabs morphology as well as dynamic topography profile (Fig. 3.6a, b tops) are similar to the reference model in which the effect of phase transitions was not included, and the only difference is the higher convergence velocity (V_{conv}), since that the presence of the ol-wd mantle phase transition enhances the slab pull (Fig. 3.6h). The trench shows an advancing trend and the topography a weak subsidence (Fig. 3.6c, e-g).

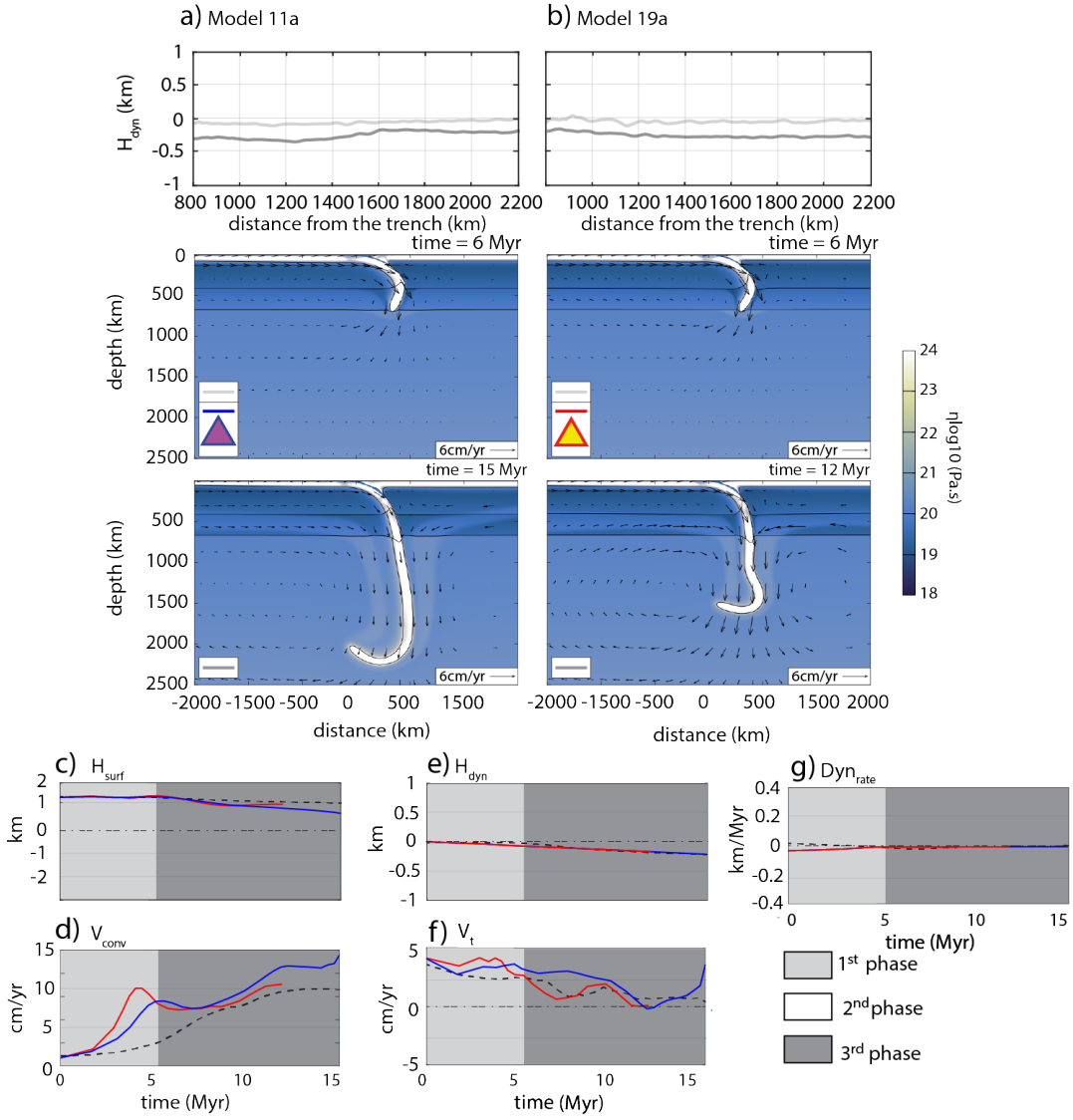

Figure 3.6 : (a, b) Selected time steps in the evolution of the reference model 10 and 19a (Table 3.2). Top: zoom in dynamic topography space and time domain. Bottom: zoom into the slab morphology. The colour represents the viscosity and the arrow the velocity field. The black solid line contour is the 1300 °C isotherm. Box in the bottom left corner shows the symbol that refers to the diagram in Figure 3.4.The dark and light grey symbols indicate the dynamic topography top plots. Time series of the surface topography (c), convergence velocity (d), dynamic topography (e), trench velocity (f), and the dynamic rate of the upper plate (g) of the current models. Dotted black lines are the reference model (Fig.3.3).

3.3.4 Flat slab (category 2)

Slabs belonging to this category stagnate into the transition zone (Fig. 3.7). This slab dynamics is promoted by a viscous lower mantle (viscosity prefactor of $A_{lower} \geq 2.29x10^{15}$ Pa s) (Table 2; Fig. 3.7), and by weak exothermic phase transition ($\gamma_{410} < +3.5$ MPa/K) combined with a strong endothermic one ($\gamma_{670} < -2$ MPa/K (Table 3.2; Fig. 3.7).

To study the evolution of this slab category we selected three simulations characterized by similar mantle phase transitions of ol-wd and post-spinel ($\gamma_{410} = +2.5$ MPa/K and $\gamma_{670} = -2$ MPa/K; Fig. 3.7) and different lower mantle viscosities and initial subducting plate ages. These models are shown the figure 3.7: the model 4 with A_{lower} of $2.29x10^{15}$ Pa s and A_{plate} of 100 Myr; the model 4g with an older A_{plate} of 150 Myr and the same lower mantle viscosity of the model 4; and the model 4c with A_{lower} of $6.87x10^{15}$ Pa s while the A_{plate} is the same as for model 4 (Table 3.2).

For each of the three simulations, the 1st phase where the slab freely falls in the upper mantle lasts about 6 Myr. The dynamic topography profile remains almost flat similar to the profile observed during the same phase for the reference model (Fig. 3.3a-c top). The trench moves towards the upper plate (V_t of ~1 cm/yr) while V_{conv}, speeds up gradually, about 3 cm/yr (Fig. 3.7e, g).

After reaching the upper-lower mantle discontinuity the slab tip folds and deforms into the MTZ (2nd phases). We observe that, as soon as the slab starts rolling back, a large-scale tilt toward the trench occurs for all models (Fig.3.7a-c top) , similar to results in (*Crameri and Lithgow-Bertelloni,* 2017; *Mitrovica, 1989*). The trench starts to retreat, following the roll back of the slab, with the highest trench velocity for the oldest plate and the slowest for the models with the more viscous lower mantle (Fig. 3.7g). These velocity differences are also observed for the convergence velocity, indicating an increase of the resisting force to the slab sinking in the lower mantle from the more viscous lower mantle and an increase of the driving force from the oldest plate (Fig. 3.7e, g). The topographic signals (H_{surf}; H_{dyn}) decrease abruptly for all models as soon as the slabs fold and retreat, with an intensity that does not depend by the slab or lower mantle properties (Fig. 3.7d, f). Along with the tilting, the mean topographies H_{surf} and H_{dyn} show a decrease of about 0.8 km and 0.3 km, respectively (Fig. 3.7d, f and h).

The 3rd phase is characterised by the deflection and stagnation of the slabs at the base of the upper mantle (Fig. 3.7a-c bottom). Despite the similarities between slab morphologies, slabs evolve differently depending on the mantle and slab properties. The younger slab shows undulations of the slab leading edge at the base of the upper mantle, whereas the older slab does

not exhibit such deformation (Fig. 3.7a-c bottom). Along with the young slab undulations in the MTZ, oscillations are observed in V_t (Fig. 3.7a, g). The amplitude of V_t during trench retreat motion depends on the slab strength: a younger slab increases the amplitude of the trench oscillation, whereas an old slab and/or more viscous lower mantle dampens the undulation of the slab trailing edge into the MTZ, which in turn, drive less oscillations in V_t (Fig. 3.7a-c bottom, g).

The topography (H_{surf}; H_{dyn}), after having reached its minimum at the end of the 2nd phase, remains almost constant for the less viscous lower mantle and the young plate cases, whereas a rise of the H_{dyn} is observed for the more viscous lower mantle (Fig. 3.7f). This high dynamic stands is due to the mantle return flow restricted to the upper mantle (Fig. 3.7c top, f). The topographic profile still keeps its tilted shape (Fig. 3.7a-c top).

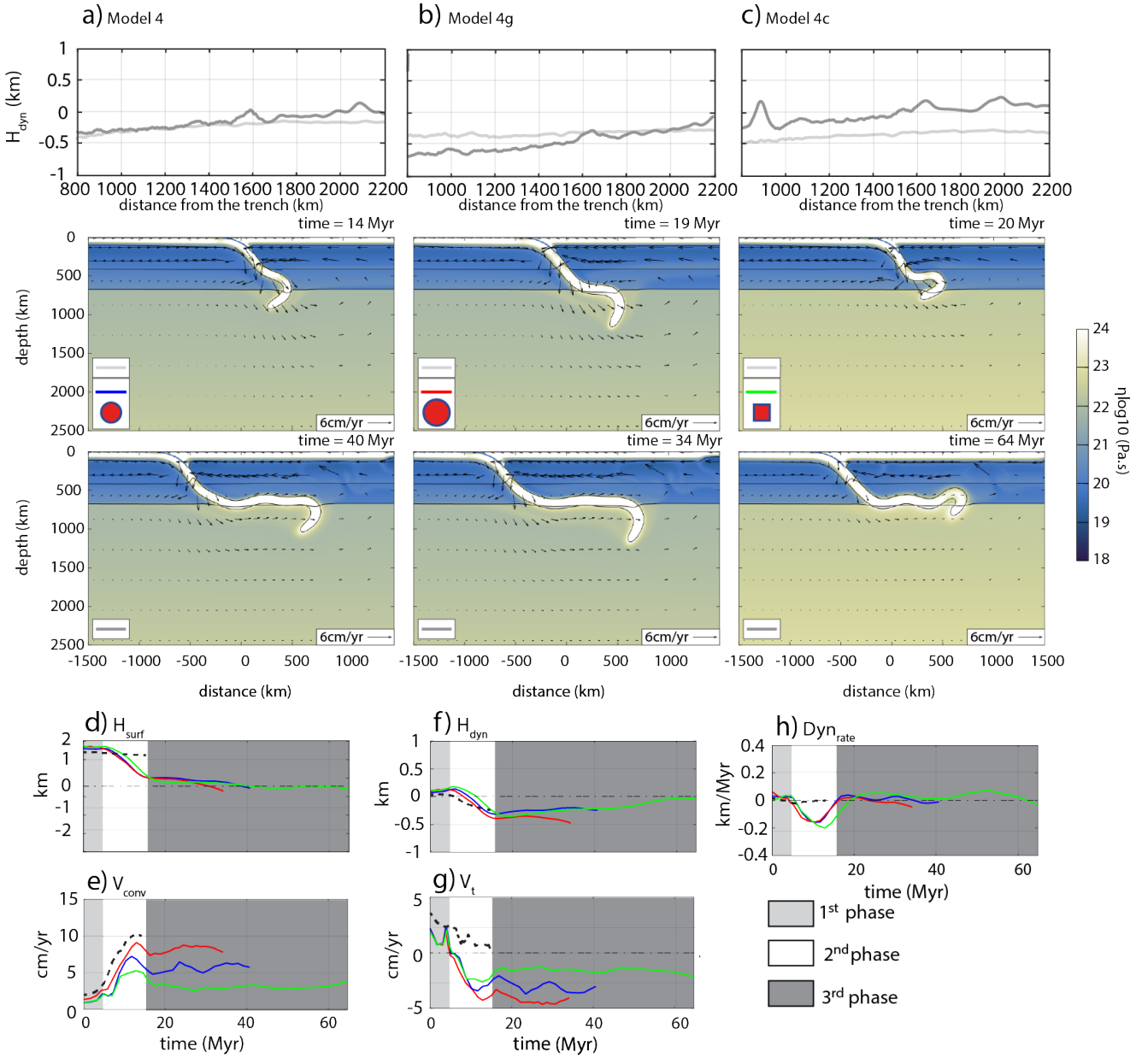

Figure 3.7: (a, b, c) Selected time steps in the evolution of the models 4, 4g and 4a (Table 3.2). Top: zoom in dynamic topography space and time domain. Bottom: zoom into the slab morphology. The colour represents the viscosity and the arrow the velocity field. The black solid line contour is the 1300 °C isotherm. Box in the bottom left corner shows the symbol that refers to the regime diagram in Figure 4.The dark and light grey symbols indicate the dynamic topography profiles for each time steps . Time series of the surface topography (d), convergence velocity (e), dynamic topography (f), trench velocity (g), and the dynamic rate of the upper plate (h) of the current models. Black dashed lines corresponds to the reference model (Fig. 3.3).

3.3.5 Folding slab (category 3)

Category 3 (Fig. 3.8) involves simulations that primarily have a strong ol-wd phase transition, combined with relatively strong post-spinel transition and a high lower mantle viscosity (Table 3.2). Indeed, it is known that a strong ol-wd phase transition (high γ_{410}) increases the sinking velocity of the slab while both strong post-spinel phase transition (very negative γ_{670}) and strong lower mantle hamper slab penetration and may facilitates slab lateral undulation and slab folding behaviour (*Běhounková & Čížková, 2008; Tosi et al., 2015*).

This slab behaviour obtained for a strong ol-wd (γ_{410}) transition combined with a moderate post-spinel (γ_{670}< -2 MPa/K) transition, while the lower mantle viscosity needs a prefactor A_{lower} > 2.29x10^{15} Pa s (Table 3.2). To better understand the evolution of these slab transition zone interactions, we look at models with similar values of ol-wd (γ_{410}= +5 MPa/K) and post-spinel (γ_{670} = - 2 MPa/K) transitions, and we vary the A_{plate} from 100 Myr to 150 Myr and the A_{lower} viscosity prefactor from 2.29x10^{15} Pa s to 6.87x10^{15} Pa s (Table 3.2). Figure 3.8 shows Model 17a, characterised by a A_{plate} of 100 Myr and a A_{lower} of 2.29x10^{15} Pa·s, Model 17f, with a A_{plate} of 150 Myr and the same A_{lower}, and model 17c with A_{plate} of 100 Myr and the A_{lower} of 6.87x10^{15} Pa s (Table 3.2). Regardless of the transition zone and lower mantle proprieties, the behaviour during the 1st phase for models in Category 3 is comparable to the reference model, and again, the dynamic topography shows a flat profile for the three models (Fig. 3.3a-b tops). However, we notice that the magnitude of V_{conv} is up to 15 cm/yr, higher than for the previous categories due to the high strength of ol-wd (γ_{410}) which enhances the slab pull force (Fig. 3.8e).

After reaching the base of the upper mantle, the folding slabs propagate directly into the lower mantle (Fig. 3.8a-c). Indeed, due to the weak resisting forces associated with a relatively weak endothermic phase transition, slabs pass easily across the transition zone (Fig. 3.8a-c). At first view this behaviour looks like the simple undisturbed sinking slab (Category 1). However, due to the strong slab pull force linked to the strength of the ol-wd transition, the slabs folds in the transition zone (Fig. 3.8 a-c bottom). Also, the lower mantle affects the behaviour of the

folding slab. Indeed, the slab does not penetrate easily into the lower mantle, and as a result, narrow folds are generated in the transition zone (Fig. 3.8c bottom). We observe a dynamic tilting of the upper plate towards the trench once slabs retreat. In contrast, if the slab folds and the trench advance, it induces an opposite tilt of the upper plate (Fig. 3.8a-c top).

The convergent and trench velocities show oscillation in time (Fig.3.8e, g). The model with A_{plate}=150 Myr shows a period of about 20 Myr, whereas the younger subducting plate shows a period of about 15 Myr. The period of the model with stronger A_{lower} is about 30 Ma. The amplitudes of V_{conv} and V_t are not affected by A_{plate} and remain higher of about 2 cm than the stronger lower mantle viscosity case (Fig. 3.8c, e and g).

These variations in velocities corresponds to periods of trenches advance and retreat (Fig. 3.8e, g). These oscillations with similar periods are also found in the topographic evolutions, which show highs and lows in H_{surf} and H_{dyn} (Fig. 3.8d, f). These topographic features follow the trench velocity peaks in time with a delay of ~4 Myr for weak A_{lower} and A_{plate} of 100 Myr and 150 Myr (Fig. 3.8a,b f, g), whereas models with strong A_{lower} shows a delay of ~7 Myr (Fig. 3.8c, d, g). During trench advance, the slab bends towards the upper plate (Fig. 3.8b top, a, c bottom), and as a result, topographic uplift occurs, as shown by the peak in dynamic topographic rate Dyn_{rate} (Fig. 3.8h). In contrast, when the trench retreats, H_{surf} and H_{dyn} decreases, resulting in a minimal Dyn_{rate} (Fig. 3.8h). The amplitude of dynamic topography H_{dyn} varies as function of A_{plate}, where a younger subducting plate induces more topographic amplitude about of 0.2 km (Fig. 3.8f). The amplitude of H_{dyn} for stronger lower mantle viscosity (Fig. 3.8c, f) remains the similar to what is measured for the models with weaker lower mantle viscosity (Fig. 3.8a, f).

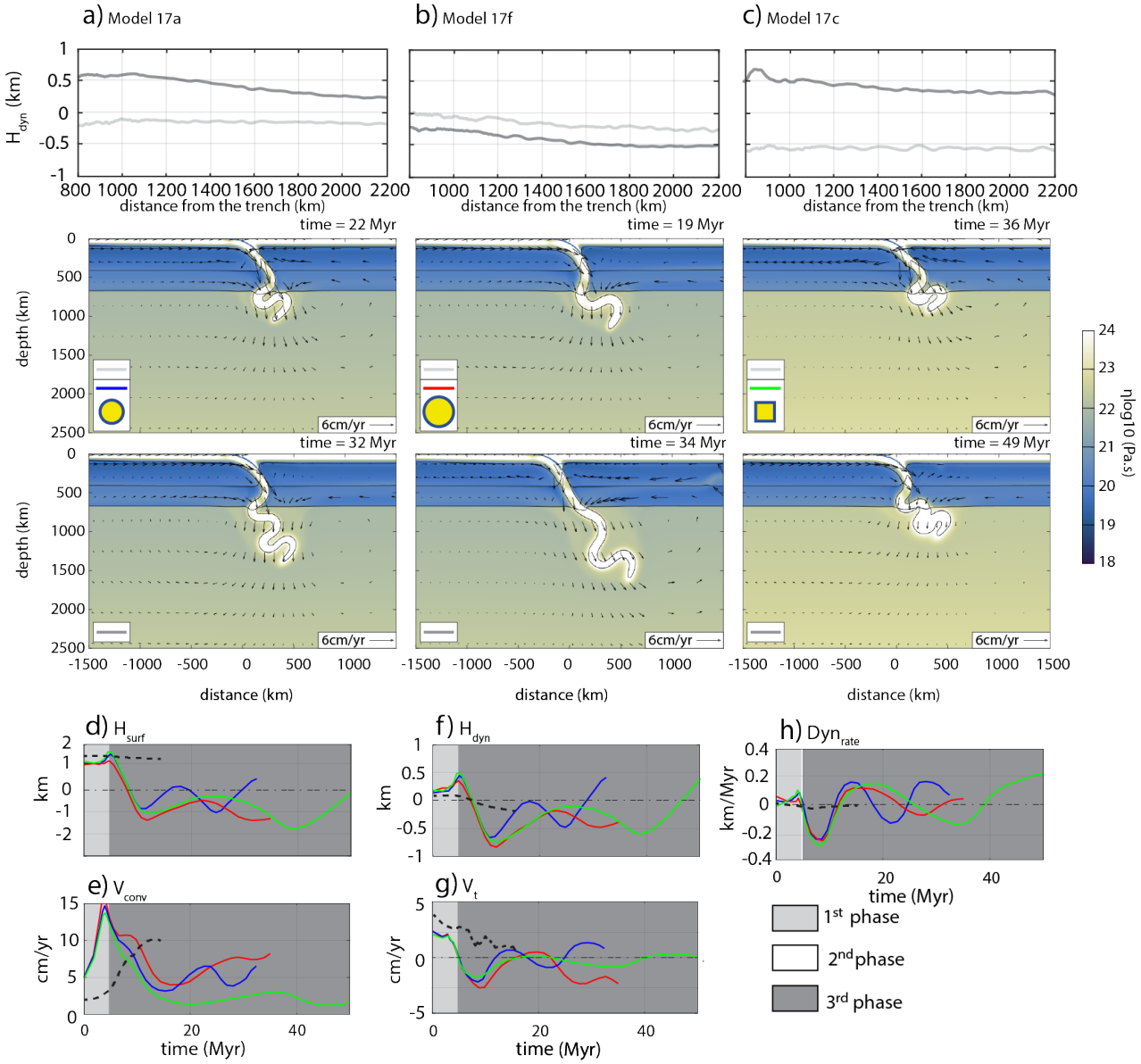

Figure 3.8 : (a, b, c) Selected time steps in the evolution of the models 17a, 17f and 17c (Table 3.2). Top: zoom in dynamic topography space and time domain. Bottom: zoom into the slab morphology. The colour represents the viscosity and the arrow the velocity field. The black solid line contour is the 1300 °C isotherm. Box in the bottom left corner shows the symbol that refers to the regime diagram in Figure 4.The dark and light grey symbols indicate the dynamic topography profiles for each time steps. Time series of the surface topography (d), convergence velocity (e), dynamic topography (f), trench velocity (g), and the dynamic rate of the upper plate (h) of the current models. Black dashed lines corresponds to the reference model (Fig. 3.3).

3.3.6 Buckling slab and avalanche (Category 4)

Category 4 differs from the Category 3 by showing a long period of slab folding in the MTZ, followed by a slab avalanche behaviour into the lower mantle. This is obtained with a strong γ_{670} (Table 3.2). To study the evolution of this slab category, we use a model similar to the one used in Category 3, but with γ_{670}=-3MPa/K (Fig. 3.9a-c).

As before, we modify the lower mantle viscosity and the A_{plate}. Model 19b has a A_{plate} of 100 Myr and an A_{lower} value of $2.29x10^{15}$Pa s, whereas model 19b has an older A_{plate} of about value 150 Myr. For model 19c, we increase the A_{lower} at $6.87x10^{15}$Pa s while we keep the same A_{plate} as in model 19b (Table 3.2).

For the 2nd phase, the creation of folds is mirrored by fluctuations of V_{conv} and V_t (Fig. 3.9e, g). When V_{conv} increases, the slab rolls back and the trench retreats. By contrast, when V_{conv} decreases, the slab bends towards the upper plate, and the trench advances (Fig. 3.9 a-c, e, g). The amplitude and period of velocities are similar to those recorded in the Category 3. The periods are about 30 Ma and 15 Ma for the models with a stronger and weaker lower mantle viscosity, respectively (Fig. 3.9.e, g). The amplitudes in V_t are not affected by A_{plate} and remain higher of by about 1 cm/yr than the stronger lower mantle viscosity case (Fig. 3.9c, e, g). Indeed, strong A_{lower} decreases the velocities, because strong A_{lower} decrease the vigour of the convection. Following the V_t oscillation in time, the dynamic topography profiles are similar to those for Category 3, episodically experiencing a dynamic tilting of the upper plate towards and away from the trench with respect to the slab folding dynamics and trench movement.

The mean topographic measurements (H_{surf} and H_{dyn}) increase and decrease depending on the slab folding in the transition zone (Fig. 3.9a-c, f). The H_{dyn} amplitudes and periods are also similar to what was recorded in the Category 3, with the difference that in these cases the slabs pile up in the transition zone rather than in the lower mantle.

When the slab material that accumulates into the transition zone starts to flush down into the lower mantle (3th phase) (Fig. 3.9a-c bottom), the dynamic topographic profiles show a sudden high, followed by an abrupt dynamic subsidence of the upper plate (Fig. 3.9a-c top). We observe a sharp increase in V_t and V_{conv} for the models with weak A_{lower} (Fig. 3.9a-c,e, g). On the contrary, model with strong A_{lower} prevent the slab from penetrating into the lower mantle, and induce a slow increase in V_t (Fig. 3.9c, g). For models 19b and 19g, V_t and V_{conv} increase with up to 5 cm and ~10 cm, respectively (Fig. 3.9a-b, e, g). Such-acceleration is explained by an increase of the slab sinking force, due to the reduced effect of the post-spinel (γ_{670}) resisting force after the slab penetration. In contrast, model 19c shows smaller amplitude

in V_t and V_{conv} about 1 cm/yr and 3 cm/yr, respectively (Fig. 3.9c, e, g). Strong lower mantle viscosity hampers the slab sinking into the lower mantle, which, in turn, drives slow trench retreat (Fig. 3.9c, g). The velocities (V_{conv} and V_t) show oscillation periods of about 30 Ma and 50 Ma for models with weak A_{lower} and strong A_{lower}, respectively (Fig. 3.9e, g). Linked to these new kinematics (Fig. 3.9d, f, h), H_{surf}, H_{dyn}, and Dyn_{rate} (Fig. 3.9d, f, h) show long period of increasing and decreasing induced by the slabs avalanches where, the periods are similar to what is recorded in V_t and V_{conv} (Fig. 3.9a-c, f). The amplitudes differs according to the geodynamical variables (A_{lower}, A_{plate}). Varying A_{plate} does not change the amplitude of H_{dyn}, which remains about 1.1 km. In contrast, stronger lower mantle viscosity increases the H_{dyn} amplitude by about 0.6 km more than weaker lower mantle (Fig. 3.9f).

After a 'slabs avalanche', trench retreats and we observe a tilting of dynamic topography profile toward the trench (Fig. 3.9a-c). This typical dynamic topography profiles resemble those for the flat slab behaviour (Category 2). However, there are variation between modes (Fig. 3.9a-c). The steepest tilt is recorded for the weak A_{lower} in combination with A_{plate}=100 Myr (Fig. 3.9a), whereas neither old plates, nor a viscous lower mantle do not provide steep tilting of the upper plate (Fig. 3.9b-c).

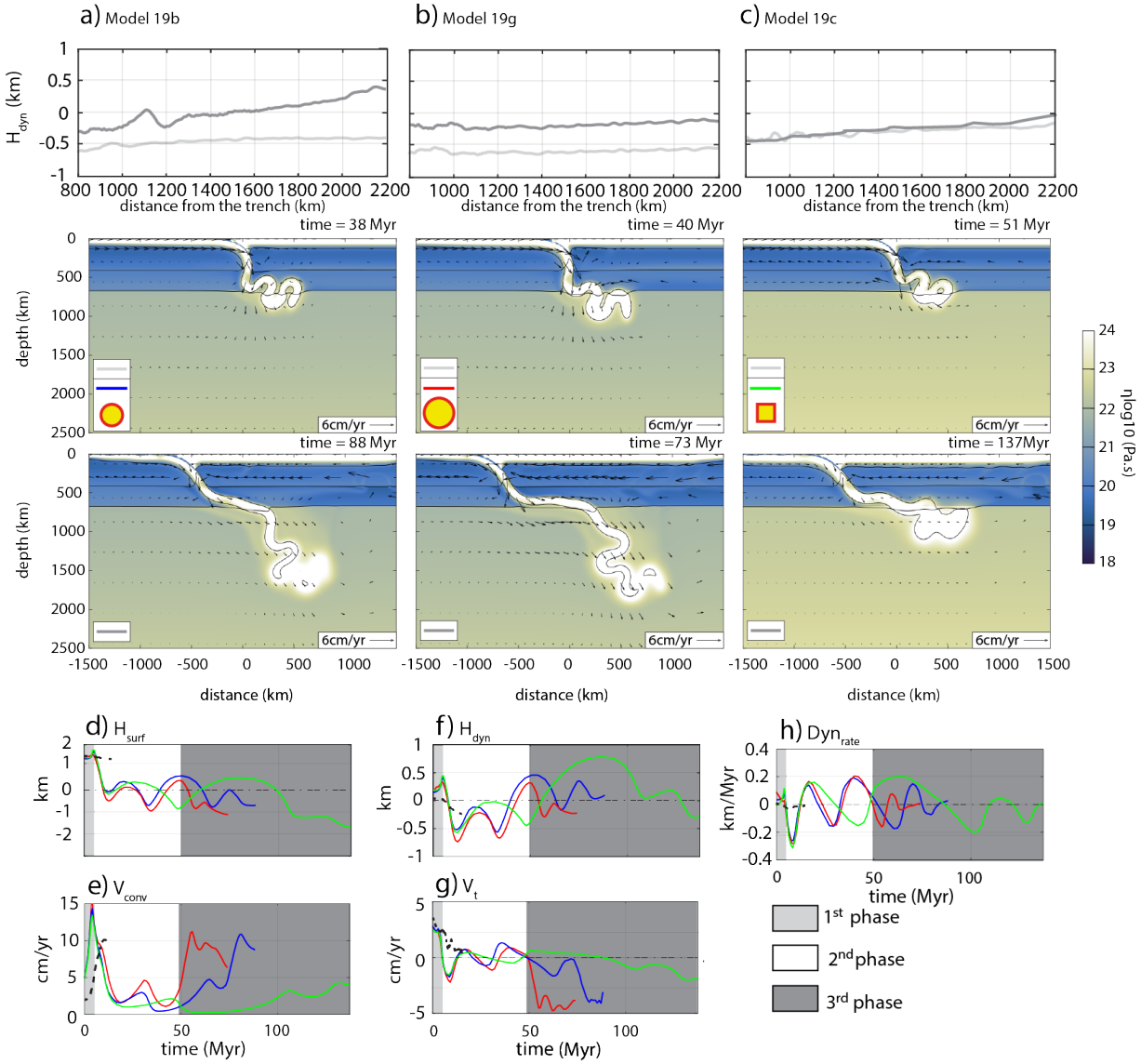

Figure 3.9 : (a, b, c) Selected time steps in the evolution of the models 19b, 19g and 19c (Table 3.2). Top: zoom in dynamic topography space and time domain. Bottom: zoom into the slab morphology. The colour represents the viscosity and the arrow the velocity field. The black solid line contour is the 1300 °C isotherm. Box in the bottom left corner shows the symbol that refers to the regime diagram in Figure 4.The dark and light grey symbols indicate the dynamic topography profiles for each time steps. Time series of the surface topography (d), convergence velocity (e), dynamic topography (f), trench velocity (g), and the dynamic rate of the upper plate (h) of the current models. Black dashed lines corresponds to the reference model (Fig.3.3).

3.3.7 Sensitivity of the dynamic topography with respect to deep slabs dynamics

To summarize the findings of our parametric study, Figure 10a, c show the relationships between the time needed by slabs to fold (i.e., t_{fold}) versus the mean dynamic topography period and the maximum dynamic topographic rate, whereas the maximum thickness of the slab into the transition zone against the maximal dynamic topography amplitude is shown in Figure 10b. The dynamic topographic period is measured by taking the duration between peaks and averaging these distance. For the amplitudes of the dynamic topography (H_{dyn}) and its rate (Dyn_{rate}), we take their maximum values in time after the first slab/MTZ interactions (i.e., t_{670}) (e.g., Fig. 3.9f).

The dynamic topographic period depends on the ability of the slab to sink into the lower mantle. For the weakest lower mantle viscosity, slabs sink faster into the lower mantle than they do for a more viscous lower mantle case. We observe a relationship between the time spent by the slab in the MTZ (t_{fold}) and the dynamic topographic period. Stronger lower mantle viscosity results in the slab being trapped into the MTZ, which, in turn, increases the dynamic period. In other words, this specific surface fingerprint highlights the fact that the mantle flow is slower for strong mantle viscosity, which in turn, drives a longer dynamic period. On the contrary, the weakest lower mantle viscosity provides less resisting force to slab-mantle induced flow. The mantle vigour is therefore more efficient, providing a shorter period in dynamic topography (Category1, Fig. 3.10a).

A viscous lower mantle combined with a strong ol-wd transition (i.e., $\gamma_{410} > +3.5$ MPa/K) and a relatively weak post-spinel transition (i.e., $\gamma_{670} > -3.0$ MPa/K) reduces the dynamic period. The age of the subducting plate does not induce significant changes in the period for Category 1, 3 and 4, whereas an old plate decreases the period for Category 2.

For the dynamic amplitude and its rate, we observe a linear trend between Category 1, 3 and 4 (Figure 8b-c). Again, the amplitude increase depends on the viscosity of the lower mantle. A stronger lower mantle together with a large strength of the ol-wd transition (i.e., $\gamma_{410} > +3.5$ MPa/K) and a weak post-spinel one (i.e., $\gamma_{670} < -3.0$ MPa/K) leads to the highest amplitudes in dynamic topography and its rate (Figure 10b-c). The slabs from Category 2 stand-out from the

relationship between the maximal width of the slab (W_{670}) and the dynamic amplitude. These models have similar dynamic topography amplitudes, around 900 m (Figure 10b).

The dynamic topographic rate (Dyn_{rate}) amplitudes are less than ~0.25 km/Myr for both Category 1 and 2. This indicates that neither undisturbed slab (Category 1) nor flat slab (Category 2) behaviour in the MTZ influence the large-scale topography of the upper plate significantly (Figure 8c). On the contrary, Category 3 and Category 4 show a wide range of dynamic topography rates from ~0.15 to ~0.5 km/Myr. Those values indicate that the folding slab behaviour strongly affects the topography of the upper plate. The strong resisting force to slab penetration linked to A_{lower} and γ_{670} drives the highest Dyn_{rate} amplitude.

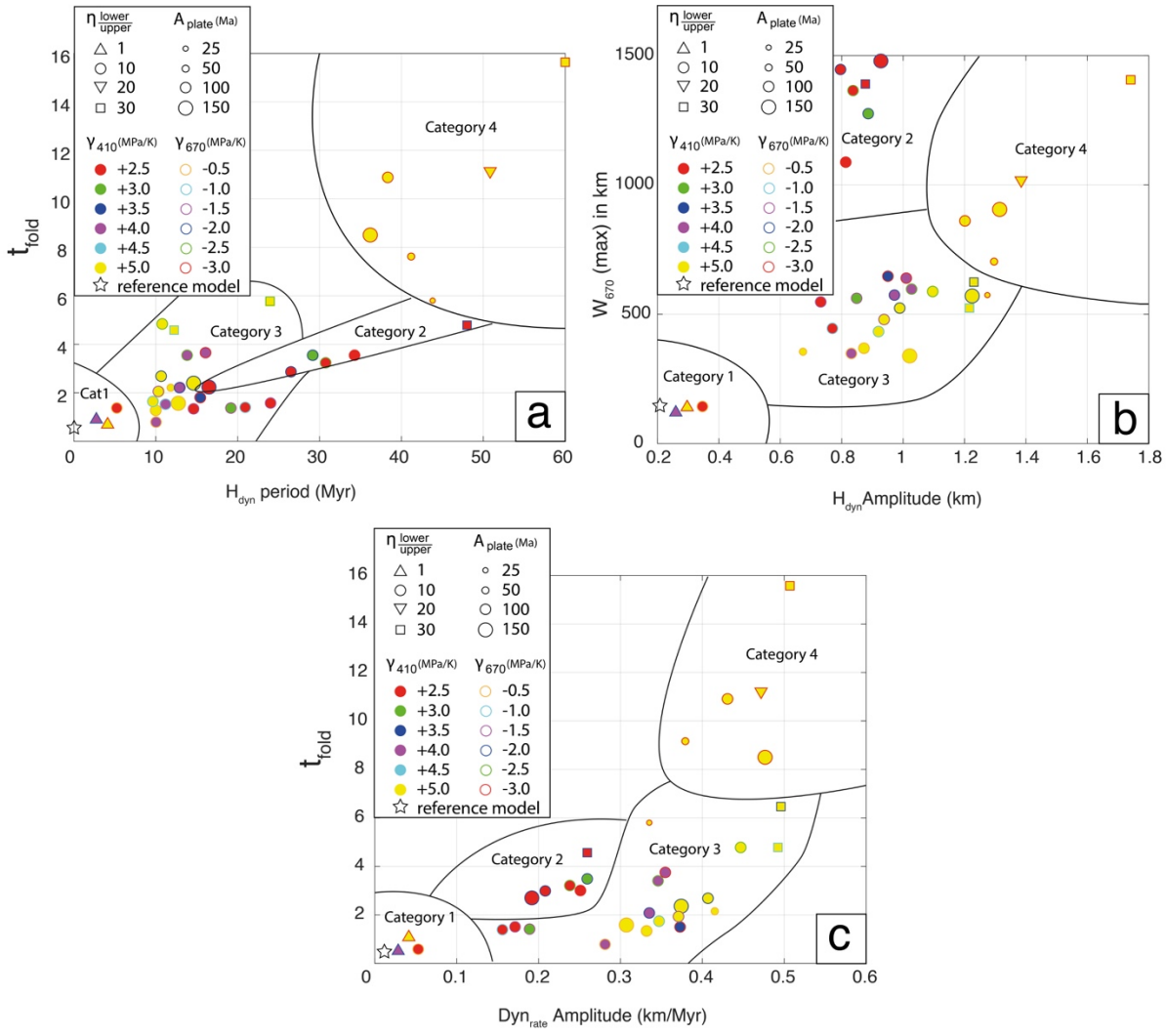

Figure 3.10 : (a) Diagram plotting t_{fold} against the mean dynamic topographic period (H_{dyn}). (b) Diagram plotting the slab thickness in the MTZ ($W_{slab}(max)/W_{slab}(t=0)$) versus the dynamic topography amplitude (H_{dyn}). (c) Diagram plotting t_{fold} over the maximum dynamic topography rate (Dyn_{rate}). How indicate in the legend box: The shape of the symbols represents the lower mantle viscosity. The size of the symbols represents the initial subducting plate age (A_{plate}). The colour of the symbols represents the strength of ol-wd transition (γ_{410}). The colour of the edges of the symbols represents the strength of post-spinel

transition (γ_{670}). Black lines delineate the slab categories areas: straight slab (category 1), flat slab (category 2), folding slab (category 3) and folding slab and avalanche (category 4).

3.4 Discussion

This study presents 2D self-consistent numerical models showing how the evolution of the slab during its journey into the mantle is represented by the dynamic topography of the overriding plate. The characteristic dynamic topographic signal strongly depends on the slab dynamics at depth. We find that, for each of the categories presented in the section 3.3, the slabs behave differently, leading to a different, diagnostic surface expression.

In the category 1 (Fig. 3.6) the weak resistance to slab penetration enables vertical slab sinking into the lower mantle. This behaviour generates a large-scale return flow producing efficient slab suction (*Faccenna et al., 2013*). Therefore, the trench does not retreat, but instead shows a slight advancing motion. The dynamic topography slightly decreases over time when the slab sinks below the upper lower mantle discontinuity. Indeed, undisturbed sinking slabs into the lower mantle lead to the creation of a much larger convection cell below the upper plate. As a result, the dynamic topography of the upper plate is progressively pulled down by the downward mantle flow generated by the sinking slab at depth.

For category 2 slabs (Fig. 3.7), once the slab reaches the 670 km discontinuity, a 'slab pull' type dynamics (*Faccenna et al., 2013*) is observed. At the surface the dynamic topography is dragged down and a tilt towards the trench is observed when the slab starts to interact with the upper/lower mantle discontinuity. Both the dynamic topographic low and the topographic tilt remain stationary during slab flattening in the MTZ, due to the steady trench retreat state.

For category 3 (Fig. 3.8), episodic fold formation at depth occurs when the slab interacts with the transition zone. This behaviour is recurrent in all our models with a strong γ_{410} and γ_{670}, combined with a viscous lower mantle. On the one hand, once the slab folds towards the upper plate, the trench advances, and uplift occurs on the upper plate. On the other hand, the backward bend of the slab driven by trench retreat enhances an upper plate dynamic low. Episodic dynamic topographic highs and lows, as well as tilting towards and away from the trench, are promoted by slab folding.

Category 4 is characterized by a first phase, in which the slab deforms into the MTZ and shows a topographic evolution at the surface similar to the folding slab (Category 3). The trench advance and retreat motion precedes the dynamic topographic variation in time. Yet, the dynamic tilting of the upper plate towards and away from the trench depends on the slab folding behaviour into the MTZ. Later, the slab sinks into the lower mantle (avalanche) and we observe

an abrupt increase in trench velocity followed by an abrupt dynamic low, and a tilt of the upper plate toward the trench. This surface fingerprint is similar to that observed for the flat slab (Category 2). Hence, the slab surface expression for Category 4 is a combination between the folding and flat slab cases (Categories 3 and 2, respectively).

In agreement with *Crameri & Lithgow-Bertelloni,* (2017), we found that once the slab tip reaches the 670 km discontinuity, the mantle convection cell become much larger, leading to a tilt of the overriding plate. Under this condition the dynamic topography of the overriding plate is dragged down abruptly. When the slab is ponding into the MTZ, the dynamic topography remains low, indicating that the underlying mantle flow keeps on being dragged down from underneath the upper plate. Moreover, we see that a folding-slab behaviour leads to episodic changes in the slab morphology. Slabs may fold forward and backward, leading to episodic trench advance and retreat motions. Hence, the trench kinematics tunes the ability of the dynamic topography to go up and down. This finding agrees with (*Cerpa et al., 2015*), who show that slab dips vary in a time-dependent manner as soon as they encounter a strong barrier as the 670 km discontinuity, inducing episodic changing in the trench velocity, and, in turn, building up topographic highs and lows close to the trench.

Our results show a key role for of slab dynamics in controlling trench motion and the dynamic topography of the upper plate. However, previous studies have shown that trench motions may depend on 3-D flow in the mantle (*Funiciello et al., 2003; 2006*; *Schellart et al., 2007*). In our study the main controlling factors on the surface fingerprint are the lower mantle viscosity and the slab buoyancy once it reaches the 670 km depth discontinuity, and our results can be thus considered valid in 3-D settings if our 2D models are set at the centre of a wide 3-D slab. By contrast, narrower 3-D models should increase the trench velocity and thus might change the dynamics of the slab at depth. Nonetheless, the dynamic topography should remain the same for a given set of slab category (direct sinking, flat slab, folding slab). Further work is necessary to test this idea.

It has been known that the upper mantle deforms by dislocation creep (e.g., Hirth *& Kohlstedt, 2003; Karato & Wu, 1993)*. Dislocation creep may lead to a lower viscosity into the asthenosphere, compared to the presented models, inducing a better decoupling between the plates and the mantle which would be less favourable to trench retreat (e.g., *Billen & Arredondo, 2018; Capitanio et al., 2007*). Additionally, in case of an upper mantle with a larger viscosity (>2.10^{20} Pa s) a delay in fold formation at depth might be expected. Indeed, the size of the fold as well as the spacing between two successive folds may increase. Also, it would have an effect on the slab sinking velocity which may delay the timing of a fold formation into

the upper mantle (e.g., *Billen & Hirth, 2007; Čížková et al., 2007*). Hence, the oscillation in the trench advance and retreat migration might be reduced. Similarly, an increase of viscosity of the upper mantle may be comparable to an increase in the strength and buoyancy of the subducting plate. Indeed, as we show for the oldest slab cases (sections 3.3.5-3.3.3.6), the amplitude of the folds and the timing between two folds increase, while the trench velocity is reduced for youngest initial age (A_{plate}) of the subducting plate. Most importantly, an increases of upper mantle viscosity or the strength and buoyancy of the subducting plate delay the spacing between two uplifts episodes as well as reduce the magnitude of the uplift of the upper plate. Hence, by changing those model characteristics (third dimension, upper mantle rheology, composite rheology, weak layer viscosity), the presented category boundaries in Figure 3.5 would likely shift as consequence, but the characteristic surface fingerprints should remain similar for the corresponding slab category (i.e., flat, straight, buckling slabs). There is observational evidence for of time-dependent variation surface fingerprints which may be linked to deep slab dynamics in the mantle MTZ.

The surface expression of deep mantle dynamics has been explored and analysed at global and local scale. At the global scale the present day signal of deep subduction is well registered both in the geoid and topography (*Flament et al., 2013; Forte et al., 1993; Zhong et al., 1996*), even if the fit between residual topography and dynamic topography is still low (*Steinberger et al., 2001*). Marine large-scale inundation has been interpreted as a signal of large-scale continental tilting due to deep subduction. Other examples come from continental subsidence of the Russian platform during the Devonian to Permian (*Mitrovica et al., 1996*) and the subsidence of the Karoo Basin during the Late Carboniferous to Early Triassic (*Pysklywec & Mitrovica, 1999*), both attributed to the subduction evolution and slab penetration into the lower mantle, leading to the subsidence of basins. In addition, the subsidence of the Australian plate might be attributed by a significant amount of slab material localized within the mantle MTZ (*DiCaprio et al., 2009; Heine et al., 2010*) which pulls down the continental plate.

Another test site for deep subduction is represented by the penetration of the Farallon slab under North America into the lower mantle probably in the Late Cretaceous. The deep slab penetration has been suggested to generate subsidence of several hundreds of meters producing large scale flooding (*Gurnis, 1990; Gurnis et al., 2000; Liu et al., 2008; Mitrovica et al., 1996*). Subsidence rates have been calibrated with the lower mantle viscosity providing a picture similar to what has been found in our numerical model results.

The dynamic topography related to slab folding has not yet been described in nature. Deciphering alternating episodes of subsidence and uplift in the geological record is indeed

more complicated. Our model shows that the period of the expected signal is on the order of tens of million years but also that the vertical motion is accompanied by horizontal advance motion of the trench, as both will be dictated also by the oscillation of the trench motion. We expect alternatively extensional or neutral tectonics regime and compression related to subsidence and uplift, respectively. One possible example is the compressional tectonic episodes and the variation of the arc volcanism as recognized in the Andes that has been commonly attributed to variations of the slab dip angle (*Folguera et al., 2006; Kay et al., 2005*). This work will provide new insights to explain other alternating compressional/extensional patterns of deformation over mobile belts.

3.5 Conclusions

In this study, using a series of 2D single-sided self-consistent thermo-mechanical subduction models, we investigate how the slab dynamics at depth may affect the surface topography of the upper plate. A systematic study shows that within a plausible range of the olivine phase transitions, mantle viscosity contrasts and ages of subducting plates, there are many cases where the surface topography is strongly affected by the underlying slab dynamics. Cases where slabs sink straight into the deep mantle, which display a vertical morphology, induce at the surface a quasi-stationary trench state as well as a relative flat long-wavelength topographic signal of the upper plate over time. The coexistence of a strong post-spinel transition (<-2 MPa/K) Clapeyron slope combined with a viscous lower mantle ($\geq 1.2 \times 10^{22}$ Pa s) hampers, at least temporarily, slab penetration into the lower mantle and induces slabs to lay down horizontally in the MTZ, thereby driving trench retreat. As a result, a wide convection cell beneath the upper plate induces a dynamic low of the entire upper plate. Slab folding and buckling are typical for both strong Clapeyron slopes at 410 km depth and 670 km depth, and are characterized by episodes of trenches retreat and advance motion. These specific kinematics lead to cyclic changes of the mantle flow below the upper plate, and induce episodic variation of dynamic topography, by pulling up and down the upper plate according to the slab folding a depth. Changes in slab dynamics occur regularly throughout Earth history. The associated changes of the surface topography will help us constrain such deep slab behaviour through time.

Chapter IV

Deep Slab folding and the deformation of the Iranian mobile belt

(central Tethys system)

Abstract

To Unravel the Neotethys slab morphology evolution at depth since mid-Cretaceous, we produced a synthesis of the main events affecting the western Cimmerian domain. This synthesis is focused on the upper and lower plates (i.e. the western Cimmerian domain and the Neotethys ocean, respectively) of the system based on the compilation of structural, geochemical and geochronological data available on the area. We explore the structural evolution of the western Cimmerian domain and we reconstruct the evolution Neotethys subduction system in both maps and cross-sections. We interpreted this evolution as consequence of deep slab dynamics and trench motion. We propose a 2D single-sided numerical model to better understand the interactions between the deep and surface processes. It suggests that the upper plate episodic deformation events are driven by the folding slab behavior at depth. We combine our data and numerical model into a conceptual scenario to overcome the complexity of the kinematics of the Neotethys slab since Early Cretaceous. Our results show that the back-arcs opening and the extension episodes into the upper plate are driven by the roll-back of the folded slab into the mantle transition zone. In contrast, the back-arc closures and upper plate shortening are triggered by the roll-over of the folding slab. Eventually a large-scale marine flooding event of the upper plate is linked to the Neotethys slab avalanche during Early Miocene.

4.1 Introduction

Deformation of back-arc extension is ephemeral, lasting only 10-30Myrs *(Taylor & Karner, 1983*). Pulses of extension and shortening has been documented on Pacific and Mediterranean back-arc basins (*Taylor & Karner, 1983*) and in some orogenic belts such as the Andes (e.g., *Guillaume et al., 2010; Martinod et al., 2013*) or the Iranian mobile belt. The deformation of this last area is related to the subduction of the Neotethys ocean (*Barrier & Vrielynck, 2008; Golonka, 2004; Stampfli & Borel, 2002*) below the western Cimmerian block, which is now attached to the Eurasian plate (Fig. 4.1; e.g., *Sengör et al., 1984; Stampfli & Borel, 2002*). The western Cimmerian domain constituted the main portion of the Iranian mobile belt deformed by episodes of compression and extension leading to the formation of two main back-arc domains, the Nain-Baft and the Sabzevar-Sistan, separated by the central Iran block (i.e., Yadz-Tabas and Lut micro blocks; Fig. 4.1).

We use geological reconstruction and numerical modelling to investigate the cause of the short-lived episodes of deformation. Previous studies suggested that episode of slab break-off may explain extension and the volcanic flare up around 40 Ma (e.g., *Agard et al., 2011; Verdel et al., 2011*). However, on convergent setting slab break-off should result in a decrease in slab pull force and then and producing trench advance; upper plate shortening and collision. Yet these interpretations cannot explain in any way the repetition of deformation episodes.

Here we propose a new model where the pulse of extension and compressional deformations are related to the trench oscillations in time following the slab deformation into the mantle transition zone, between 410km and 670km. We use the tectonic reconstructions to model the position of the trench and to estimate the velocity of convergence in time. We test this idea using simple numerical model showing how the time dependence of the upper plate deformation depends on: (1) viscosity coupling between slab and mantle and (2) on the presence of two major olivine phase transition at 410 and 670km depth respectively. The resulting model is further compared with tomography images which suggest that pile of slab is localized around 1500km depth (*Fukao & Obayashi, 2013; Ritsema et al., 2004; Simmons et al., 2010*).

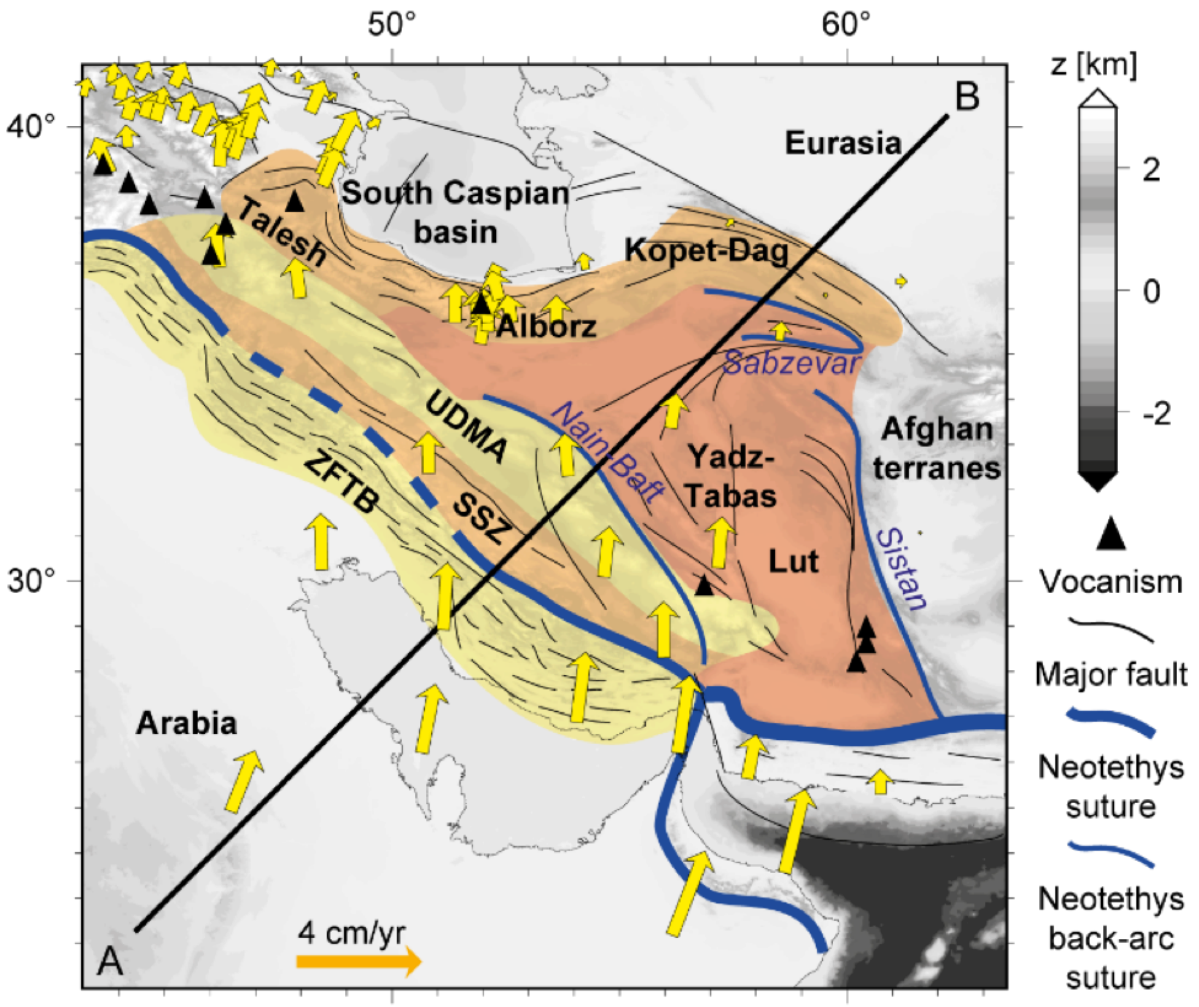

Figure 4.1: Main structural areas of the western Cimmerian domain (coloured areas) and main Neotethys suture and associated back-arcs in the studied area. Thick black line represents the path of the present-day section in Fig. 4.4 and Fig. 4.9 (ZFTB: Zagros Fold and Thrust Belt; UDMA: Urumieh-Dokthar Magmatic Arc; SSZ: Sanandaj-Sirjan Zone.

4.2 Geological background

The Iran mobile belt can be divided on six tectonic domains, characterized by different deformation episode (as summarized on Figure 4.2) and described in the following paragraph.

Neotethys domain. The Neotethys oceanic spreading is active at least during middle Cretaceous times (~120 to ~73Ma; Fig. 4.2; *Shafaii Moghadam & Stern,* (*2015*) and reference therein), followed by another short spreading episode (Fig. 4.2; 42 to 37 Ma; *Shafaii Moghadam & Stern, 2015*), identified only in the northern part of the Sanandaj-Sirjan zone (Fig. 4.1), close to the Iran-Iraq boundary (*Shafaii Moghadam & Stern, 2015*). Collision started in the Early Oligocene times (Fig. 4.2; e.g., *Agard et al., 2011; McQuarrie & van Hinsbergen, 2013*).

The Sanandaj-Sirjan zone. The Sanandaj-Sirjan is a 50 to 100km wide domain, limited by the Neotethys suture in the SW and by the Urumieh-Dokhtar magmatic arc in the NE. It extends from the Bitlis to the western end of Makran (Fig. 4.1). It is constituted by Mesozoic metamorphic and igneous rocks showing tholeiitic and calc-alkaline signatures (e.g., *Ao et al., 2016; Leterrier, 1985; Omrani, 2018*) and commonly interpreted as the active margin of the western Cimmerian domain (Fig. 4.2; e.g., *Agard et al., 2011; Stocklin & Nabavi, 1973*). Starting Oligocene until Miocene, due to the Arabia-Eurasia collision, the Sanandaj-Sirjan zone was shortened exhumed and overthrusted above the Arabian plate (*Agard et al., 2005; François et al., 2014*). Shortening is followed by the formation of large strike-slip zone related to the partitioning and lateral escape of block from the Arabia collisional zone (e.g., *Allen, 2010; Authemayou et al., 2006*). At present day, the Sanandaj-Sirjan domain show a thick crustal root (i.e., the Zagros orogen about 55 to 70 km depth; e.g., *Paul et al., 2006*) and represent the backbones of the Iranian Plateau. It encompasses a series of mostly internally drained sedimentary basins with low internal topographic relief bounded by the High Zagros Mountains and the Urumieh-Dokhtar magmatic arc to the SW and NE, respectively (*Ballato et al., 2017*).

Urumieh Dokhtar magmatic arc. The Urumieh-Dokthar magmatic arc is situated in between the Central Iranian domain and the Sanandaj-Sirjan zone, partly covering the Nain-Baft ophiolitic belt (Fig. 4.1). It is constituted mainly by subduction related tholeiitic and calc-alkaline volcanic deposits of Eocene to Oligocene age (e.g., *Dimitrijevic, 1973; Omrani et al., 2008*). Since Miocene, the Urumieh-Dokhtar arc activity is restricted to small adakites

provinces (e.g., *Agard et al., 2011; François et al., 2014; J. Omrani et al., 2008; Verdel et al., 2011*).

The Nain-Baft oceanic basin (back-arc). The Nain-Baft belt consists of a series of ophiolitic slices cropping out along the Nain-Deshir and Deshir-Baft thrusted toward the SW above the Sanandaj-Sirjan zone. Tectonic slices are composed of serpentinized ultra-mafic and mafic rocks with MORB signatures (*Pirnia et al., 2018*) along with radiolarites and limestones of Late Cretaceous (Fig. 4.2; e.g., *Ghazi et al., 2012; Pirnia et al., 2013*). They formed during the Late Cretaceous episode of back-arc spreading (Fig. 4.2; e.g., *Shafaii Moghadam et al., 2009*). Middle Paleocene limestone rest unconformably over the tectonic slices, indicating the closure of the oceanic basin (Fig. 4.2). The Nain-Baft belt bounds to the SW boundary the Central Iran domain (Fig. 4.1).

Central Iran domain. The Central Iranian domain is constituted by several crustal blocks, including the Central Iran, the Yadz-Tabas blocks and the Lut block (Fig. 4.1; e.g., *Berberian & King, 1981*). These formed during the opening of the Neotethys and the separation of the western Cimmerian domain from the Gondwanan plate during Permian to Early Triassic times (e.g., *Barrier & Vrielynck, 2008; Stampfli & Borel, 2002*). Both the Lut and the Yadz-Tabas blocks of in Central Iran recorded several rotations trough time during Mesozoic and since the onset of the Arabia-Eurasia plates collision (Fig. 4.2; e.g., *Mattei et al., 2015, 2017*). Moreover, a 100 km long belt of metamorphic core complexes is present in between the Yazd and Tabas blocks indicating Paleogene extension (Fig. 4.2; e.g., *Verdel et al., 2007*).
In addition, in the western Iranian domain, (i.e., in Central Iran, Sanandaj-Sirjan zone and Urumieh Dokthar magmatic arc), the deposition of the Qom formation dated from the Early to Middle Miocene shows shallow marine deposits (Fig. 4.2; e.g., *Aghanabati & Rezai, 2009; Saidi et al., 1997; Stoneley, 2015*). This is suggesting a post-collisional subsidence of the whole western Cimmerian domain.

Sabzevar-Sistan oceanic basin (back-arc). The Sabzevar-Sistan suture zone from a thousand kilometre-long ophiolitic system separates the Central Iran domain from the Eurasian plate and the Afghan micro-blocks. We can define two main regions. The northern one, the Sabzevar suture zone (Fig. 4.1), extends EW over 400 km in NE Iran. It is bounded by the Kopet Dagh at North and by the Lut micro-block. The southern one, the Sistan suture, extends roughly NS over 1000 km bordering to the West the Lut block and the Afghan block to the East (Fig. 4.1).

Large-scale still active strike-slip faults bordering the two sutures areas attest to late deformation of the different micro-blocks during the Arabian-Eurasia collision (e.g., *Blanc et al., 2003; Calzolari et al., 2016*). In the Sistan area, ophiolites attest the presence of an Early Cretaceous ocean showing MORB and Supra-subduction zone magmatic signatures (Fig. 4.2; *Babazadeh & de Wever, 2004; Saccani et al., 2010; Zarrinkoub et al., 2012*). In the Sabzevar area, Early Cretaceous extension preceded the opening of the Sabzevar ocean at around 105 Ma (*Rossetti et al., 2014*). Thus, both Sabzevar and Sistan structural zones represent an early phase of back-arc extension *(Rossetti et al., 2010; Shafaii Moghadam et al., 2016*), but their original position and continuity are debated (e.g., *Bagheri & Stampfli, 2008; Barrier & Vrielynck, 2008*). Figure 4.2 shows a possible Sabzevar-Sistan single and connected oceanic domains (e.g., *Barrier & Vrielynck, 2008*).

The opening of the Sabzevar-Sistan Neotethyan back-arc is synchronous to the anti-clock wise rotation of the Central Iran domain (*Mattei et al., 2015*). The Sabzevar-Sistan ocean closed progressively starting Late Cretaceous to early Tertiary (e.g., *Barrier & Vrielynck, 2008; Zarrinkoub et al., 2012*). Magmatic and structural argument support eastward subduction of the Sabzevar-Sistan ocean under the Eurasian plate and the Afghan block, respectively. During the late collision, the central Iran domain rotated and the Sabzevar-Sistan suture was possibly off-set by large dextral strike-slip fault system. Magmatic signature in the Sabzevar-Sistan area are high potassic calc-alkaline to calc-alkaline domain and also showing adakite signatures since Eocene times interpreted as the Eocene episode of slab break-off (Fig. 4.2; *Jamshidi et al., 2015; Rossetti et al., 2014; Shabanian et al., 2012*). In addition, nummulitic limestone deposits have been observed in the Central Iran and Sistan area suggesting subsidence of this area (e.g., *Aghanabati & Rezai, 2009; Saidi et al., 1997*).

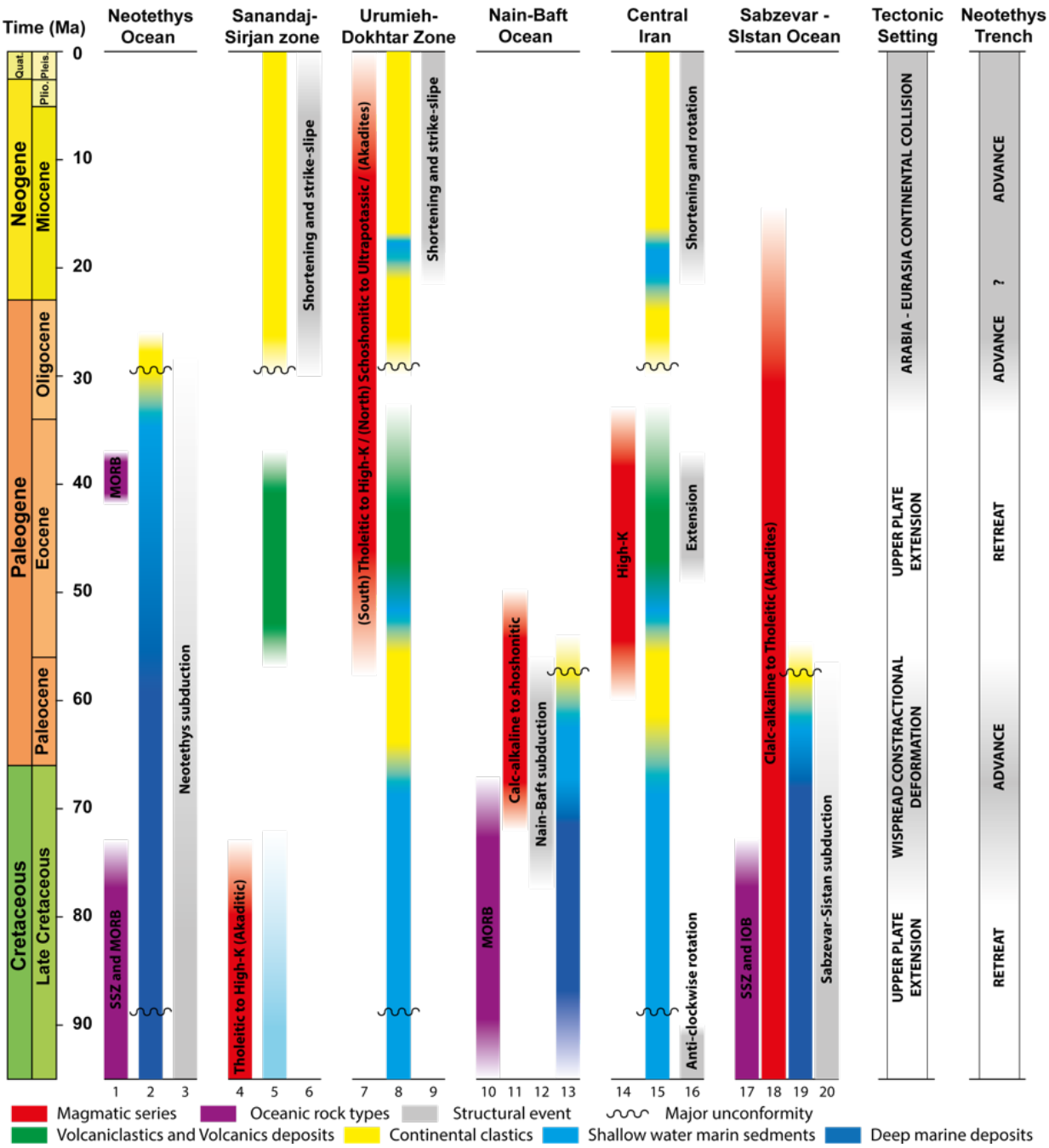

Figure 4.2: Tectonic and magmatic chart of the western Cimmerian domain constituting the upper plate of the Neotethys subduction system. Horizontal axis gathers the main structural units from SW to NE. Right vertical axis shows of the major Tectonic events in the region and the Neotethys interpreted trench advance and retreat episodes. See Fig. 4.1 for the location of the structural areas. **1:** *Aghanabati & Rezai, 2009; Ali et al., 2012; Allahyari et al., 2014; Aswad et al., 2011; Babaie et* al., 2006; Ghasemi et al., 2002; Monsef et al., 2010; Saccani et al., 2014; Shafaii Moghadam & Stern, 2015; **2: and 3:** *McQuarrie & van Hinsbergen, 2013*; **4:** *Azizi et al., 2018; Azizi & Jahangiri, 2008; Badr et al., 2013; Chiu et al., 2013; Mazhari et al., 2013; Nouri et al., 2016; Omrani et al., 2008; Sepahi & Athari, 2006*; **5:** *Falcon, 1974***; 6:** *Agard et al., 2005, 2006***; 7.** *Chiu et al., 2013; Omrani et al., 2008***; 8:** *Saidi et al., 1997***; 9:** *François et al., 2014***; 10:** *Pirnia et al., 2018; Shafaii Moghadam et al., 2009***; 11:** *Omrani et al., 2008***; 12:** *Ghazi et al., 2012***; 13: and 14:** *Chiu et al., 2017; Verdel et al., 2007***; 15:** *Aghanabati & Rezai, 2009; Allen & Armstrong, 2008; Saidi et al., 1997; Wilmsen et al., 2005, 2009, 2015, 2018***; 16:** *Mattei et al., 2017; Morley et al., 2009; Verdel et al., 2007***; 17:** *H. Omrani, 2018; Shafaii Moghadam et al., 2014***; 18:** *Chiu et al., 2013, 2017; Jamshidi et al., 2015; H. Omrani, 2018; H. Omrani et al., 2018; Pang et al., 2013, 2014; Rossetti et al., 2014; Shafaii Moghadam et al., 2014, 2016***; 19: and 20:** *Rossetti et al., 2010; Zarrinkoub et al., 2012*

4.3 Tectonic reconstruction since the Cretaceous

The relative convergence velocity between Africa and Eurasia show large fluctuation (e.g., *Dewey et al., 1973; Seton et al., 2012*). During the late Cretaceous, convergence velocity exceeded 6 cm/yr and then slow down to 2-3 cm/yr (*Seton et al., 2012*). The deformation of the upper plate is sensitive mainly to the relative motion between Eurasia and the trench. Thus, we considers the amount of deformation previously discussed for the Iranian mobile belt as a proxy for the trench migration history relative to the almost stationary Eurasia, i.e., assuming negligible erosion or accretion at trench. During the last 80 Ma, subduction velocity can be estimated by summing up the trench velocity with the convergence velocity (Fig. 4.3). The velocity pattern show oscillation derived from trench motion alternating episode of trench retreat and trench advance. Prior to 80-90 Ma, the Neotethys ocean was actively spreading. Therefore, the convergence velocity represents only a minimum estimate of the subduction velocity.

Based on the previous information, we reconstruct the evolution of the region along a cross-section crossing all the tectonic domain from ca. 90 Ma to present (Fig. 4.4).

A. 90 Ma, Late Cretaceous. Neotethys trench retreat and slab-rollback. Opening of the Nain-Baft back-arc basin.

Magmatic activity of the Sanandaj-Sirjan zone indicates northward subduction of the Neotethys ocean at least from the middle Cretaceous (Fig. 4.4A; e.g., *Ao et al., 2016; Leterrier, 1985; Torsvik et al., 2012*). In the upper plate domain, i.e., the western Cimmerian domain, the Nain-Baft oceanic basin opened during the Late Cretaceous suggesting the occurrence of upper plate extension led by trench retreat (Fig. 4.2; 4.4; *Agard et al., 2011*). Note that further East, in Eastern Iran, the spreading of the Sabzevar-Sistan oceanic basin is partly synchronous to the Nain-Baft basin opening (120-110 until 77,8 Ma; *Rossetti et al., 2010; Shafaii Moghadam et al., 2014; Zarrinkoub et al., 2012*). Therefore, we estimate the Neotethys trench retreat of at least 300 km assuming 150km of extension for each back-arc basin. The Cretaceous geochronological ages dispersion suggests continuous oceanic spreading for the Neotethys from 110 Ma to 73 Ma; *Shafaii Moghadam & Stern, 2015* and reference therein). Geochemical analysis, however, shows magmatic signatures evolving from MORB to supra-subduction zone (Fig. 4.4A). Thus, during Middle Cretaceous, an oceanic ridge formed in the SW part of the

Neotethys, allowing the development of MORBs. Rapidly, this ridge was inverted leading to the Northward intra-oceanic subduction of the southern part of the Neotethys followed by the obduction of the central part of the Neotethys above the distal parts of the Arabian plate margin (Fig. 4.4B; e.g., *Agard et al., 2005, 2011; Burg, 2018; Duretz et al., 2016*).

B. 60 Ma, Early Paleocene. Neotethys trench advance, closing of the Nain-Baft back-arc basin

During Late Cretaceous and early Paleogene times, the Nain-Baft oceanic basin was rapidly closed through the subduction beneath Central Iran (Fig. 4.4B; *Shafaii Moghadam et al., 2009*). The Sabzevar-Sistan oceanic basin was also closed via northward subduction starting from the Paleogene (e.g., *Rossetti et al., 2010)*. Thus, if we consider the central Iranian domains as rigid blocks, shortening of the whole upper plate (i.e., the western Cimmerian domain) can be estimated of at least 150 km and has to be related to trench advanced. This event could have triggered the regional shortening documented in the northern part of the Central Iranian domain and in the Alborz and Kopeh Dagh ranges (e.g., *Allen et al., 2003; Ballato et al., 2011; Guest, Stockli, et al., 2006; Madanipour et al., 2017*). The closing of the Sabzevar back-arc occurred slightly later, during the Paleogene, allowing additional 150 km of trench advance.

C. 45 Ma, Early Eocene. Upper plate extension and Neotethys slab roll-back

During Paleogene, large core-complex and exhumation of high temperature-low pressure metamorphics in Central Iran indicate upper plate extension (e.g., *Alamdarie Malekpour, 2017; Kargaranbafghi et al., 2012; Moritz et al., 2006; Shafaii Moghadam et al., 2016; Verdel et al., 2007*). In the NW Sanandaj-Sirjan zone, the occurrence of coeval ophiolites suggests Neotethys oceanic spreading in a supra-subduction context. This is produced by slab roll-back (Fig. 4.4C; *Verdel et al., 2011*). The migration of the volcanic arc from the Sanandaj-Sirjan zone toward the Urumieh-Dokthar magmatic arc suggest a decreasing of the slab angle. A volcanic activity flare-up over large part of Iran suggest a vigorous mantle convection episode and heating of the whole upper plate (*Agard et al., 2011; Verdel et al., 2011*). This extensional episode is in the order of some tens of kilometres. This period corresponds also to the deposition time of nummulitic limestone (e.g.; *Aghanabati & Rezai, 2009; Saidi et al., 1997*) suggesting the subsidence of the upper plate.

D. Onset of Arabia-Eurasia collision. 30 Ma, Early Oligocene

The onset of Arabia-Eurasia collision is still debated (e.g., *Agard et al., 2005; Ballato et al., 2011; Koshnaw et al., 2018; Mouthereau, 2011; Pirouz et al., 2017*). Here, we consider Upper Miocene-Oligocene as the most reliable age for the onset of continental subduction in the central part SW Iran, i.e. the central part of the Sanandaj-Sirjan zone (Fig. 4.4D; e.g., *Agard et al., 2011; McQuarrie & van Hinsbergen, 2013*).

E. Present day section

Since the onset of the Arabia-Eurasia collision, the lower plate has been progressively integrated into the collisional wedge and the deformation has been propagated toward South-West in the Arabian plate. The Neotethys ophiolites and the distal part of the Arabian margin were first subducted below the Iranian margin during Early Oligocene times (e.g., *Agard et al., 2005; Ballato et al., 2011; Koshnaw et al., 2018; Pirouz et al., 2017*).
Starting from the Early Miocene (*Barber et al., 2018; Gavillot et al., 2010; Mouthereau, 2011*) the deformation occurred into the more proximal part of the Arabian margin to form the present High Zagros. Deformation then propagated toward SW leading to the formation the Zagros Fold and Thrust belt and to the thickening the crust up to 50-60 km (Fig. 4.4E; e.g., *Paul et al., 2006*). In the upper plate domain, collisional deformation started with the shortening, exhumation and the thrusting of the Sanandaj-Sirjan zone above the Neotethys ophiolites during the Oligocene (Fig. 4.2; e.g., *Agard et al., 2005; Barber et al., 2018; François et al., 2014*). From the Early to middle Miocene , collisional deformation affected progressively the central part of the Iranian domain with exhumation of the Urumieh-Dokhtar Magmatic Arc (*François et al., 2014*) together with the anti-clockwise rotation of the Yadz-Tabas and Lut micro-blocks (Fig. 4.2; *Allen, 2010; Mattei et al., 2015*). Arabian -Eurasian collision propagates then to the Talesh-Alborz and Kopeth-Dag area, triggering the shortening of the range from the Early Middle Miocene (*Allen, 2010; Ballato et al., 2008, 2015; Guest, Stockli, et al., 2006; Madanipour et al., 2018; Mattei et al., 2017; Rezaeian et al., 2012*). During Early to Middle Miocene times an episode of extension (to transtension) is suggested for Central Iran suggesting temporal variations of the convergence velocity (*Morley et al., 2009*). The last step of the collision included the oroclinal bending of the Talesh-Alborz and Kopet-Dagh range around the South Caspian Basin (SCB), and the subduction of the SCB beneath the Absheron Ridge where an accretionary prism formed since the Late Miocene (*Allen et al., 2003; Ballato et al.,*

2015; Cifelli et al., 2015; Green et al., 2009; Mammadov, 2008). From published geological data, it is possible to estimate ~250km of shortening accommodated within the upper plate since 30 Ma (e.g., *Green et al., 2009; Guest et al., 2006; Morley et al., 2009*) while ~100km in the lower plate (e.g., *Blanc et al., 2003; McQuarrie, 2004; Sherkati et al., 2006*) of the former trench position toward the upper plate since the onset of the collision (Fig. 4.4E). During Early Miocene the shortening of the upper plate is coeval to the deposition of the Qom formation which spreads in the Western Cimmerian domain *(Aghanabati & Rezai, 2009; Saidi et al., 1997; Stoneley, 2015*). This suggests that the upper plate gets shortened while subsiding.

Summing up, the opening and closing of back-arc basins indicate that the upper plate is deformed by two episodes of extension and one of compression followed by continental collision. Here, we propose that this may have produced by oscillation of trench due to deep slab folding. We test this hypothesis using numerical models described in the next paragraph.

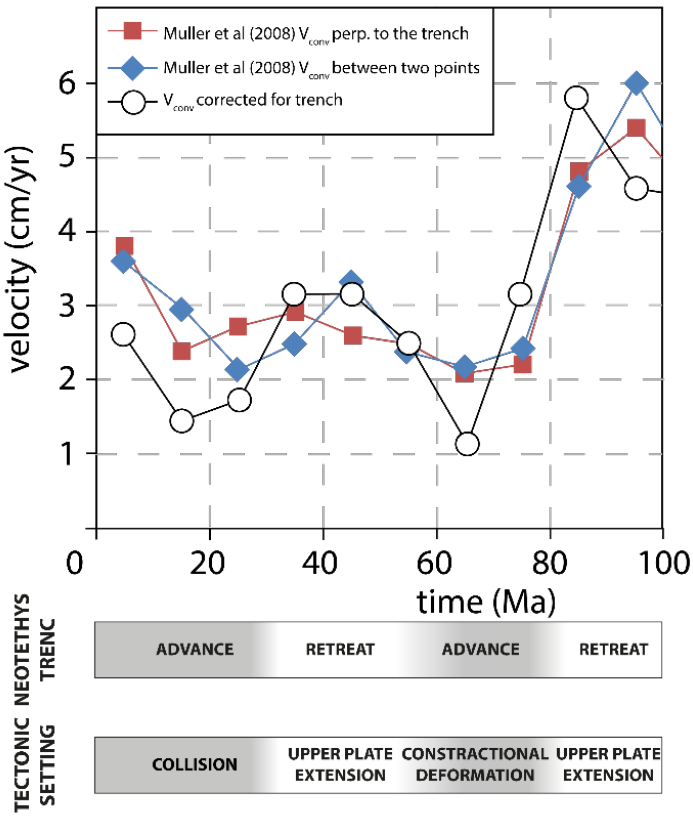

Figure 4.3: Subduction velocity (white dots) along the cross-section AB (see Fig. 4.1 for location) estimated by summing up the convergence velocity between Arabia and Eurasia perpendicular to trench. Subduction velocity should have been higher as it should include unknown Neotethys spreading velocity. For comparison we also show the convergence velocity (*Müller et al., 2008*).

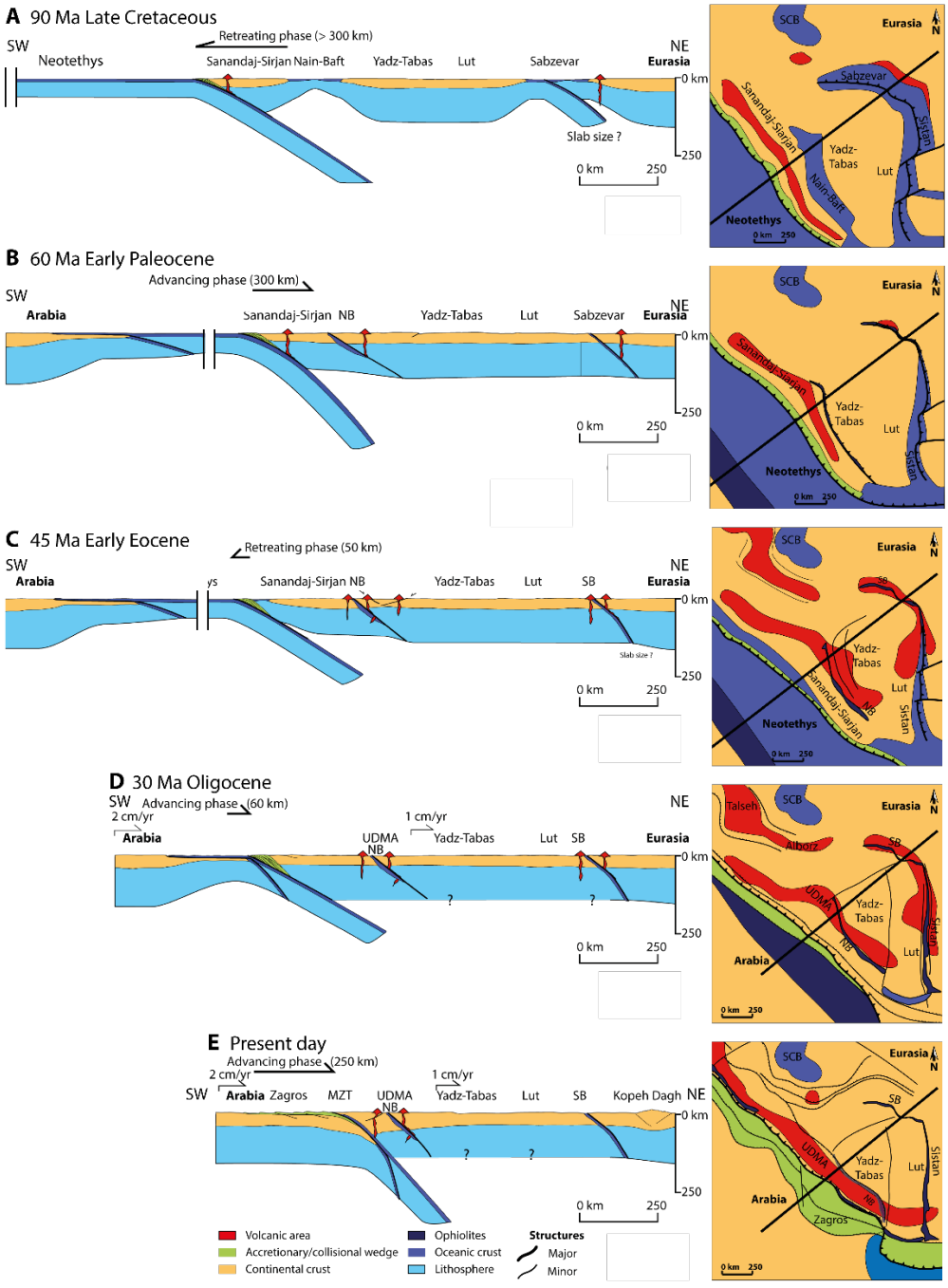

Figure 4.4: Schematic cross-sections and relative maps for the central Neotethys domain. **A.** Mid to Late Cretaceous, ante 90 Ma stage. Since Early Cretaceous, the Neotethys trench is largely retreating, at least 300km, leading to Nain-Baft back-arc opening. **Panel B.** Early Paleocene, ca. 60 Ma. The Neotethys trench advance, of about 180km, trigger the subduction and closing of the Nain-Baft and Sabzevar-Sistan back-arc basin the shortening of the Iranian domain. **Panel C** Early Eocene 45 Ma,. The Neotethys trench slightly retreat, of about 50 km, driving the extension and core complex formation in Central Iran. Neotethys fore arc basin develops in a supra-subduction mode SW to the Iranian margin. **D-E.** Since the Oligocene, the Neotethys suture advanced northward producing shortening in the Sanandaj-Sirjan zone, Central Iran and Kopet-Dag and leading to the northward migration of the volcanic arc (Urumieh-Dokthar Magmatic Arc). NB: Nain-Baft back-arc basin; UDMA: Urumieh-Dokthar Magmatic Arc; SCB: South Caspian Basin.

4.4 Numerical model results

4.4.1 Model set up

We use a thermo-compositional 2D numerical model of single-sided subduction to investigate how deep slab deformation may produce episode of trench advance and retreat episodes. Model presented here is performed in a Cartersian geometry. The numerical model set-up is similar to that of *Briaud et al.* (*under review*) (Fig. 4.5). We use the finite element code CITCOM to solve the governing equations in an incompressible (Boussinesq approximation) viscous fluid with negligible intern and zero internal heating (*Wang et al., 2015; Moresi and Gurnis, 1994*). The reference viscosity of the model is 1×10^{20} Pa s. The thermal initial condition is 2773K and the core-mantle boundary (CMB) and 273K at the surface. For simplicity, the continental upper plate is defined by a constant temperature as opposed to the subducting plate, which is defined by the half-space cooling. To decouple both plates, the oceanic crust is added at the top of the subducting plate (1×10^{20} Pa s), 7.5 km thick. The continental crust is defined using compositional tracers with a uniform thickness of 30 km.
To model the large-scale mantle convection, a stratified the mantle is used. The upper mantle ranges from the surface to 670 km depth and the lower mantle from 670 km to the CMB. To approximate the temperature-pressure dependent viscosity of the olivine, we use a Newtonian rheology (diffusion creep) and a maximum viscosity cut-off in order to avoid non-realistic surface strength. The 670 km depth discontinuity is considered as a combination of jump of viscosity of few orders of magnitude with the 670 km depth endothermic phase transition of the walsdeylite-ringwoodite to post-spinel. The viscosity contrast provides a resisting for the slab penetration due the abrupt increasing of lower mantle viscosity about $\mu_{LM}=70\mu_{UM}$. The endothermic phase transition generates positive buoyancy force that gets the slab ponding, at least temporarily into the mantle transition zone (MTZ) (e.g., *Agrusta et al., 2017; Christensen, 1985; Čížková, & Bina, 2013*). This combination may inhibit the flow between the two mantle domains. The 410km discontinuity is characterized by the transition of olivine to walsdeylite, leading to negative buoyancy force which enhances the pull of the slab. The 1-D viscosity structure of the whole model is showed in Figure 4.5b.

The subduction is initiated by prescribing an asymmetric geometry in the trench region, which provides the initial instability required for free subduction. The slab is thus, extended to 200 km depth with a radius curvature of 500km. The box domain has a depth of 3000km which corresponds to the whole mantle depth. The aspect ratio of the depth versus the width of the

model is 1:3. On the left end side of the model, a mid-ocean ridge is imposed whereas the zero-heat flux is considered on the trailing edge of the upper plate (Fig. 4.5a). Hence, the upper plate is mobile relative to the right side of the box. All boundaries are considered as an impermeable (i.e., free slip boundaries). As a result, the mantle convection is restricted to the size of the domain and driven by the internal buoyancy forces. The rectangular non-uniform mesh is defined by 2880×472 elements where the finest elements size of 2.5 km^2 is localized on the trench region.

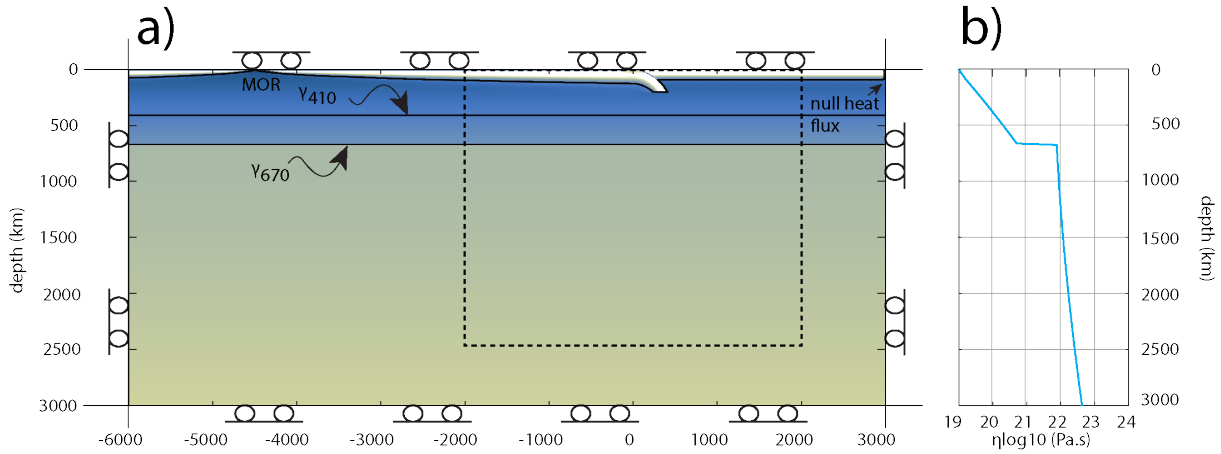

Figure 4.5: a) Sketch of the model domain at t=0 Ma of a subducting lithosphere with and initial plate age of 100 Ma. The background colours indicates the viscosity, while the two horizontal black lines (Y_{410};Y_{670}) represent the equilibrium position of the phase boundaries of olivine-wadsleyite at 410 km depth and the post-spinel transition at 670 km depth. Two oceanic ridges of the subducting plate (MOR) and the upper plate (null heat flux) are also indicated. Little rollers on the box sides correspond to the free slip boundary conditions. b) 1-D viscosity structure of the mantle used in this study.

4.2.2 Model results

We run a series of model to show the influence of the slab, exploring the parameter range of the 410 km ol-wd (y_{410}) and the post-spinel (y_{670}) phase transition on slab penetration and slab folding at transition zone (*Běhounková & Čížková, 2008; Tosi et al., 2015*).

Our reference model has a γ_{410}=-+5.0 MPa/K and γ_{670}=-3.0MPa/K, initial age of the subducting plate of 100 Ma and a lower mantle/ upper mantle viscosity increase of 70. Figure 4.6 illustrates the evolution of the model surface topography and how the horizontal (deviatoric) normal stress evolving as function of the slab folding dynamics at depth. The kinematics parameters (trench velocity, the plate convergence rate and slab dip angle) are in Figure 4.7.

Initially the slab sink into the upper mantle (Fig. 4.6a), producing compression (>40 MPa) close to the trench, upper plate extension at distance >1000 km and a flat dynamic topography signal of the upper plate of about 0km elevation (Fig. 4.6a top).

Then the slab reaches the upper/lower mantle discontinuity (Fig. 6b), and folds into the mantle transition zone (Fig. 4.6c). In this phase slab fold, retreats toward the lower plate and produces less back-arc compression while the surface topography remains flat.

Throughout the time spend by the slab to pile up into the transition zone (Fig. 4.6c, d), the slab folds forward and backward, producing trench advance and retreat. The shallow slab dip angle related to the trench retreat produce strongly asymmetric mantle flow, with large scale return flow focused on the wedge side of the slab (Fig. 4.6c). In contrast, the near steep dip angle associated to trench advance results in return flow cells of smaller size localised into the wedge side of the subduction zone (Fig. 4.6d). The decrease and increase in trench velocity (Fig. 4.7), the periodic variation of mantle flow in conjunction with the slab folding behaviour into the mantle transition zone, gives rise to abrupt variation of the stress state of the upper plate (Fig. 4.6c, d bottom), from compressional to extensional stress state. Moreover, this peculiar slab behaviour in time induces the tilting of the upper plate towards and fromward the trench, episodically (Fig. 4.6c, d top). Likely to what found in some previous studies (*Cerpa et al., 2015; Guillaume et al., 2009*), we do observe periodic variations in the upper plate stress/strain rate associated with the slab folding behaviour in the mantle transition zone.

Once the slab flush into the lower mantle the slab, it deflects into the MTZ. We observe the initiation of both long wave-length compressional stress state into upper plate and a tilting of the upper plate towards the trench in combination with the large-scale mantle flow. Indeed, the model exhibits into the upper plate a near linear increase in maximum compressive stress while the surface topography shows large-scale tilting towards the trench of about 2000 km (Fig. 4.6e). The horizontal length of the upper plate undergoing in significant compression >30 MPa, increasing rapidly after flushing at ~60Myrs. Similar results have been obtained by (*Faccenna et al., 2017; Yang et al., 2016*) about SE Asia and South America, respectively.

The Figure 4.7 indicates that the oscillation of the convergence velocity may be linked to the ability of the slab to fold into the mantle transition zone.

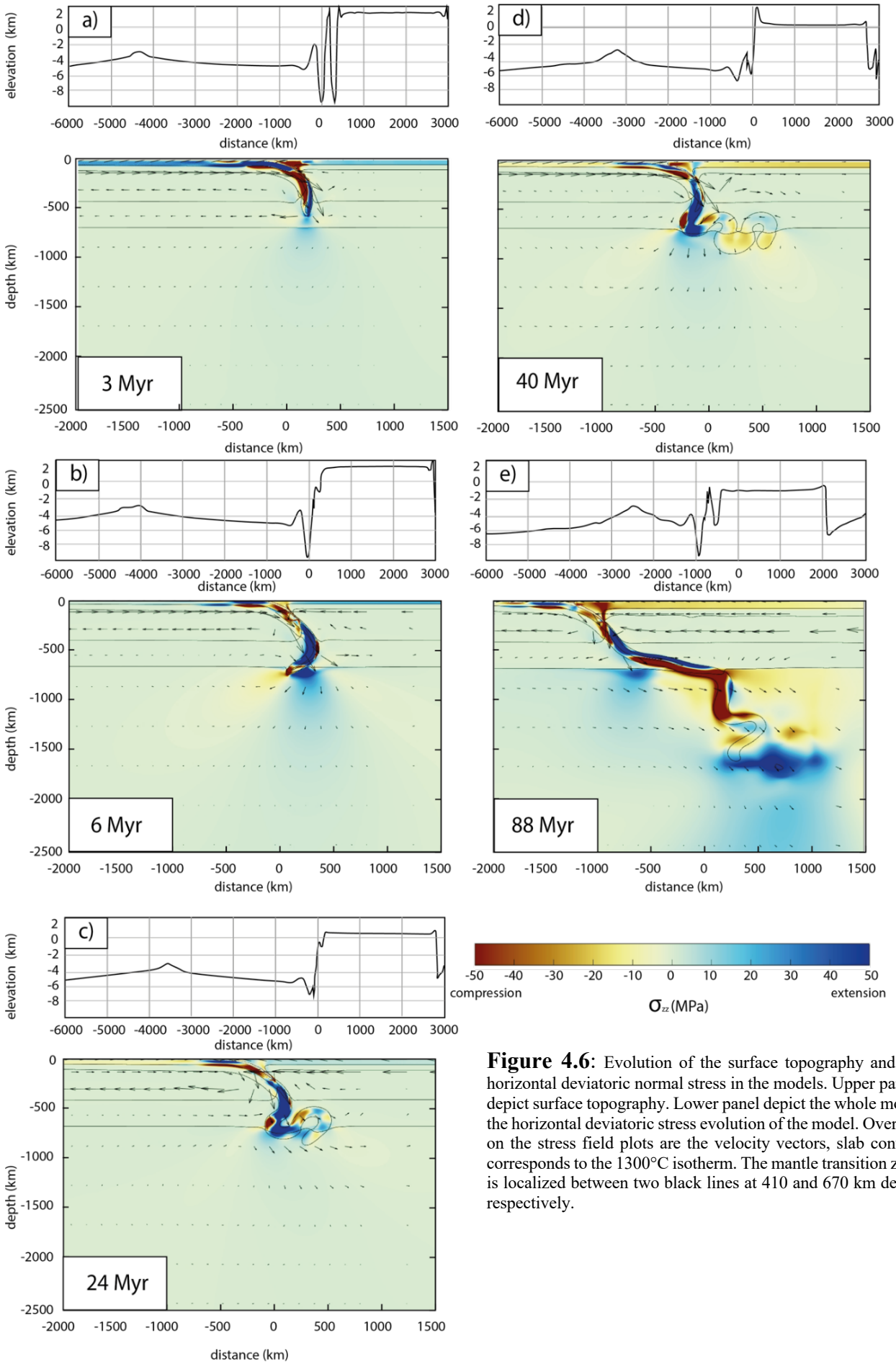

Figure 4.6: Evolution of the surface topography and the horizontal deviatoric normal stress in the models. Upper panels depict surface topography. Lower panel depict the whole model the horizontal deviatoric stress evolution of the model. Overlain on the stress field plots are the velocity vectors, slab contour corresponds to the 1300°C isotherm. The mantle transition zone is localized between two black lines at 410 and 670 km depth, respectively.

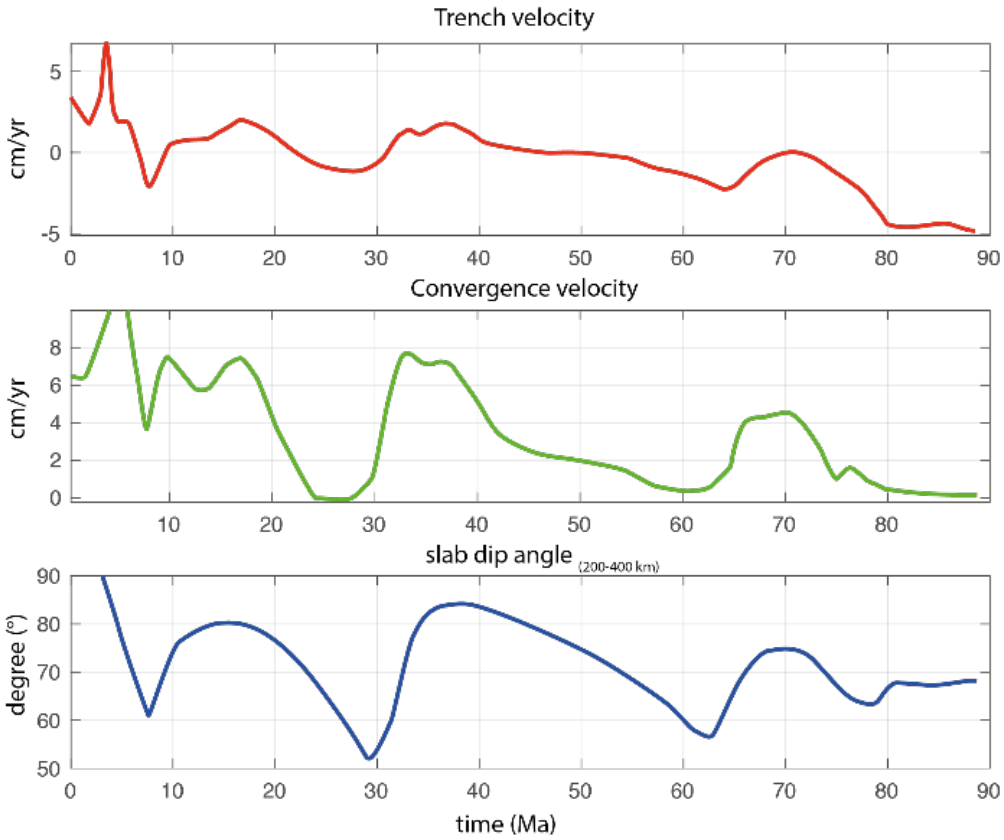

Figure 4.7: Kinematics and geometry features of the model

Figure 4.8 shows the result of model runs with the same mantle rheology and plate age, but different strength of the Clapeyron slopes at 410 and 670 km depth, changing so the ability of slabs to get ponding or penetrate the MTZ. We define two diagnostic parameters *P* and *S:* P represents the amplitude of the distance between peak on convergence velocity while *S* (dimensionless with respect to the mantle depth) corresponds to the maximal slab tip depth. These parameters allow us to separate our models into four slab morphology clusters. 1) Low, or no periodicity of the convergence rate and wide range of slab depth; 2) folding slab in the whole mantle and 3) folding following by a flushing event into lower mantle; 4) slab flattening at the base of the upper mantle.

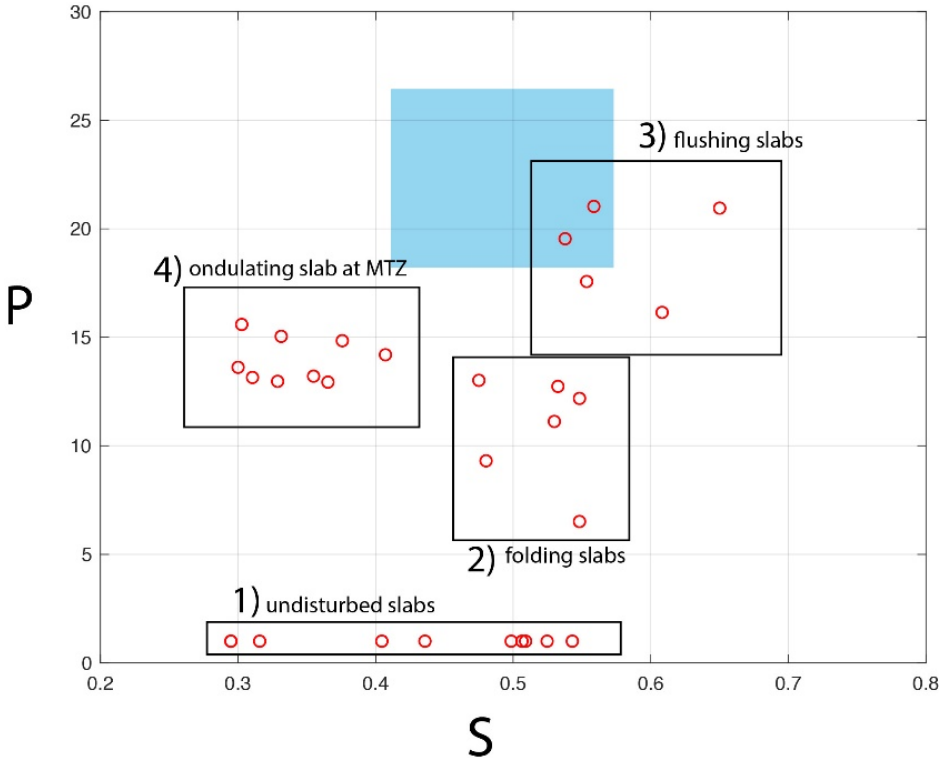

Figure 4.8: Diagram plotting *P* against *S*. As indicated in the diagram, the symbol colours represent the strength of the Clapeyron slopes. The blue area corresponds to the plausible location of the Iranian slab inferred form tectonic reconstruction (Fig. 4.4) and tomographic images.

4.5 Discussion

In the diagram Figure 4.8, it appears that the Iranian slab matches with the folding and flushing slab behaviour of our set of 2-D numerical models (Fig. 4.6).

Our 2D numerical models provide information on slab dynamic at the MZT and how it affects the overriding plate stress state and the topography. Models shows that the slab folding behaviour into the MTZ and flushing events into the lower mantle happens with both stratified mantle viscosity and relatively high Clapeyron slopes strength. The slab behaviour into the MTZ is accompanied by slab thickening and folding due to the increased resistance to slab penetration into the lower mantle. When the slab piles up into the MTZ, we observe episodic changing into stress states as well as the topography of the upper plate. The large-scale extensional stress state and the surface topography low of the upper plate are observed when the slab rolls back with respect to the upper plate. In contrast, the onset of large-scale compressional stress state in the upper plate is observed when the slab folds over, toward the upper plate which induce surface topography high. Model show that the surge of compression during the flushing event is due the onset of increasing trench retreat velocity, shallow slab dip angle and decreasing convergence velocity. As consequence, the upper plate is pushed, shortened and tilt towards the trench, similar to that predicted by authors (*Crameri & Lithgow-Bertelloni, 2017; Faccenna et al., 2017; Liu et al., 2008*). Our models are not designed to investigate specific settings and can be only broadly compared with the Central Iran system. However, it provides first order information on the way compressive and extensive stresses occur during the progression of slab folding into the MTZ followed by flushing in the deep mantle. Those general rules help us to guide our interpretation of the past subduction history of the Central Iran.

We select the central Iran region to restore the plausible evolution of the subduction slab and the stress and topographic features of the upper plate before the onset of the collision ~30 Ma ago. A tomographic cross section from GAP-P4 P-waves models (*Fukao & Obayashi, 2013*) shows the presence of deep slab down to 1500 km depth and the associated slab shape gets progressively thicker into the lower mantle (Fig. 4.9). Similar features have been observed in other tomographic models (e.g., *Ritsema et al., 2004; Simmons et al., 2010*), and resolution tests show that the widening effect is not an artefact of the inversion model. To provide a rough estimation of the amount of subducted material, we measured the area of the main high velocity

anomalies along the cross section. The retro-deformation of the slab is performed considering both amount of subduction and upper plate deformation. At each step we subtract the amount of subducted material in Figure 4.9 starting from present day setting.
Reconstructions in Figure 4.9 shows that the slab starts to anchor into the upper and lower mantle discontinuity prior to 100 Ma. Then, from 90 to 30 Ma, the episodic back arc opening and shortening may be induced by the folding of the slab at depth favouring trench advance and retreat behaviour. Folding events at MTZ depth may explain the phase of compressional and extensional episodic stress state of the Central Iran which is reflected in our model by the variation of deviatoric stress feature (Fig. 4.6) as already highlighted in (*Faccenna et al., 2017; Guillaume et al., 2009*). It is thus, plausible that the back arcs openings and closures into the western Cimmerian domain may be related to the deep folding slab behaviour.

According to our reconstructions, the opening of the Sabzevar-Sistan ocean (120-100 Ma, e.g., *Rossetti et al., 2014; Zarrinkoub et al., 2012*) could be related to the anchoring and the retreat of the Neotethys slab in the MZT. During Late Cretaceous, the slab continued to retreat leading to the opening of the Nain-Baft back-arc basin close to the trench (Fig. 4.9A). We estimate the upper plate extension at a minimum of 300km in total to allow the two oceanic break ups. Yet this estimation could vary along strike as this extension is coeval to the Central Iran anti-clockwise rotation (*Mattei et al., 2015*). This suggests 3D effect of the slab flattening at the MTZ impacting the upper plate deformation. Until 90 Ma the stretching of the upper plate and Neotethys trench retreat seems to be continuous. Between 90 and 60 Ma as the Nain-Baft back arc basin was opening, Central Iran area recorded exhumation and erosion but no major signs of shortening (e.g., *Wilmsen et al., 2015*). Which led us assume that rotation of Central Iran went together with its exhumation but with no signs of upper plate shortening. Thus, we propose that the Neotethys slab flatten and did not fold at the MTZ before 60Ma (Fig. 4.9A, B). The closure initiation of the Nain-Baft and of the northern part of the Sabzevar-Sistan oceanic domains during Late Cretaceous-Paleocene times shows the shortening of the upper plate. This event is associated to the Neotethys trench advance led by the folding of the slab at the MZT (Fig. 4.9B). The advance of the slab and the associated shortening of the upper plate went on until Eocene times. During Eocene, the upper plate recorded extension, a peak of magmatism as well as marine flooding is deciphered all over the upper plate (Fig. 4.2). This is interpreted as led by the retreat of the Neotethys slab. During Oligocene, the Neotethys trench advances preceding possibly the onset of the collision and led to slab roll over towards the upper plate (Fig. 4.9D). Moreover, the present-day the slab shape is localized bellow the MTZ. The

flooding event all over the Western Cimmerian domain and showed by the deposition of the Qom formation (Fig. 2) could be linked to the flushing of the subducted Neotethys slab into the lower mantle (Fig. 4.9C). Indeed, the model describe a large-scale tilting of the upper plate toward the trench once the slab propagates down to the lower mantle. In the Iranian case, after the onset of collision and during the former trench advance, the deposition of shallow marine limestone (i.e. the Qom formation during Early Miocene) depicts subsistence of the upper plate far from the Neotethys suture. These slab flushing from ~20Ma to present day led us to estimate the slab sinking velocity into the lower mantle at ~4cm.yr^{-1} which slightly higher than literature estimations (~2cm/yr; *Čížková et al., 2012*). After this flushing event, no clear event of extension is deciphered into the upper plate (Fig. 4.2) suggesting no major folding of the slab at depth or that collision predominates on the slab behaviour on the upper plate deformation.

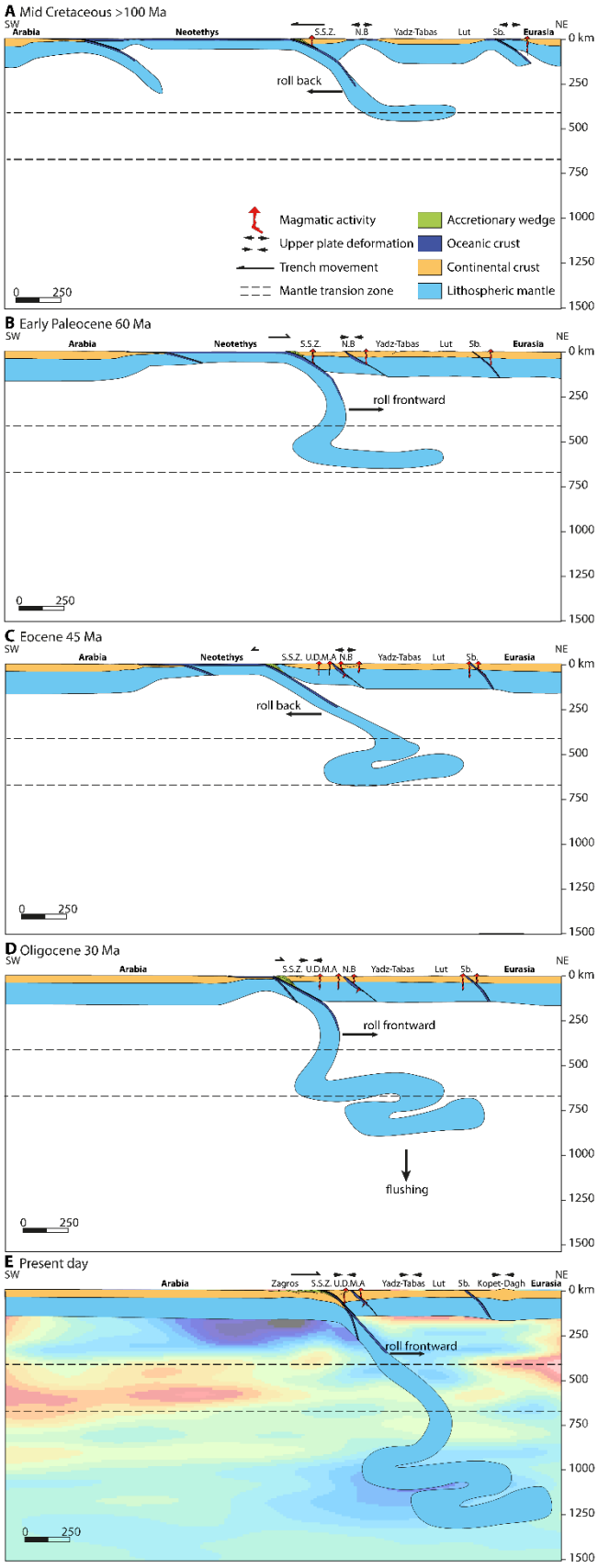

Figure 4.9: Interpreted tomographic section and reconstruction of subduction system along a SW-NE section. See Figure 1 for section path location. N.B.: Nain-Baft; Sb. Sabzevar; S.S.Z. Sanandaj-Sirjan zone; U.M.D.A. Urumieh-Dokthar Magmatic arc.

4.6 Conclusion

In this study we used a joined numerical and natural data investigation to decipher the history of the Neotethys subduction system. We explored how the slab dynamics may affected the surface deformation of the western Cimmerian domain since Mid Cretaceous. Thanks to natural data compilation, plate kinematic reconstruction, numerical modelling and tomographic images we show that the folding slab behaviour into the mantle transition zone had a profound impact on the western Cimmerian domain structural evolution.

We demonstrate that folding slab behaviour at the mantle transition zone discontinuity is driven by stratified mantle viscosity in combination with the presence of 410km and 670km depths Clapeyron slopes. The folding slab into the MTZ drives the episodic trench migration as well as the large-scale topographic evolution and deformation of the upper plate. In Iran, the Neotethys ocean subducted below the western Cimmerian domain before the onset of the collision between Arabian and Eurasia. We estimate the trench motion and the upper plate deformation. The opening of the Nain-Baft and Sabzevar-Sistan back-arc basins during middle to Late Cretaceous is related to the roll back of the Neotethys slab. The basin closures during Paleogene is triggered by roll over slab behaviour. The extension and marine flooding of the upper plate during Eocene is related to the roll back of the slab. Since the onset of the Arabian Eurasia collision, the trench is advancing showing the folding and the roll frontward of the Neotethys slab. At early Miocene times, the onset of the slab avalanche into the lower mantle induces wide marine flooding spreading on the upper plate.

Chapter V

Lateral variability of slab interacting with the mantle transition zone

In this chapter simple 2D and 3D numerical models characterized by an ocean-ocean single-sided subduction zone are presented with the aim to unravel the role played by the lateral width variability of the slab while interacting with the mantle transition. For this purpose, it has been analysed if and how the dynamic topography is differently affected by the 3D slab dynamics at depth.

5.1 Introduction

How slabs interact with the transition zone (MTZ) remains enigmatic. We observe this process thanks to indirect observables such as tomographic images, that show only the present-day apparent slab morphology recognizing a wide range of behaviours of subducting plates while interacting with the MTZ. A straightforward example of this variability is recognized beneath the South American plate (Fig. 5.1). But which is the cause of the slab deep variability?

Previous studies have shown that changes in plate rheology (e.g., buoyant ridge; old oceanic lithosphere ; *Agrusta et al., 2017; Agrusta et al., 2018; Martinod et al., 2016*), mantle rheology (e.g., *Agrusta et al., 2017; Billen & Arredondo, 2018; Goes et al., 2017*) plate kinematics (e.g., far-field tectonics; *Husson et al., 2012; Lee & King, 2011; Yamato et al., 2013*) may affect the slab behaviour at depth.

In chapter 3, thanks to 2D numerical models, I have investigated how the slab dynamics is dependent on mantle rheology (i.e., γ_{410}; γ_{670}; A_{lower}) and on plate strength (A_{plate}). That chapter concludes that slab dynamics is radically affected by the strength of Clapeyron slopes (γ_{410}; γ_{670}) combined to mantle layering. The strength of the subducting plate plays a second-order role on the slab dynamics. By tuning these parameters (γ_{410}; γ_{670}; A_{lower}; A_{plate}), the behaviour of slabs falls into four categories: from slab sinking into the lower mantle, to slab fold or stagnate into the MTZ. Those slab categories exhibit also characteristic upper plate dynamic topography variation in space and time that, if unravelled, reflect the enigmatic deep dynamics. It still remains unclear if the lateral length variability of the slab plays any role in its behaviour and the resulting upper plate dynamic topography.

Just with the purpose to clarify the role played by the lateral slab width, I have realised a study of 3D numerical models characterized by differently long slabs interacting with the MTZ. It is challenging to verify if specific shallow surface fingerprints of convergent margins are affected by the slab length, following the idea that these superficial features might mirror the

deep behaviour of the lithosphere (*Flament et al., 2013; 2014*). This work is summarized in this chapter which is structured as follow:

- It is first presented a simple 2D reference model of the flat slab into the MTZ. This model has the same mantle rheology than the 2D models presented in Chapter 3 section 3.3.4 and a reshaped resolution mesh to improve the computational performances.

- Second, I have added to the previous 2D modelling efforts a set of 3D models investigating how the 3D lateral boundary condition may change the slab dynamics.

- Third, I realized additional 3D models to highlight the role played by the slab length in tuning its deep behaviour.

- Finally, the chapter ends by quantifying if and how the upper plate dynamic topography is controlled by the length variability of slabs.

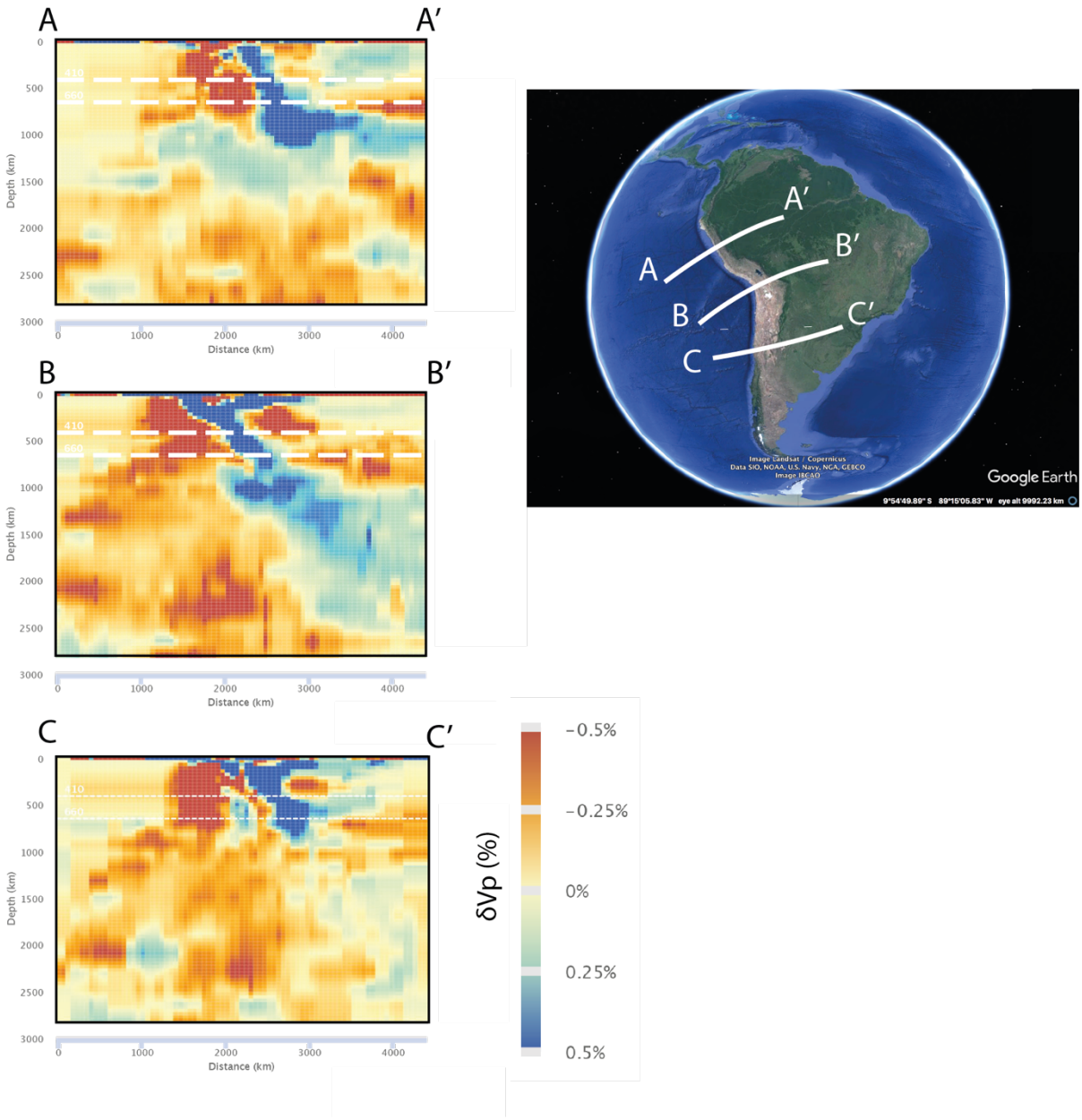

Figure 5.1: (Left) P-wave tomographic cross section beneath the South American plate (ww.atlas-of-the-underwold.org). HADES tomographic explorer (UUP07). (Right) Locations of the P-wave tomographic cross-sections perpendicular to the trench.

5.2 Method

The scope of this chapter is to test (i) how slab dynamics is affected by the lateral boundary conditions; (ii) to decipher if the slab width (W_{plate}) controls its behaviour at depth and (iii) how the upper plate dynamic topography vary along two-end members trench width (W_{plate}).

To answer to these questions, I use numerical models having a specific combination of mantle (i.e., A_{lower}, phase transformations), plates and slab properties (i.e., strength and buoyancy) which determine the flat slab behaviour at the mantle MTZ (*Agrusta et al., 2017; Christensen, 1996; Garel et al., 2014*) (see Chapter 3; Table 3.2). This choice allows to appreciate variations in slab morphology within a steady slab dynamic state.

The 3D model domain is 3000 km deep, as previously setup for 2D models (Chapter3). The model width is 4500 km long in the x-direction (Fig. 5.2). Free-slip boundary conditions are applied to all the lateral boundaries as well as to the top and bottom of the models' domain. The finest resolution used for model computation is 10 km^3. This mesh size has been used to optimize the computational time after having checked that velocity differences between fine and coarse meshes do not exceed 10 % (see Chapter 2, section 2.6).

The temperature boundary condition is initially defined as follows: 273 K at the surface and 2773 K at the bottom of the model domain, in agreement with what has been done for the 2D models (Chapter 3). Hence, the thermal buoyancy generates a density contrast between the lithosphere and the underlying mantle which drives the subduction process. The initial temperature field of the upper and lower plates follow the half-space cooling model for a given plate age (e.g., *Turcotte and Schubert 2002*). Hence, the age of plates increases from 0 Ma to 100 Ma (i.e., thickness of about 110 km) moving from mid-ocean ridges to the trench (Fig. 5.2).

The upper plate is mobile thanks to mid-oceanic ridges imposed to the top right corner of the model. In the oceanic plate, a mid-oceanic ridge (MOR) is also imposed at 2000 km from the trench (Fig. 5.2a). As initial condition, the lithosphere is bent inside the mantle to reach the critical amount of an unstable wedge (corresponding to about 200 km in nature) to initiate subduction (Fig. 5.2). The problems linked to initiation of subduction are beyond the scope of this thesis. The initial bending radius of slabs is of about 500 km. This radius mirrors the average present-day radius of natural slabs (*Lallemand et al., 2005*).

At the top of both the lower plate and the subducting lithosphere, a thin oceanic crust about 10 km thick and with a low viscosity of $2x10^{20}$ Pa s is present down to 200 km depth to enhance the decoupling between the plates.

Transform faults are also implemented on the plate edges. For all the 3D cases, transform faults have the same thickness than the lithosphere (~100 km) and width comparable to the weak layer settled at the top of the subducting plate (about 10 km). The transform fault has the same viscosity than the top subducting plate weak layer (Fig. 5.2c). This simple configuration allows for mantle circulation around the slab edges and minimize possible boundary condition effects (Fig. 5.2b). Plate motions are thus enabled by the presence of weak transform faults.

A rheology with a linear stress dependency is used for both mantle and lithosphere in combination with a maximum yield strength of 300 MPa (see Chapter 2; Eq. 2.16; Eq. 2.19). Moreover, a maximum viscosity of 10^{24} Pa s is imposed, to avoid a non-realistic high strength at the surface. Both 410 km and 670 km depths Clapeyron slopes (i.e., γ_{410} and γ_{670}, respectively) are also assumed with values of +2.0 MPa/K and -2.0 MPa/K, respectively. The density increases for a mantle composed of 100 wt% of olivine associated with the phase changes are $\Delta\rho_{410}$ = 250 kg/m^3 and $\Delta\rho_{670}$ = 350 kg/m^3 for γ_{410} and γ_{670}, respectively (e.g., *Faccenda & Zilio,* 2017). Moreover, there is a viscosity contrast between the lower and upper mantle (see Eq. 3.8, Chapter 3, Table 3.1).

To study the influence of 3D lateral boundary conditions (i.e., distance between the plate and the domain side, Y_1; Fig. 5.2b) on subduction dynamics, two different models domain have been set-up as follows:

(1) half of the model along the mid-plane;

(2) models with free edges where the subduction system is localized in the centre of a wider box (Fig.5.2). Y_1 varies from 0.5 to 1x *h* for the setup (1) and is Y_1=Y_2= 0.5x*h* *for the setup (2), being h* the depth of the model.

(3) 3D models have been performed by varying the W_{plate} from 1000 to 3000 km wide in order to unravel if and how the width of the plates (W_{plate}) may change the deep

slab dynamics. For all cases, the box dimensions between the trench and front wall are always $\geq 0.5 W_{plate}$ to minimize border effects (e.g., *Schellart et al., 2007*).

To determine whether the trench advances or retreats with respect to the upper plate during the subduction evolution, the trench velocity is tracked ($V_t = dXt/dt$, positive if the trench advances with respect to the upper plate). The sinking velocity in the lower mantle (VsLM) is the proxy of the mantle flow behaviour. In addition, it is measured the width of the slab at the base of the upper mantle (W_{670}) mirroring the lateral variation in slab morphology (i.e., penetrating; stagnating). As far as the dynamic topographic space and time trackings are concerned, it has been used the same method as described in the equation 3.11 (Chapter 3).

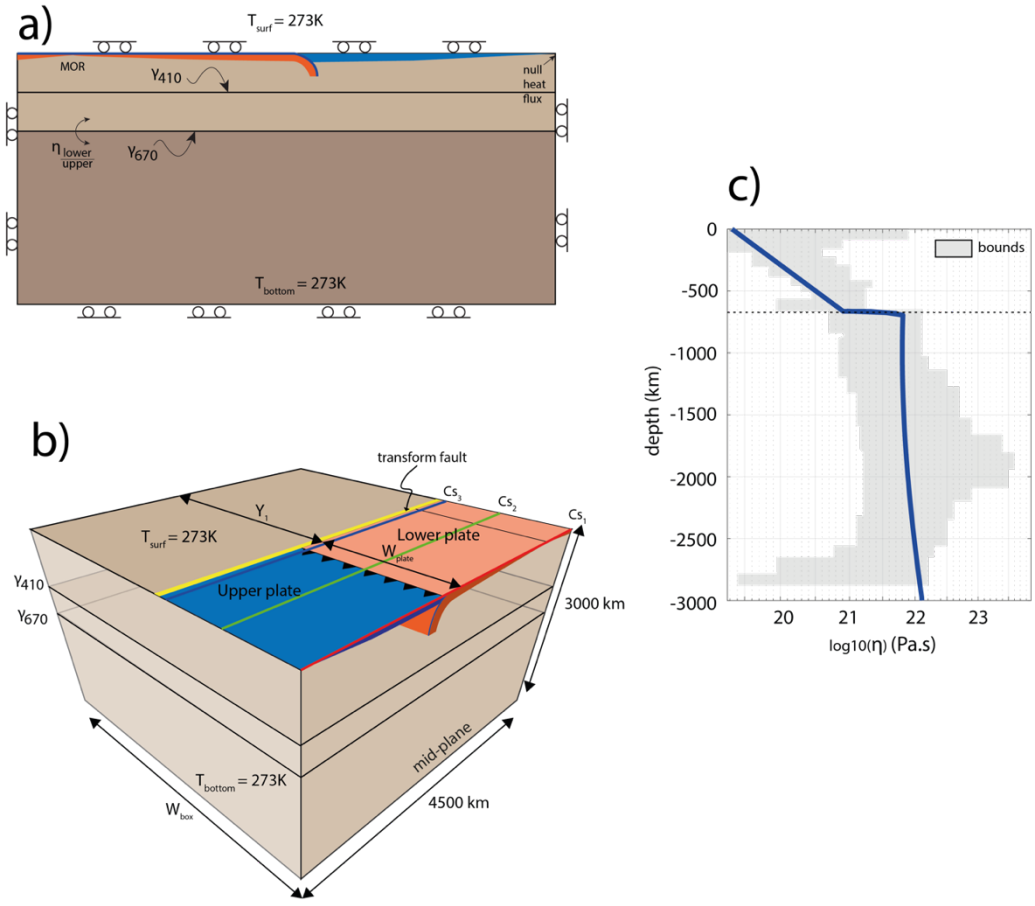

Figure 5.2: a) Initial 3D model section localised along Cs_1 (panel b) with boundary conditions. Little rollers depict the free-slip boundary. The model domain is 3000 km deep and 4500 km width. b) Initial 3D half-width model set up with thermal boundary conditions (Table1). The model domain is 3000 km deep, 4500 km width and variable in y direction (W_{box}) depending on the model set up applied. Y_1 corresponds to the free edge. Cs_1, Cs_2 and Cs_3 correspond to cross sections of 3D models presented in section 5.3. Notice that Y_2 is not mentioned due to the mid-plane set up. The lower and upper plate are in orange and blue, respectively. The upper and lower mantle are in light and dark brown, respectively. Clapeyron slopes are represented by the solid black lines (y_{410}; y_{670}). The weak viscous layer at the top of the lower plate is indicated in dark blue. c) viscosity profile used. The dotted black line separates the upper and lower mantle. Grey area represents the range of admitted viscosity based on joint inversion geoid and post-glacial rebound data from *Forte and Mitrovica (1996) and Peltier (1999)*.

5.3 Results

5 simulations of 3D self-consistent single-sided subductions have been performed with the aim to benchmark 3D and previously realized 2D models (Table 5.1). Moreover, these models enhanced to understand if and how the variability of slab morphology may induce variations in the upper plate dynamic topography.

In this section, it is first briefly introduced the 2D reference model (*mod0*) of a flattening slab at the base of the upper mantle as already described in the Chapter 3, section 3.3 of the thesis. Second, 3D models are presented (*mod1*, *mod2 and mod3*) which have the same plate and mantle rheology than the 2D reference model. Boundary condition of 3D models have been systematically modified by changing the width of free edges (i.e., Y_1; Y_2) in order to better understand how the boundary conditions may affect the slab dynamics in time. Third, it has been examined how the plate width (i.e., W_{plate}) may influence the slab morphology at depth. Fourth, the variability of dynamic topography as a function of the lateral slab length is described.

Model name	dimensions	Y_1 (km)	Y_2 (km)	W_{plate} (km)	W_{box} (km)
mod0	2D	-	-	-	-
mod1	3D	3000	-	3000	6000
mod2	3D	1500	-	3000	4500
mod3	3D	1500	1500	3000	6000
mod4	3D	3500	-	1000	4500

Table 5.1: Modelling geometrical parameters.

As already done in the chapter 3, the slab evolution has been described as happening in two distinct phases: the freely fall phase in the upper mantle (1st phase) and the slab-MTZ interaction (2nd phase).

5.3.1 Reference model: main features of flattening slab behaviour

To study the evolution of the flattening slab dynamics, it has been chosen a mantle rheology comparable to what already presented in chapter 3, section 3.4 (Table 3.2). This rheology allows the slab to stagnate at the base of the upper mantle (Fig. 5.3) thanks to a viscosity lower mantle (i.e., prefactor of $A_{lower} = 2.29x10^{15}$ Pa s) (Table 3.2; Fig. 5.3), combined to the exothermic (γ_{410} = +2.0 MPa/K) and endothermic phase transitions (γ_{670} = -2 MPa/K; Table 3.2, Fig. 5.3).

As already described for flattening slabs category in the chapter 3, I recall here the main features of the model.

The 2D slab (*mod0*) freely falls phase lasts about 5 Myr (Fig. 5.3; W_{670}). The slab sinks vertically through the upper mantle following a stationary trench motion (Fig. 5.3, V_t), while V_{sp}, decelerates from 10 to 5 cm/yr (Fig. 5.3).

The second phase is underlined by an increase of W_{670} after that the slab has reached the 670 km depth discontinuity (Fig. 5.3, W_{670}). The slab tip penetrates first into the lower mantle as illustrated by the high vertical slab sinking velocity into the lower mantle (Fig. 5.3; revealed hereafter by VsLM). Once the slab deforms and stagnates into the MTZ, the trench accelerates in combination with an increasing slab material accumulation (W_{670}) at the base of the upper mantle (Fig. 5.3). In contrast, VsLM decelerates indicating an increase of the resistance force to the slab sinking in the lower mantle.

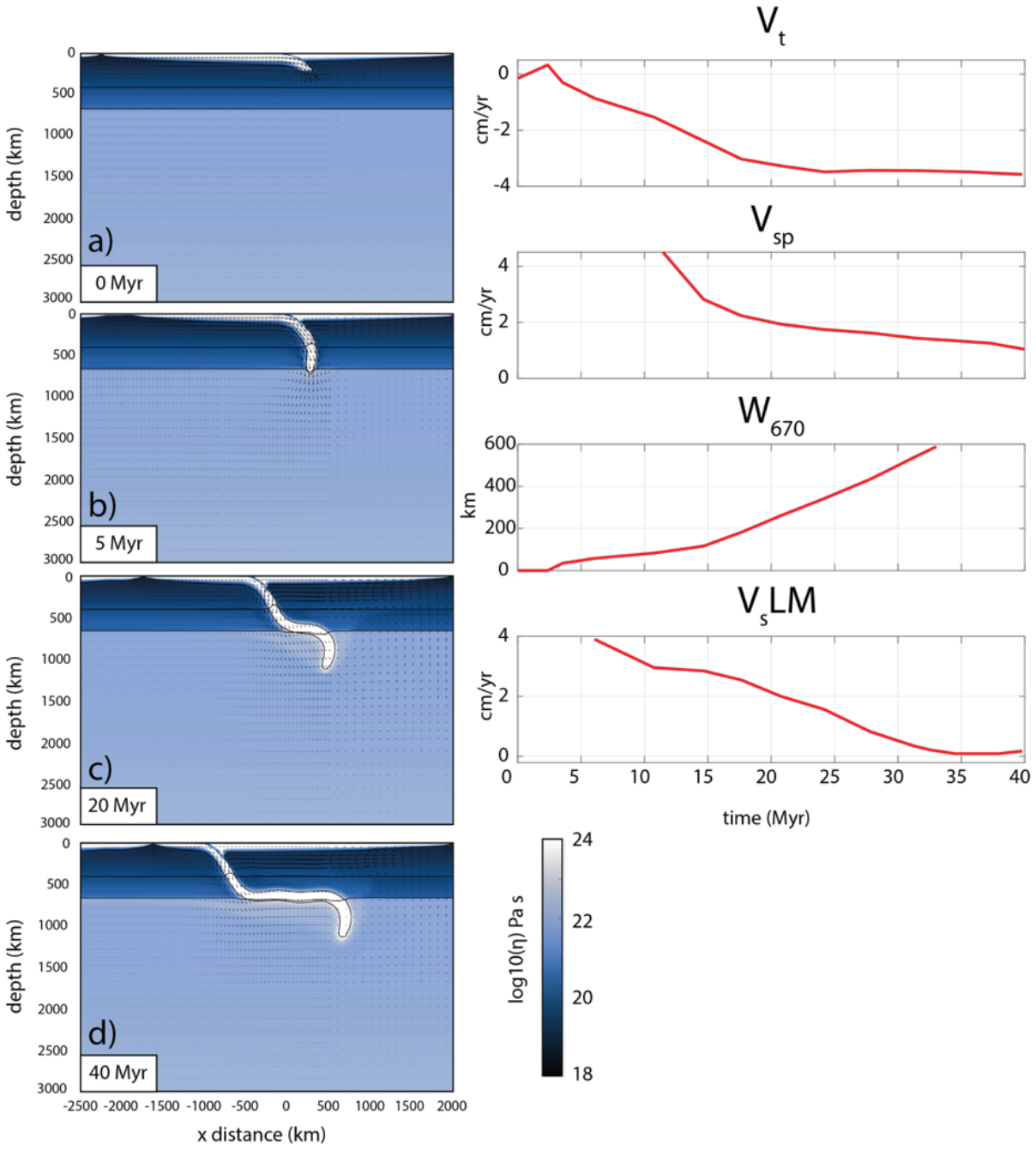

Figure 5.3: Panels a-d) 2D slab evolution in time. Background is the viscosity field. Arrows correspond to the mantle flow velocity. E) diagnostic parameters used to define the slab behaviour at depth: V_t is the trench velocity; V_{sp} the subducting plate velocity; W_{670} the slab width at the base of the upper mantle and VsLM the slab sinking velocity in the lower mantle.

5.3.2 Effect of edges boundary conditions on slab dynamics

To test how 3D slab morphology varies in space and time depending on boundary conditions and slab width, the three cross-sections has been defined, perpendicular to the trench (Fig. 5.2). Cs_1 is localized at Y=0km, Cs_2 at Y=0.5*x*W_{plate} km, and Cs_3 at Y=W_{plate} -100km, respectively (Fig. 5.4). These cross-sections are useful for processing how slab morphology, the kinematics, as well as dynamic topography, evolve laterally. Here, I present the test of how the width of the edge boundary – Y_1 - may affect the slab dynamics at depth (Table 5.1). Two 3D models have been ran changing (Y_1): *mod1* (Fig. 5.4a) is characterized by $Y_1 = h$ while model *mod2* (Fig. 5.5a) is depicted by narrower free edge boundary ($Y_1 = 0.5xh$).

For the first phase, *mod1* and *mod2* behave as described for the 2D reference model. Both 3D slabs (*mod1* and *mod2*) propagate through the upper mantle with a same morphology along the cross-sections Cs_1, Cs_2 and Cs_3 and lasting about ~5 Myr (Fig. 5.4b-d, 5.5b-d). During the second phase, *mod1* and *mod2* slabs start to buckle and roll back thanks to the resisting force to slab penetration into the lower mantle triggered by the viscous lower mantle in combination with the γ_{670} (Fig. 5.4b-d. 5.5b-d). At 20 Ma, the slab morphologies along the strike remain identical, the slabs are not affected by any 3D effect. The kinematics (V_t; VsLM) and the slab width into the MTZ (W_{670}) are comparable to what described for the reference model (Fig. 5.4e, 5.5e). The trench is stationary, VsLM decelerates whereas W_{670} starts to increase (Fig. 5.4e; 5.5e).

From 30 Ma, the slab shape of *mod1* and *mod2* does not change along the cross-sections Cs_1 and Cs_2, the slab propagates down into the lower mantle (Fig. 5.4a-c, 5.5a-c). In contrast, both *mod1* and *mod2* slabs along the Cs_3 cross-sections clearly show that the slabs start to deflect at the base of the upper mantle as highlighted by the increasing W_{670} (Fig. 5.4d, 5.5d). Moreover, there are not variations in surface kinematics along the three cross-sections (V_t). At about 35 Ma, slab geometry along cross sections differs from Cs_1 to Cs_3 for both models (*mod1* and *mod2*). We observe variations in slabs morphology from penetrating into the lower mantle (Cs_1) to stagnating into the MTZ (Cs_3). As mirrored by W_{670} and VsLM, the slab does not penetrate easily into the lower mantle for Cs_3. Cs_2 and Cs_1 depicts higher VsLM and less slab material accumulation (W_{670}) into the MTZ, suggesting a sinking slab behaviour (Fig. 5.4e, 5.5e). Both *mod1* and *mod2* show that the width of the free edge (Y_1) does not significantly affect the slab morphology.

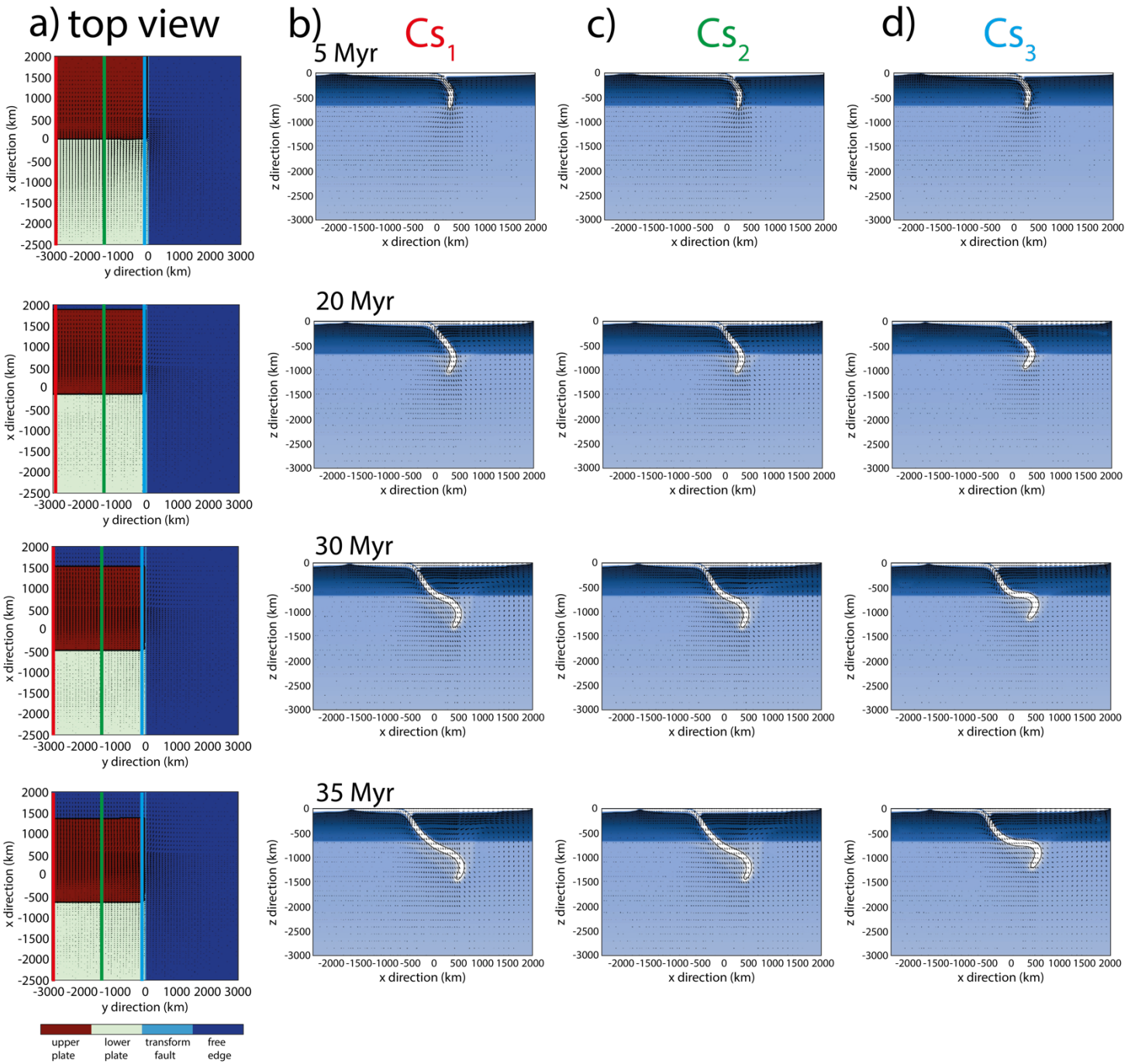

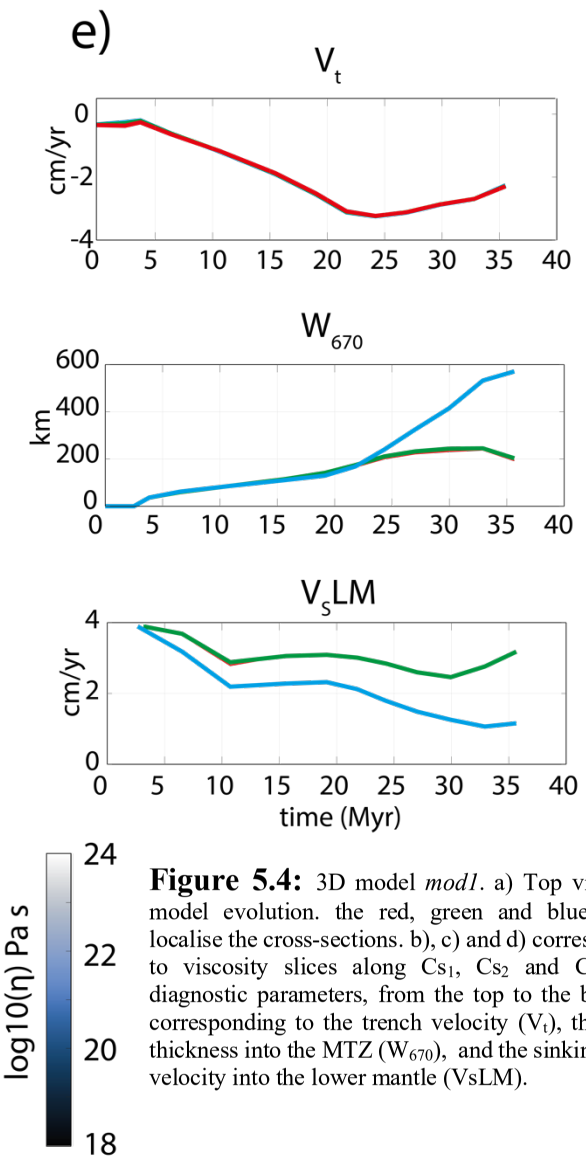

Figure 5.4: 3D model *mod1*. a) Top view of model evolution. the red, green and blue lines localise the cross-sections. b), c) and d) corresponds to viscosity slices along Cs_1, Cs_2 and Cs_3. e) diagnostic parameters, from the top to the bottom corresponding to the trench velocity (V_t), the slab thickness into the MTZ (W_{670}), and the sinking slab velocity into the lower mantle (VsLM).

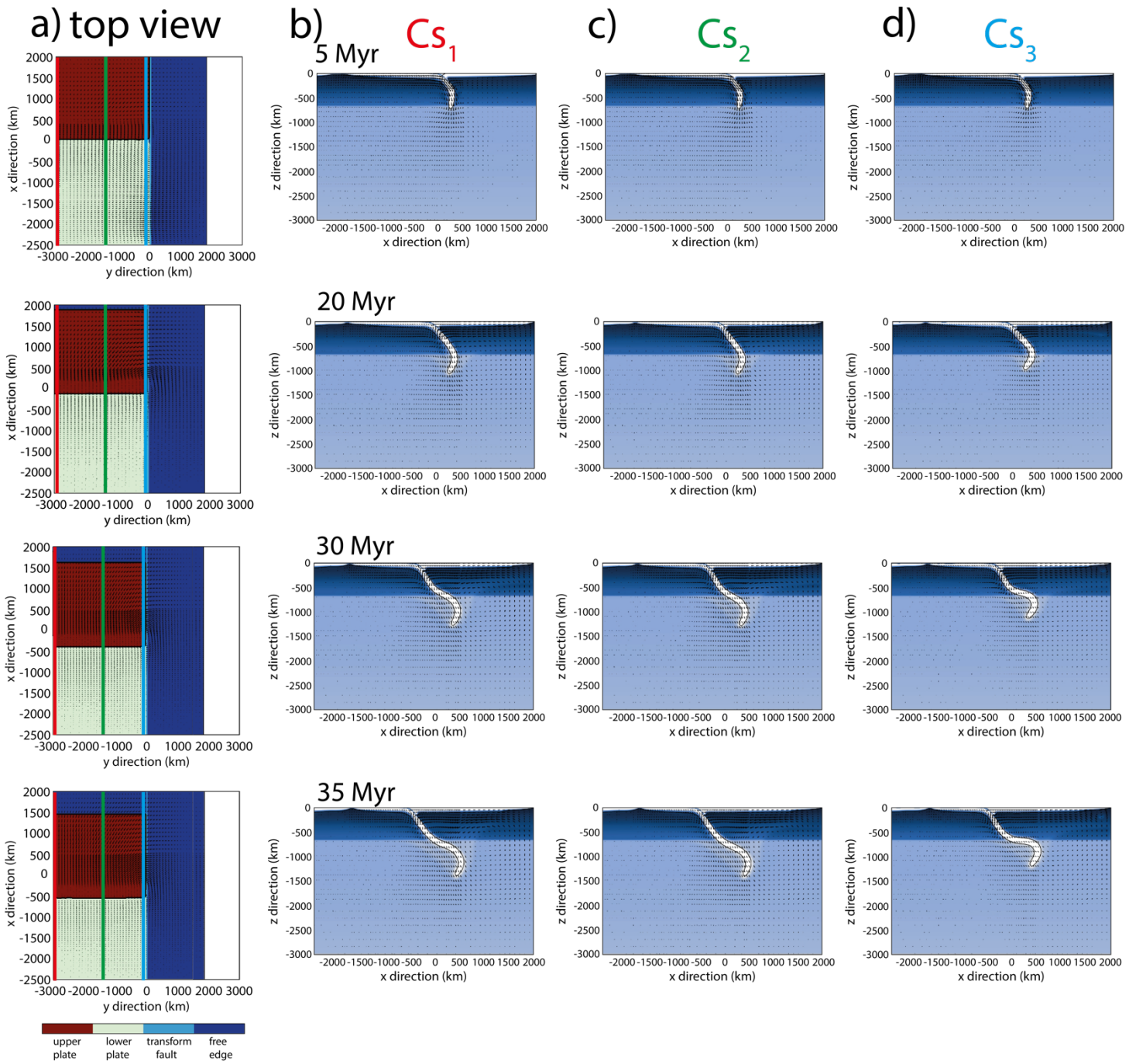

Figure 5.5: 3D model *mod2*. a) Top view of model evolution. the red, green and blue lines localise the cross-sections. . b), c) and d) corresponds to viscosity slices along Cs_1, Cs_2 and Cs_3. e) diagnostic parameters, from the top to the bottom corresponding to the trench velocity (V_t), the slab thickness into the MTZ (W_{670}), and the sinking slab velocity into the lower mantle (VsLM).

Figure 5.6 shows the vertical mantle velocity (*Vz*) along the cross-sections Cs_1, Cs_2 and Cs_3 and the horizontal velocity in x direction (*Vx*) at 300 km depth of the model *mod1*. This figure allows quantifying the resulting slab induced mantle circulation.

After 35 Myr the slab has already interacted with the lower mantle. Cs_1 and Cs_2 depict a strong *Vz* component in the whole mantle enhanced by the slab that sinks sub-vertically (Fig. 5.6 a-b). Along the cross-sections Cs_1 and Cs_2, Vz is comparable to the trench velocity, with a value of about 3 cm/yr; the size of the convection cell goes down to 2000 km depth (Fig. 5.6a-b). Below the mid-ocean ridge, on the top right end side of the model domain, the negative *Vz* velocity represents the ascending mantle flow which occurs at about 3 cm/yr (Fig. 5.6 a-c). Both positive and negative fluxes are nothing else than the expression of a well-developed poloidal flow established in the mantle along the Cs_1 and Cs_2 cross-sections (Fig. 5.6 a-b). On the contrary, Cs_3 depicts a shallower poloidal cell which goes down to 1000 km depth and is characterized by the same velocity magnitude than along Cs_1 and Cs_2 (Fig.5.6c, d). As far as the horizontal mantle circulation is concerned, *Vx* is stronger on the plate edges than on the centreline of the model (Figure. 5.6d).

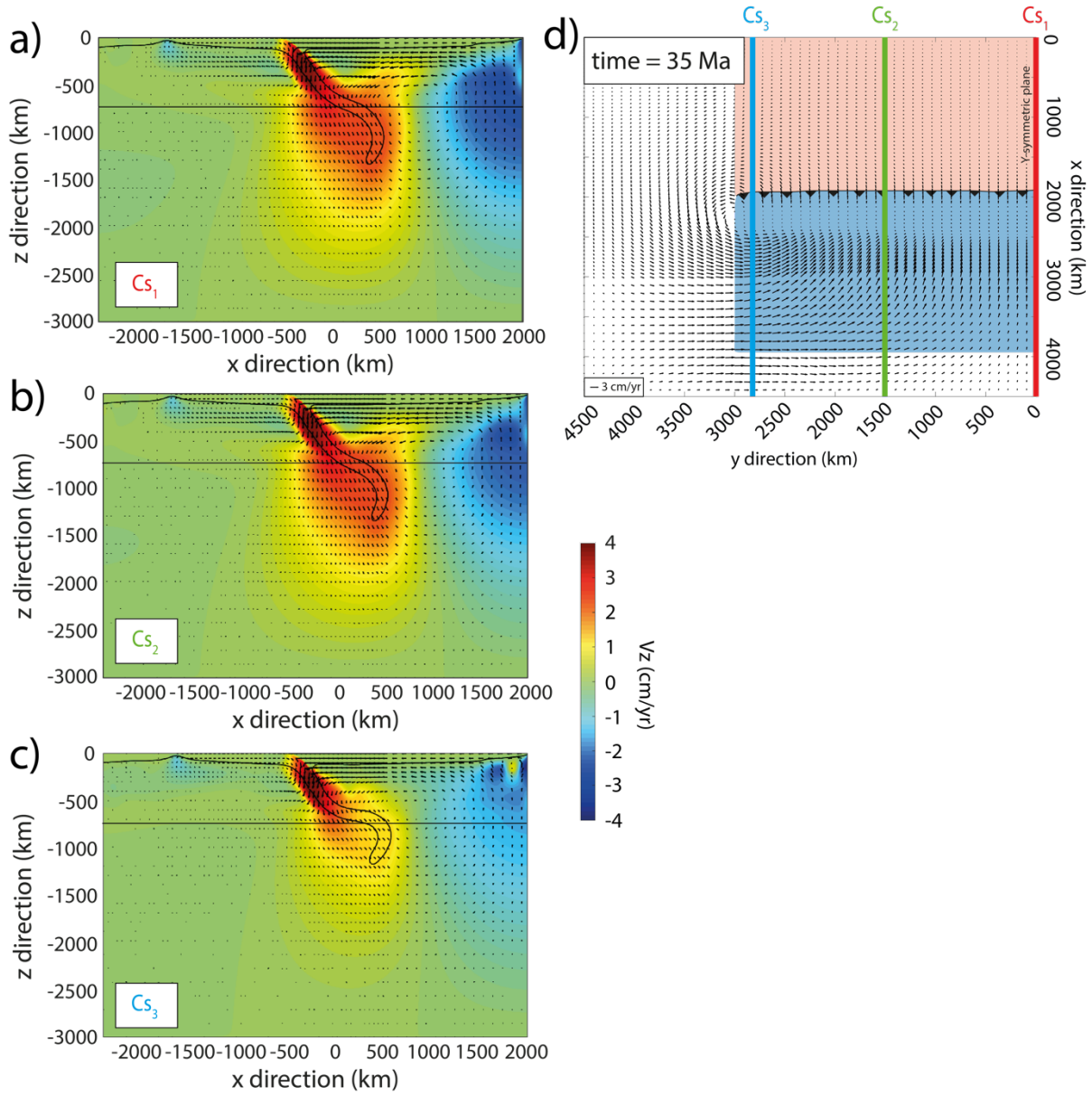

Figure 5.6*:* 3D model mod1. a-c) Vertical mantle velocities (Vz) along three cross-section of the model mod2, Cs_1, Cs_2 and Cs_3. Colours represent the V_z component of the mantle velocity flow. The slab is highlighted by the solid black contours corresponding to the isotherm 1300°C. The horizontal black solid lines are the upper/lower mantle discontinuity. d) Top view of the model domain. Orange and blue colours show the lower and upper plates, respectively. Arrows correspond to the horizontal mantle velocity flow at 300 km depth. The blue, green and red lines correspond to the cross-section Cs_1, Cs_2 and Cs_3, respectively.

To test if the lateral variation in slab morphology - from the free edges where slab stagnates to the centreline where slab moves down into the lower mantle – is caused only by the peculiar mid-plane model set up, I ran the model *Mod3.* This model differs from the two previous ones by adding another free edge boundary, Y_2. The two free edges, Y_1 and Y_2, are settled on both sides of the subducting system (Fig. 5.5). *Mod3* is thus characterized by $Y_1 = Y_2 = 0.5xh$ (Table 5.1) while the whole mantle and plate settings are not changed. In order to avoid possible misunderstandings related to the presence of the two free-edges, the cross-section names have been slightly changed (i.e., Cs_1 become Cs_3').

During the first phase, which lasts 5 Myr, the slab behaves as described for the two previous cases (Fig. 5.4, 5.5). The slab moves through the upper mantle assuming the same morphology along the cross-sections Cs_3, Cs_2 and Cs_3' (Fig.5.7a) than models *mod1* and *mod2* (Fig. 5.4, 5.5).

During the second phase, lasting up to 20 Ma, the slab starts to buckle and roll back (Fig. 5.7b-d). This is due to the resisting force to slab penetration into the lower mantle triggered by both the viscous lower mantle and the γ_{670}. However, VsLM is higher for Cs_2 than Cs_3 and Cs_3' (Fig. 5.7b, d).

From 30 Ma to the end of the simulation, the slab geometry differs along the three selected cross sections. We observe variations in slab morphology from penetrating into the lower mantle (Cs_2) to stagnating in the MTZ (Cs_3, Cs_3'). W_{670} and V_sLM are significant on the plate edges (Cs_3 and Cs_3'). On the contrary, the model shows faster V_sLM and less slab material (W_{670}) into the MTZ in its central part (Cs_2). These parameters indicate that slab penetrates into the lower mantle but only in the middle of the model (Fig.5.7).

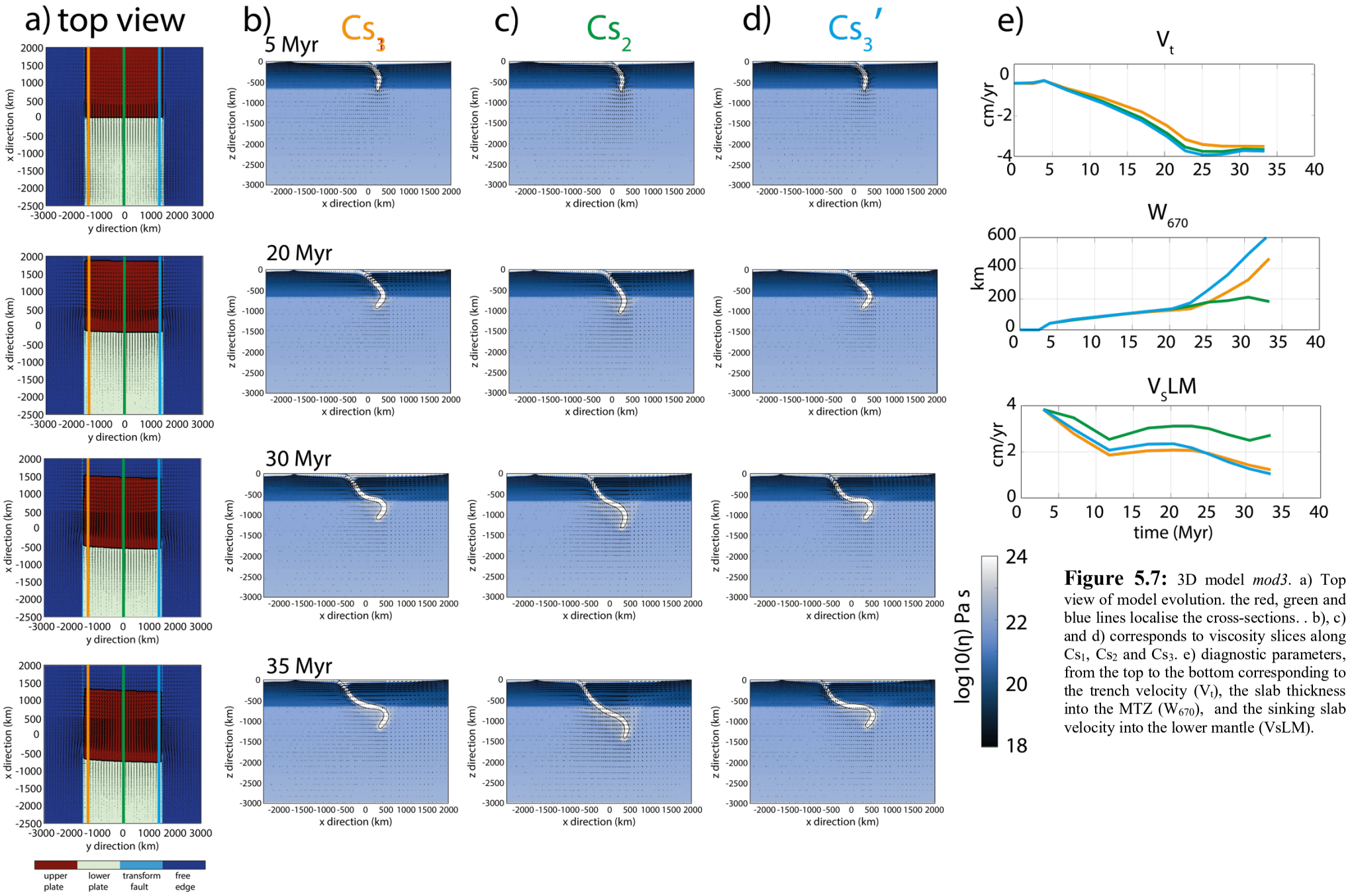

Figure 5.7: 3D model *mod3*. a) Top view of model evolution. the red, green and blue lines localise the cross-sections. . b), c) and d) corresponds to viscosity slices along Cs_1, Cs_2 and Cs_3. e) diagnostic parameters, from the top to the bottom corresponding to the trench velocity (V_t), the slab thickness into the MTZ (W_{670}), and the sinking slab velocity into the lower mantle (VsLM).

5.3.3 How does plate width affect the slab morphology?

To decipher if the slab width (W_{plate}) has an impact on the slab behaviour at depth, the model *mod4* has been ran. The plate width (W_{plate}) has been decreased to W_{plate} = 1000km, keeping constant the other parameters (Table 5.1).

During the first phase, the slab behaves as described in the previous cases (Fig. 5.4 to 5.7). The slab propagates through the upper mantle in about 5 Myr, having the same morphology along Cs_1, Cs_2 and Cs_3 (Fig. 5.8b-d).

During the 2nd phase, the slab geometries are identical along the cross-sections Cs_1, Cs_2 and Cs_3: the slab goes down into the lower mantle without showing lateral variation of slab morphology in time. This uniform slab morphology is mirrored by the same, linear increase of both W_{670} and the sinking velocity in the lower mantle (Fig. 5.8e). In addition, we do not see variations in the trench kinematics (V_t; Fig. 5.8e).

Figure 5.9 shows the vertical component of the slab induced mantle velocity (*Vz*) along the cross-sections Cs_1, Cs_2 and Cs_3 and the horizontal velocity in x the direction (*Vx*) at 300 km depth, as previously described in the figure 5.6. A pronounced downward *Vz* reaches 2000 km and surrounds the slab, in the three cross-sections Cs_1, Cs_2 and Cs_3 (Fig. 5.9 a-c), *Vz* has an average velocity of about 3 cm/yr (Fig. 5.9a-c). Once again, *Vz* indicates a well-developed poloidal flow settled below the plates from side to side of the plate (Fig. 5.9a-b). The horizontal component of the slab induced mantle velocity (V_X) shows a strong toroidal component acting from the edge to the mid-plane of the narrow subduction system and characterized by a dimension cell of about 2500 km (Fig. 5.9d).

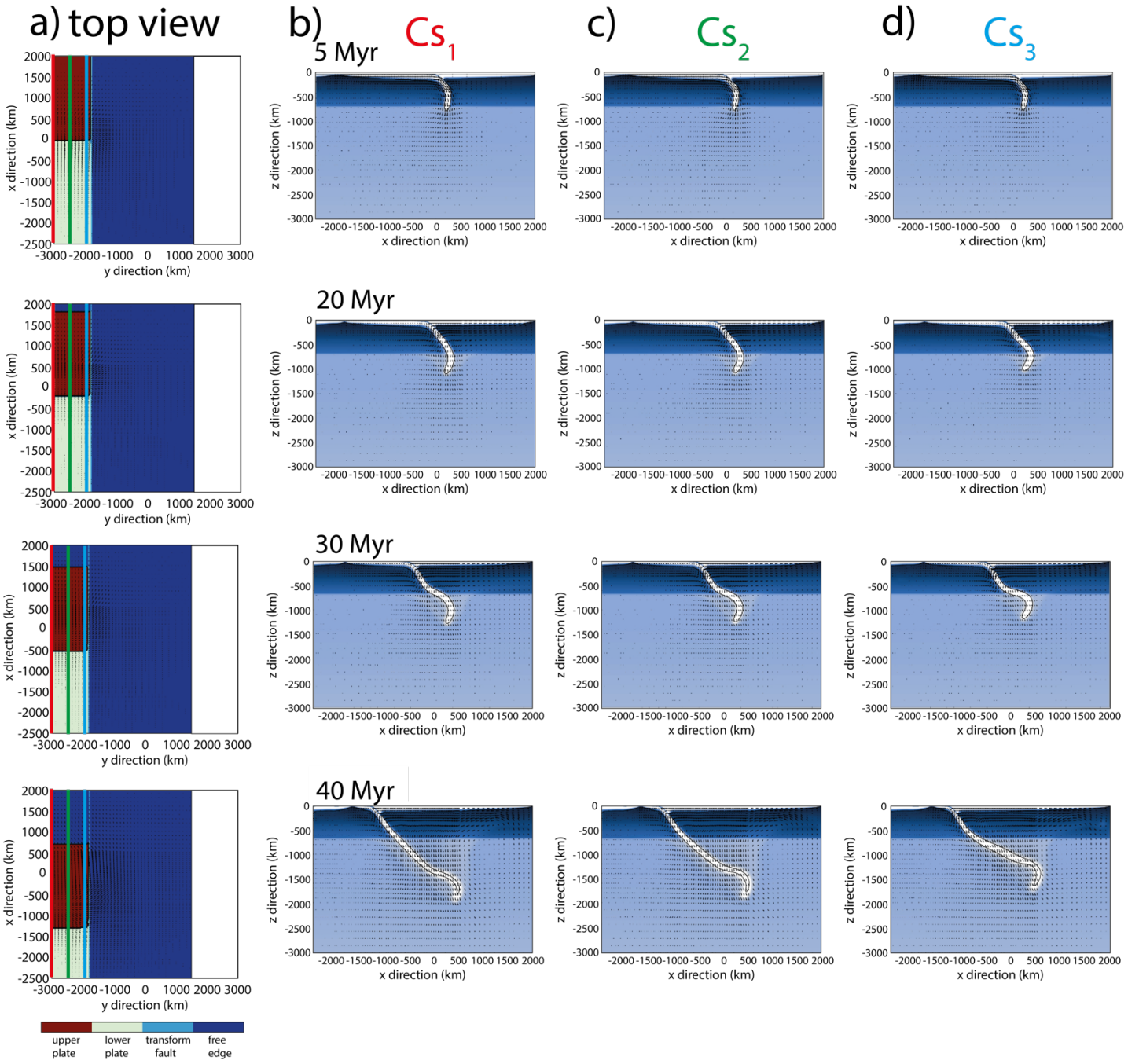

Figure 5.8: 3D model *mod4* a) Top view of model evolution. the red, green and blue lines localise the cross-sections. b), c) and d) corresponds to viscosity slices along Cs_1, Cs_2 and Cs_3. e) diagnostic parameters, from the top to the bottom corresponding to the trench velocity (V_t), the slab thickness into the MTZ (W_{670}), and the sinking slab velocity into the lower mantle (VsLM).

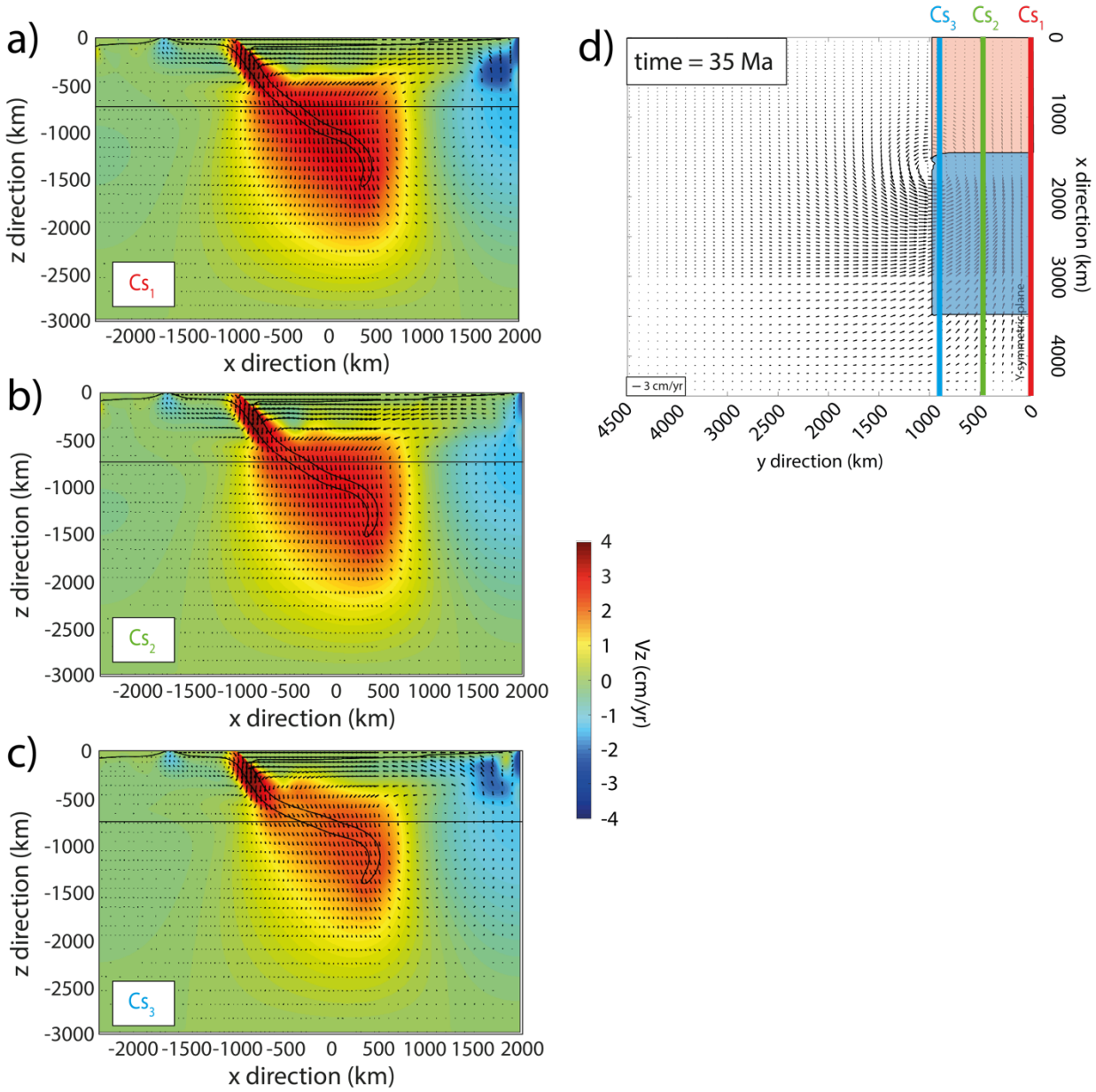

Figure 5.9: 3D model mod4.a-c) depict the vertical velocities of the three cross-section Cs_1, Cs_2 and Cs_3 of the model mod4. Colours represent the V_z component of the slab induced mantle velocity flow. The slab is highlighted by a solid black contour corresponding to the isotherm 1300°C. The black solid line is the upper/lower mantle discontinuity. d) top view of the model domain. Orange and blue colours show the lower and upper plat, respectively. Arrows correspond to the horizontal mantle velocity flow at 300 km depth. The blue, green and red lines correspond to the cross-sections Cs_1, Cs_2 and Cs_3, respectively.

5.4 Discussion and perspective

In the Chapter 3 of this thesis, the 2D numerical models of the flattening slabs show how the dynamic topography evolve once the slab interacts with the 670 km depth discontinuity. It has been found that this process brings to the tilt of the upper plate towards the trench as well as to an average dynamic topography of the upper plate decrease. However, the 2D approximation would make the results applicable only to a very limited selection of subduction zones. Hence, the use of 3D modelling is an important step forward to better understand not only how the slab evolves laterally during its evolution but also if and how it is possible to detect the surface fingerprints of such slab variation at depth.

5.4.1 Effects boundary conditions on slab dynamics

As seen from figures 5.4 to 5.7, the boundary conditions of the system (i.e., Y_1) do not impact the overall slab and mantle dynamics evolution in time. Thanks to the edge boundaries tests (see section 5.3.2), it has been showed that the free edge (i.e., Y_1) boundary must be $\geq 0.5xh$ to minimize the weird influence of the box sidewalls. M*od2* has been setup large enough such that no appreciable amount of deformation occurs on Y_1. In case of presence of two free edges on both sides of the subduction zone (Fig.5.7, Y_1 and Y_2), the slab lateral evolution in time is still unchanged from the centre to the free edge of the plates (Y_1). As showed by the models with the mid-plane set up (*mod1* and *mod2*) and the free edges (Y_1 and Y_2; *mod3*), there is slab stagnation close to the plate edges whereas slab penetration occurs far from the plate edges.

The model *mod3* with free edges looks similar to what found in the models with mid-plane (*mod1*, *mod2*): the centre of *mod3* remains similar to the centreline of *mod1* and *mod2,* showing slab penetration into the lower mantle (Fig.5.4, 5.5, 5.7). The central (or the side-wall) part of the 3D models suggests that the poloidal component of the slab/mantle flow enhances the slab penetration into the lower mantle (Fig.5.10). In contrast, the free edges remain identical in term of slab morphology and mantle flow dynamics: the toroidal flow sustains the slab deflection into the MTZ. This outcome confirms that the free edges or mid-plane boundaries conditions do not strongly influence the 3D subduction dynamics.

5.4.2 Effects of plate width of slab dynamics

Comparing the outcomes of the wide (Fig. 5.4, 5.5, 5.7) and narrow subduction systems (Fig. 5.8), it is clear that the subducting plate width (W_{plate}) tune the way the slab deforms at depth. The lateral morphological variations are associated with variable the slab velocity (VsLM), slab width (W_{670}) and shape/velocity of the slab induced mantle circulation cells (Fig.5.8, 5.9). Wide subduction zones (*mod1* to *mod3*) show that the slab either sinks at a low angle through the upper mantle and flattens into the MTZ on subduction edges (Fig. 5.7e, Cs_3; Cs_3'), or it sinks at a steep angle into the lower mantle in the centre of the 3D models (Fig. 5.7e, Cs_1). In contrast, narrow subduction zone shows the slab sinks at steep angle without significant trench-parallel variation in morphology (Fig 5.8b, Cs_1, Cs_2, Cs_3).

This peculiar setting triggers a slightly different slab induced mantle circulation as respect to what shown in the previous case: in the centre of large subducting system, the poloidal mantle flow dominates. In contrast, the free edges allow for strong toroidal mantle flow around the slab which, in turn, favours the slab deflection at the base of the upper mantle. Hence, the subduction dynamics and the lateral slab morphology is significantly controlled by W_{plate}.

This outcome is in agreement with *Schellart et al.* (2007), where wide subduction zone makes changes in the slab dip angle in combination with upper plates bending. *Schellart et al.* (2007) have found that a wide subduction system (W_{plate}>2000 km) is characterized by the minimum and the maximum in trench velocity in the centre of the model and close to each slab edge, respectively. This peculiar condition leads to more slab stagnation on the 670 km discontinuity close in correspondence of the slab edges. In contrast, narrow subduction zones homogeneously retreat along the trench strike (*Schellart et al., 2007*).

However, models presented in this chapter, assume strong lithospheres (i.e., maximum viscosity cut-off). Thus, the upper plates are not able to strongly deform and bend inducing a significant curvature of the trench and tuning the trench velocity rate along the strike. Furthermore, the plate strength may have an impact on how the slab deform laterally at depth. Indeed, by reducing the maximum viscosity-cut off of the current 3D models, the trench as well as the slab at depth might be more prone to curve and deform which, in turn, may enhance the lateral variability of slab geometry. Hence, to improve how the slab and lithosphere may curve

during the subduction evolution, future implementations (e.g., more complex lithosphere and slab rheology, lateral heterogeneities in the upper and lower plates) are mandatory.

5.4.3 Dynamic topography response to lateral slab morphology at depth

In agreement with the previous findings of *Crameri and Lithgow-Bertelloni* (2017), 2D numerical models realized in the frame of this thesis have shown that the upper plate topography tilts towards the trench when the slab starts to interact with the MTZ. The presence of a viscosity jump between the upper and lower mantle and the 670 km depth phase transition have been invocated as the main engines able to generate a trench-ward upper plate tilting.

It is shown here that a tilt of the upper plate towards the trench occurs also for wide 3D models, as soon as the slab hits the MTZ (Fig. 5.10d). In our wide plate cases, the trench perpendicular tilting of the upper plate occurs at about 2000 km from the plates edges (Fig.5.10 d; *mod1*, *mod2* and *mod3*). On the contrary, there is no tilt of the narrow upper plate towards the trench on the plate edge (Fig.5.10d-e*; mod4*). Narrow subduction zone neither depicts the tilt of the upper plate toward the trench in the centreline nor in the plate edge (Fig.5.10a-b).

The novel finding of this study is the differential occurrence of dynamic tilting (comparable to the width of the plate) of the upper plate in wide subduction zones (W_{plate}=3000km; Fig. 5.4, 5.5, 5.7). This tilting occurs from the plate edges towards the centreline of the models (*mod1*/*mod* 2 and in *mod3*; Fig. 5.10). The tilting of the upper plate toward the centreline is about 0.002° and up to 0.01° over a distance of 3000 km and over a time period of around ~35 Ma (Fig. 5.10d). In contrast, narrow subduction system clearly shows that the tilt towards the centreline of the system does not occur while the slab propagates directly into the lower mantle. This peculiar dynamic topographic behaviour may be explained as the consequence of the slab induced mantle circulation occurring once the slab starts to interact with the MTZ. Indeed, once the wide slab reaches the upper/lower discontinuity in the middle of subduction system (or close to the centreline), it starts to excite a much larger poloidal flow. The poloidal flow acts on the dynamic topography by pulling down the upper plate trench-wards. As result, the dynamic topography shows significant tilting of the upper plate towards the trench during slab/lower mantle interactions (Fig. 5.10d). The wide plate edges cases show the poloidal mantle flow cell hampered by the toroidal flow enhanced by the lack of slab material on the free edge (e.g., *Funiciello et al., 2003*). Here, the mantle flow cell becomes

progressively localised into the upper mantle which, in turn, dampers the dynamic topography tilting parallel to the trench (Fig. 5.10d). The narrow slab width case shows the toroidal mantle cell affecting the entire subduction domain. Thus, the dynamic topography is also dampened by the toroidal flow, as mirrored by the flat signal recorded along Cs_1, Cs_2 and Cs_3.

In this study, I assume the same viscosity profile for all the models. By reducing the upper mantle viscosity, the mantle flow should be more vigorous. Hence, a weaker mantle viscosity should produce bigger toroidal convection cells. Consequently, the width of the plate should play a second order role in driving the lateral variability of slab morphology than the mantle rheology. Indeed, I would expect that the slab stagnation dominates far from the plate edge with weaker upper mantle viscosity. Hence, the dynamic topography profile of the upper plate may be more flattened inland ward, with less dynamic tilting in the mid-plane or in the centre of the 3D model. It could be interesting to investigate how the 3D slab lateral variability evolves in time analysing the parameter space of the Earth viscosity profile. This work deserves future investigations.

Furthermore, a previous study (*Crameri and Lightgow-Bertelloni, 2017*) found that the continental upper may be correlated to progressive marine flooding event. However, I investigated how the dynamic topography of the upper plate varies exclusively for the underlying mantle dynamics. Thus, the models presented in this thesis suppressed the isostasy part of the full topography. Hence, the upper plate inundation is not appreciable.

There are natural examples of continental tilting inferred from the geologic record. For example, there is a tilt of the central North American in the Late Cretaceous producing large scale flooding (*Mitrovica et al., 1989*) probably induced by penetration of the Farallon slab into the lower mantle (*Davila and Lithgow-Bertelloni, 2015*; *Gurnis,* 1990; *Gurnis et al.,* 2000; *Liu et al.,* 2008; *Mitrovica et al.,* 1996). A similar tilting has been attributed to the subduction in Australia towards the South-East Asian subduction system, which experienced a tilt of ~0.08° during the Eocene (DiCaprio et al., 2009; Heine et al., 2010, Crameri and Lithgow-Bertelloni, 2017). Additionally, the subduction-induced large-scale mantle-flow cell has already been evocated as possible cause of compression and mountain building in the upper plate, in the region closer to the trench (*Crameri et al., 2017; Crameri et Lithgow-Bertelloni, 2017; Faccenna et al., 2013, 2017*). Even though those examples still have to be investigated carefully, the lateral variability of slab morphology-induced mantle flow may explain variation in the large-scale upper plate dynamic topography.

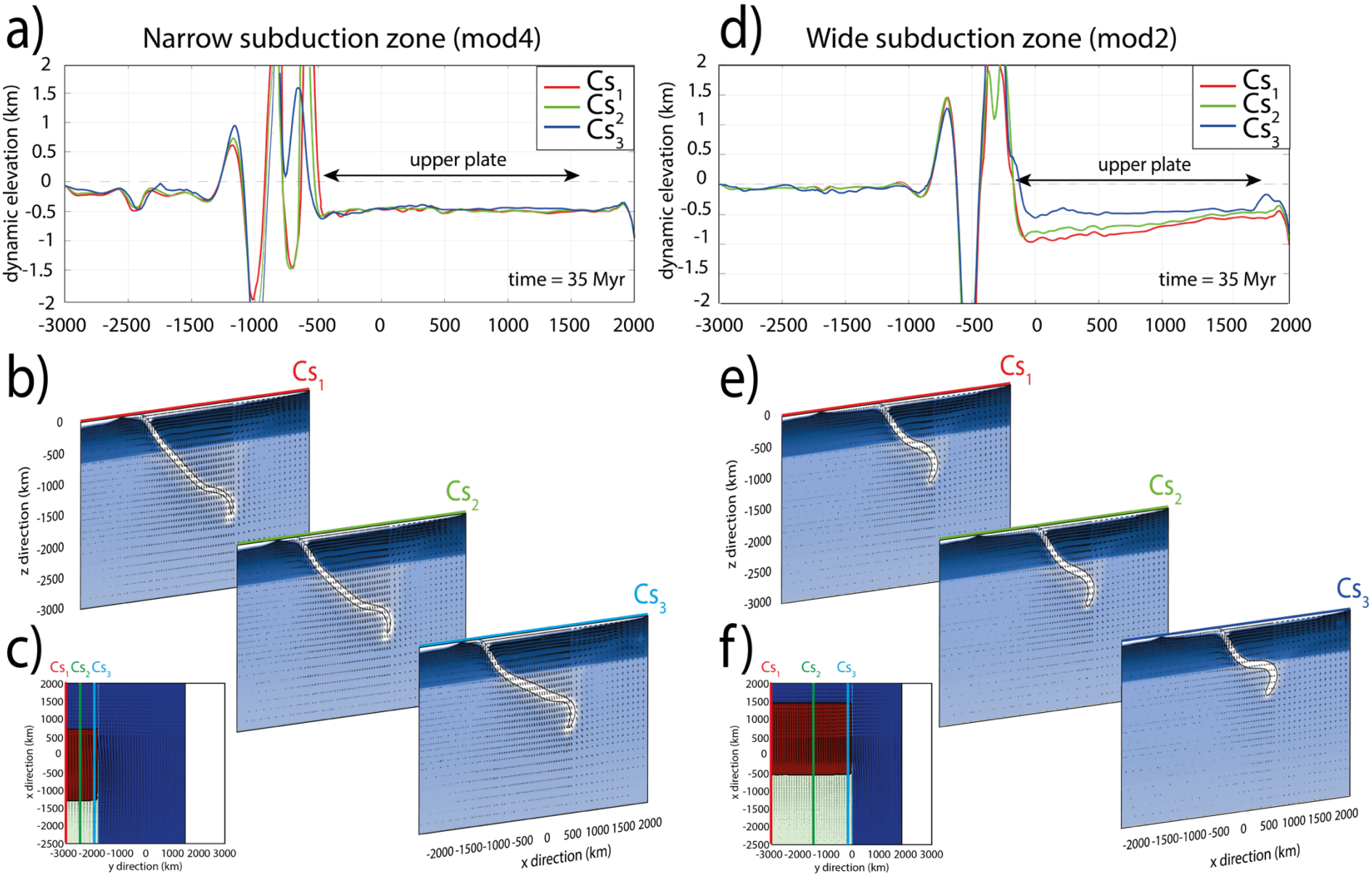

Figure 5.10: a) and b) are the dynamic topography profiles along the cross-section Cs1 (red), Cs2 (green) and Cs3 (blue). b) c) e) and f) illustrate the last stages of models mod4 and mod3, respectively.

Chapter VI

Conclusions

This thesis is focused on analysing if and how the surface fingerprints of the upper plate are affected by the deep slab dynamics, especially once slabs starts to interact with the upper-lower mantle transition zone.

Thanks to 2D numerical models, I systematically investigated the role of the mantle rheology (i.e., Clapeyron slopes and lower mantle viscosity) as well as plate strength (i.e., initial thermal age of plates) on the slab dynamics and the resulting surface fingerprints. Numerical self-consistent thermo-mechanical subduction models showed that - within a plausible range of the Clapeyron slopes, mantle viscosity contrasts and ages of subducting plates - there are many cases where the upper plate topography is strongly affected by the underlying slab dynamics. When the slab sinks straight into the deep mantle, it enhances a quasi-stationary trench kinematics and a flat, large-scale topographic signal of the upper plate over time.

The coexistence of a strong post-spinel transition (<-2 MPa/K) Clapeyron slope combined with a viscous lower mantle ($\geq 1.2 \times 10^{22}$ Pa s) hampers, at least temporarily, slab penetration into the lower mantle and induces slabs to lay down horizontally on the MTZ. This peculiar condition kinematically enhances trench retreat and the development of a wide convection cell beneath the upper plate which induces a large-scale upper plate dynamic topography subsidence and a tilting of the upper plate towards the trench.

Slab folding and buckling are typical for strong Clapeyron slopes at both 410 km and 670 km depths; these systems are characterized by cyclic episodes of trenches retreat and advance. This specific kinematics leads to cyclic changes of the slab induced mantle circulation below the upper plate and induces episodic variations of dynamic topography, by pulling up and down the upper plate. Moreover, the surface topography of the upper plate tilts toward and fromward the trench, following the slab folding at depth.

The outcomes of 2D numerical models have been exported to the analysis of the Neotethys subduction system, in particular in the Iranian area from ~100 Ma to 30 Ma. Thanks to a joined numerical and natural data approach, the history of the Neotethys subduction system has been deciphered. It has been explored how the slab dynamics may affect the surface deformation of the western Cimmerian domain since Mid Cretaceous. With the compilation of natural data, plate kinematic reconstructions, numerical modelling and tomographic images, it has been showed that the folding slab behaviour into the mantle transition zone had a profound impact on the structural evolution of the western Cimmerian domain. It has been unravelled that the

folding slab behaviour at the mantle transition zone discontinuity led to episodic trench migration, large-scale topographic variations and deformations of the upper plate. In Iran, the Neotethys ocean subducted below the western Cimmerian domain before the onset of the collision between Arabian and Eurasia. The trench motion and the upper plate deformation have been estimated: the opening of the Nain-Baft and Sabzevar-Sistan back-arc basins during middle to Late Cretaceous is likely related to the roll back of the Neotethys slab. The basin closure during Paleogene could have been triggered by the folding of the slab towards the upper plate. The extension and marine flooding of the upper plate during Eocene is related to the roll back of the slab. Since the onset of the Arabian Eurasia collision, the trench has advanced inducing the convex shape of the Neotethys slab. At early Miocene, the onset of the slab avalanche into the lower mantle induces widespread marine flooding on the upper plate.

Finally, I performed 3D numerical models of subduction with the aim to understand if and how the behaviour of the slab at depth and, in turn, the associated shallow fingerprints, are influenced by the width of the subducting plate. These models demonstrated that the width of the subduction system plays a significant role. A wide subduction zone is characterized by a slab which propagates down into the lower mantle in its centre while the slab stagnates on the 670 km discontinuity along the plate edges. On the contrary, a narrow subduction system did not depict such lateral variation in slab morphology once interacting with the mantle transition zone. The characteristic poloidal and toroidal mantle circulation induced by the subduction process acts below the upper plate; it has been recognized as the main driver of the dynamic topography gradient from the centre to the plate edge for wide 3D cases.

The toroidal mantle circulation hampers the upper plate tilting of the plate edges towards the trench. On the contrary, the poloidal mantle flow cell triggers the tilt of the whole upper plate towards the trench. The trench perpendicular tilting of the upper plate might coincide with an increase in upper plate inundation even far from the subduction edges.

References

Agard, P., Omrani, J., Jolivet, L., & Mouthereau, F. (2005). Convergence history across Zagros (Iran): constraints from collisional and earlier deformation. *Internal Journal of Earth Sciences*, *94*, 401–419. https://doi.org/10.1007/s00531-005-0481-4

Agard, P., Monié, P., Gerber, W., Omrani, J., Molinaro, M., Meyer, B., et al. (2006). Transient, synobduction exhumation of Zagros blueschists inferred from P-T, deformation, time, and kinematic constraints: Implications for Neotethyan wedge dynamics. *Journal of Geophysical Research: Solid Earth*, *111*(11). https://doi.org/10.1029/2005JB004103

Agard, P., Omrani, J., Jolivet, L., Whitechurch, H., Spakman, W., Monié, P., et al. (2011). Zagros orogeny : a subduction-dominated process. *Geological Magazine*, *148*(5–6), 692–725. https://doi.org/10.1017/S001675681100046X

Aghanabati, A., & Rezai, A. (2009). *Correlation of lithostratigraphic units ofIran in major structural and sedimentary basins.*

Agrusta, R., Van Hunen, J., & Goes, S. (2014). The effect of metastable pyroxene on the slab dynamics. *Geophysical Research Letters*, *41*(24), 8800–8808. https://doi.org/10.1002/2014GL062159

Agrusta, R., Goes, S., & van Hunen, J. (2017). Subducting-slab transition-zone interaction: Stagnation, penetration and mode switches. *Earth and Planetary Science Letters*, *464*, 10–23. https://doi.org/10.1016/j.epsl.2017.02.005

and Planetary Science Letters, *464*, 10–23. https://doi.org/10.1016/j.epsl.2017.02.005

Agrusta, R., van Hunen, J., & Goes, S. (2018). Strong plates enhance mantle mixing in early Earth. *Nature Communications*, *9*(1), 2708. https://doi.org/10.1038/s41467-018-05194-5

Alamdarie Malekpour, A. (2017). *Regional Tectonic and Structural Significance of Late Cretaceous-Cenozoic Extension in Iran*. New Mexico Institute of Mining and Technology.

Ali, S. A., Buckman, S., Aswad, K. J., Jones, B. G., Ismail, S. A., & Nutman, A. P. (2012). Recognition of Late Cretaceous Hasanbag ophiolite-arc rocks in the Kurdistan Region of the Iraqi Zagros suture zone: A missing link in the paleogeography of the closing Neotethys Ocean. *Lithosphere*, *4*(5), 395–410.

Allahyari, K., Saccani, E., Rahimzadeh, B., & Zeda, O. (2014). Mineral chemistry and petrology of highly magnesian ultramafic cumulates from the Sarve-Abad (Sawlava) ophiolites (Kurdistan, NW Iran): New evidence for boninitic magmatism in intra-oceanic fore-arc setting in the Neo-Tethys between Arabia and Iran. *Journal of Asian Earth*

Sciences, *79*, 312–328.

Allen, M. B. (2010). Roles of strike-slip faults during continental deformation: examples from the active Arabia–Eurasia collision. *Geological Society, London, Special Publications*, *338*(1), 329–344. https://doi.org/10.1144/SP338.15

Allen, M. B., & Armstrong, H. A. (2008). Arabia-Eurasia collision and the forcing of mid-Cenozoic global cooling. *Palaeogeography, Palaeoclimatology, Palaeoecology*, *265*(1–2), 52–58. https://doi.org/10.1016/j.palaeo.2008.04.021

Allen, M. B., Vincent, S. J., Alsop, G. I., Ismail-Zadeh, A., & Flecker, R. (2003). Late Cenozoic deformation in the South Caspian region: Effects of a rigid basement block within a collision zone. *Tectonophysics*, *366*(3–4), 223–239. https://doi.org/10.1016/S0040-1951(03)00098-2

Ao, S., Xiao, W., Khalatbari Jafari, M., Talebian, M., Chen, L., Wan, B., et al. (2016). U-Pb zircon ages, field geology and geochemistry of the Kermanshah ophiolite (Iran): From continental rifting at 79 Ma to oceanic core complex at ca. 36 Ma in the southern Neo-Tethys. *Gondwana Research*, *31*, 305–318. https://doi.org/10.1016/j.gr.2015.01.014

Arnould, M., Coltice, N., Flament, N., Seigneur, V., & Müller, R. D. (2018). On the Scales of Dynamic Topography in Whole-Mantle Convection Models. *Geochemistry, Geophysics, Geosystems*, *0*(0). https://doi.org/10.1029/2018GC007516

Aswad, K. J. A., Aziz, N. R. H., & Koyi, H. A. (2011). Cr-spinel compositions in serpentinites and their implications for the petrotectonic history of the Zagros Suture Zone, Kurdistan Region, Iraq. *Geological Magazine*, *148*(5–6), 802–818.

Authemayou, C., Chardon, D., Bellier, O., Malekzadeh, Z., Shabanian, E., & Abbassi, M. R. (2006). Late Cenozoic partitioning of oblique plate convergence in the Zagros fold-and-thrust belt (Iran). *Tectonics*, *25*(3), 1–21. https://doi.org/10.1029/2005TC001860

Azizi, H., & Jahangiri, A. (2008). Cretaceous subduction-related volcanism in the northern Sanandaj-Sirjan Zone, Iran. *Journal of Geodynamics*, *45*(4–5), 178–190. https://doi.org/10.1016/j.jog.2007.11.001

Azizi, H., Hadad, S., Stern, R. J., & Asahara, Y. (2018). Age, geochemistry, and emplacement of the ~40-Ma Baneh granite–appinite complex in a transpressional tectonic regime, Zagros suture zone, northwest Iran. *International Geology Review*, *00*(00), 1–29. https://doi.org/10.1080/00206814.2017.1422394

Babaie, H. A., Babaei, A., Ghazi, A. M., & Arvin, M. (2006). Geochemical, 40Ar/39Ar age, and isotopic data for crustal rocks of the Neyriz ophiolite, Iran. *Canadian Journal of Earth Sciences*, *43*(1), 57–70.

Babazadeh, S. A., & de Wever, P. (2004). Early Cretaceous radiolarian assemblages from radiolarites in the Sistan Suture (eastern Iran). *Geodiversitas*, *26*(2), 185–206.

Badr, M. J., Collins, A. S., & Masoudi, F. (2013). The U-Pb age, geochemistry and tectonic significance of granitoids in the Soursat Complex, Northwest Iran. *Turkish Journal of Earth Sciences*, *22*(1), 1–31.

Bagheri, S., & Stampfli, G. M. (2008). The Anarak , Jandaq and Posht-e-Badam metamorphic complexes in central Iran : New geological data , relationships and tectonic implications. *Tectonophysics*, *451*, 123–155. https://doi.org/10.1016/j.tecto.2007.11.047

Ballato, P., Nowaczyk, N. R., Landgraf, A., Strecker, M. R., Friedrich, A., & Tabatabaei, S. H. (2008). Tectonic control on sedimentary facies pattern and sediment accumulation rates in the Miocene foreland basin of the southern Alborz mountains, northern Iran. *Tectonics*, *27*(6), 1–20. https://doi.org/10.1029/2008TC002278

Ballato, P., Uba, C. E., Landgraf, A., Strecker, M. R., Sudo, M., Stockli, D. F., et al. (2011). Arabia-Eurasia continental collision: Insights from late Tertiary foreland-basin evolution in the Alborz Mountains, Northern Iran. *Bulletin of the Geological Society of America*, *123*(1–2), 106–131. https://doi.org/10.1130/B30091.1

Ballato, P., Landgraf, A., Schildgen, T. F., Stockli, D. F., Fox, M., Ghassemi, M. R., et al. (2015). The growth of a mountain belt forced by base-level fall: Tectonics and surface processes during the evolution of the Alborz Mountains, N Iran. *Earth and Planetary Science Letters*, *425*, 204–218. https://doi.org/10.1016/j.epsl.2015.05.051

Ballato, P., Cifelli, F., Heidarzadeh, G., Ghassemi, M. R., Wickert, A. D., Hassanzadeh, J., et al. (2017). Tectono-sedimentary evolution of the northern Iranian Plateau: insights from middle–late Miocene foreland-basin deposits. *Basin Research*, *29*(4), 417–446. https://doi.org/10.1111/bre.12180

Barber, D. E., Stocckli, D. F., Horton, B. K., & Koshnaw, R. I. (2018). Cenozoic Exhumation and Foreland Basin Evolution of the Zagros Orogen During the Arabia-Eurasia Collision, Western Iran. *Tectonics*, *37*, 4396–4420. https://doi.org/10.1029/2018TC005328

Barrier, É., & Vrielynck, B. (2008). Palaeotectonic map of the Middle East, Atlas of 14 maps, tectonosedimentary-palinspastic maps from Late Norian to Pliocene. *Commission for the Geologic Map of the World (CCMW, CCGM), Paris, France*.

Becker, T. W., & Boschi, L. (2002). A comparison of tomographic and geodynamic mantle models. *Geochemistry, Geophysics, Geosystems*, *3*(1), n/a-n/a. https://doi.org/10.1029/2001GC000168

Becker, T. W., Faccenna, C., O'Connell, R. J., & Giardini, D. (1999). The development of slabs

in the upper mantle: Insights from numerical and laboratory experiments. *Journal of Geophysical Research: Solid Earth*, *104*(B7), 15207–15226. https://doi.org/10.1029/1999JB900140

Behn, M. D., Conrad, C. P., & Silver, P. G. (2004). Detection of upper mantle flow associated with the African Superplume. *Earth and Planetary Science Letters*, *224*(3–4), 259–274.

Běhounková, M., & Čížková, H. (2008). Long-wavelength character of subducted slabs in the lower mantle. *Earth and Planetary Science Letters*, *275*(1–2), 43–53. https://doi.org/10.1016/j.epsl.2008.07.059

Berberian, M., & King, G. C. P. (1981). Towards a paleogeography and tectonic evolution of Iran. *Canadian Journal of Earth Sciences*, *18*(2), 210–265. https://doi.org/10.1139/e81-019

Billen, M. I., & Arredondo, K. M. (2018). Decoupling of plate-asthenosphere motion caused by non-linear viscosity during slab folding in the transition zone. *Physics of the Earth and Planetary Interiors*, *281*, 17–30. https://doi.org/10.1016/j.pepi.2018.04.011

Billen, M. I., & Hirth, G. (2007). Rheologic controls on slab dynamics. *Geochemistry, Geophysics, Geosystems*, *8*(8). https://doi.org/10.1029/2007GC001597

Blanc, E. J.-P., Allen, M. B., Inger, S., & Hassani, H. (2003). Structural styles in the Zagros Simple Folded Zone, Iran. *Journal of the Geological Society*, *160*(3), 401–412. https://doi.org/10.1144/0016-764902-110

Brooks, A. N., & Hughes, T. J. R. (1982). Streamline upwind/Petrov-Galerkin formulations for convection dominated flows with particular emphasis on the incompressible Navier-Stokes equations. *Computer Methods in Applied Mechanics and Engineering*, *32*(1–3), 199–259.

Bull, A. L., McNamara, A. K., & Ritsema, J. (2009). Synthetic tomography of plume clusters and thermochemical piles. *Earth and Planetary Science Letters*, *278*(3–4), 152–162. https://doi.org/10.1016/j.epsl.2008.11.018

Burg, J.-P. (2018). Geology of the onshore Makran accretionary wedge: Synthesis and tectonic interpretation. *Earth-Science Reviews*, *185*(April), 1210–1231. https://doi.org/10.1016/j.earscirev.2018.09.011

Burgess, P. M., & Moresi, L. N. (1999). Modelling rates and distribution of subsidence due to dynamic topography over subducting slabs: is it possible to identify dynamic topography from ancient strata? *Basin Research*, *11*(4), 305–314.

Burov, E. B. (2011). Rheology and strength of the lithosphere. *Marine and Petroleum Geology*. Elsevier Ltd. https://doi.org/10.1016/j.marpetgeo.2011.05.008

Byerlee, J. (1978). Friction of rocks. In *Rock friction and earthquake prediction* (pp. 615–626). Springer.

Calzolari, G., Rossetti, F., Seta, M. Della, Nozaem, R., Olivetti, V., Balestrieri, M. L., et al. (2016). Spatio-temporal evolution of intraplate strike-slip faulting: The Neogene-Quaternary Kuh-e-Faghan Fault, central Iran. *Bulletin of the Geological Society of America*, *128*(3–4), 374–396. https://doi.org/10.1130/B31266.1

Capitanio, F., Morra, G., & Goes, S. (2007). Dynamic models of downgoing plate-buoyancy driven subduction: Subduction motions and energy dissipation. *Earth and Planetary Science Letters*, *262*(1–2), 284–297. https://doi.org/10.1016/j.epsl.2007.07.039

Cerpa, N. G., Araya, R., Gerbault, M., & Hassani, R. (2015). Relationship between slab dip and topography segmentation in an oblique subduction zone: Insights from numerical modeling. *Geophysical Research Letters*, *42*(14), 5786–5795. https://doi.org/10.1002/2015GL064047

Chiu, H. Y., Chung, S.-L., Zarrinkoub, M. H., Mohammadi, S. S., Khatib, M. M., & Iizuka, Y. (2013). Zircon U-Pb age constraints from Iran on the magmatic evolution related to Neotethyan subduction and Zagros orogeny. *Lithos*, *162–163*, 70–87. https://doi.org/10.1016/j.lithos.2013.01.006

Chiu, H. Y., Chung, S.-L., Zarrinkoub, M. H., Melkonyan, R., Pang, K. N., Lee, H. Y., et al. (2017). Zircon Hf isotopic constraints on magmatic and tectonic evolution in Iran: Implications for crustal growth in the Tethyan orogenic belt. *Journal of Asian Earth Sciences*, *145*(March), 652–669. https://doi.org/10.1016/j.jseaes.2017.06.011

Christensen, U. (1995). Effects of phase transitions on mantle convection. *Annual Review of Earth and Planetary Sciences*, *23*(1973), 65–88. https://doi.org/0084-6597/95/0515

Christensen, U. (1996). The influence of trench migration on slab penetration into the lower mantle. *Earth and Planetary Science Letters*, *140*(1–4), 27–39. https://doi.org/10.1016/0012-821X(96)00023-4

Christensen, U. R, & Yuen, D. A. (1985). Layered convection induced by phase transitions. *Journal of Geophysical Research*, *90*(B12), 10291. https://doi.org/10.1029/JB090iB12p10291

Cifelli, F., Ballato, P., Alimohammadian, H., Sabouri, J., & Mattei, M. (2015). Tectonic magnetic lineation and oroclinal bending of the Alborz range: Implications on the Iran-Southern Caspian geodynamics. *Tectonics*, *34*(1), 116–132.

Čížková, H., & Bina, C. R., (2013). Effects of mantle and subduction-interface rheologies on slab stagnation and trench rollback. *Earth and Planetary Science Letters*, *379*, 95–103.

https://doi.org/https://doi.org/10.1016/j.epsl.2013.08.011

Čížková, H., & Bina, C. R. (2019). Linked influences on slab stagnation: Interplay between lower mantle viscosity structure, phase transitions, and plate coupling. *Earth and Planetary Science Letters*, *509*, 88–99. https://doi.org/10.1016/j.epsl.2018.12.027

Čížková, H., van Hunen, J., & van den Berg, A. (2007). Stress distribution within subducting slabs and their deformation in the transition zone. *Physics of the Earth and Planetary Interiors*, *161*(3), 202–214. https://doi.org/https://doi.org/10.1016/j.pepi.2007.02.002

Čížková, H., van den Berg, A. P., Spakman, W., & Matyska, C. (2012). The viscosity of Earth's lower mantle inferred from sinking speed of subducted lithosphere. *Physics of the Earth and Planetary Interiors*, *200–201*, 56–62. https://doi.org/https://doi.org/10.1016/j.pepi.2012.02.010

Cloos, M. (1992). Thrust-type subduction-zone earthquakes and seamount asperities: A physical model for seismic rupture. *Geology*, *20*(7), 601–604.

Crameri, F., Schmeling, H., Golabek, G. J., Duretz, T., Orendt, R., Buiter, S. J. H., et al. (2012). A comparison of numerical surface topography calculations in geodynamic modelling: An evaluation of the 'sticky air' method. *Geophysical Journal International*, *189*(1), 38–54. https://doi.org/10.1111/j.1365-246X.2012.05388.x

Crameri, F, Schmeling, H., Golabek, G. J., Duretz, T., Orendt, R., Buiter, S. J. H., et al. (2012). A comparison of numerical surface topography calculations in geodynamic modelling: An evaluation of the 'sticky air' method. *Geophysical Journal International*, *189*(1), 38–54. https://doi.org/10.1111/j.1365-246X.2012.05388.x

Crameri, F, Lithgow-Bertelloni, C. R., & Tackley, P. J. (2017). The dynamical control of subduction parameters on surface topography. *Geochemistry, Geophysics, Geosystems*, *18*(4), 1661–1687. https://doi.org/10.1002/2017GC006821

Crameri, Fabio, & Lithgow-Bertelloni, C. (2017). Abrupt upper-plate tilting during slab-transition-zone collision. *Tectonophysics*, (January). https://doi.org/10.1016/j.tecto.2017.09.013

Dávila, F. M., & Lithgow-Bertelloni, C. (2015). Dynamic uplift during slab flattening. *Earth and Planetary Science Letters*, *425*, 34–43. https://doi.org/10.1016/j.epsl.2015.05.026

Dewey, J. F., PITMAN III, W. C., Ryan, W. B. F., & Bonnin, J. (1973). Plate tectonics and the evolution of the Alpine system. *Geological Society of America Bulletin*, *84*(10), 3137–3180.

DiCaprio, L., Gurnis, M., & Müller, R. D. (2009). Long-wavelength tilting of the Australian continent since the Late Cretaceous. *Earth and Planetary Science Letters*, *278*(3), 175–

185. https://doi.org/https://doi.org/10.1016/j.epsl.2008.11.030

Dimitrijevic, M. D. (1973). *Geology of Kerman region*. *Geol Survey of Iran Rep 52:334*. Teheran.

Duretz, T., Gerya, T. V., & May, D. A. (2011). Numerical modelling of spontaneous slab breakoff and subsequent topographic response. *Tectonophysics*, *502*(1–2), 244–256. https://doi.org/10.1016/j.tecto.2010.05.024

Duretz, T., Agard, P., Yamato, P., Ducassou, C., Burov, E. B., & Gerya, T. V. (2016). Thermo-mechanical modeling of the obduction process based on the Oman Ophiolite case. *Gondwana Research*, *32*, 1–10. https://doi.org/10.1016/j.gr.2015.02.002

Dziewonski, A. M., & Anderson, D. L. (1981). Preliminary reference Earth model. *Physics of the Earth and Planetary Interiors*, *25*(4), 297–356.

Evans, B., Fredrich, J. T., & Wong, T. (1990). The brittle-ductile transition in rocks: Recent experimental and theoretical progress. *The Brittle-Ductile Transition in Rocks, Geophys. Monogr. Ser*, *56*, 1–20.

Faccenda, M., & Dal Zilio, L. (2017). The role of solid–solid phase transitions in mantle convection. *Lithos*, *268–271*, 198–224. https://doi.org/10.1016/j.lithos.2016.11.007

Faccenna, C., Becker, T. W., Conrad, C. P., & Husson, L. (201). Mountain building and mantle dynamics, *32*(December 2012). https://doi.org/10.1029/2012TC003176

Faccenna, C., Oncken, O., Holt, A. F., & Becker, T. W. (2017). Initiation of the Andean orogeny by lower mantle subduction. *Earth and Planetary Science Letters*, *463*, 189–201. https://doi.org/10.1016/j.epsl.2017.01.041

Falcon, N. L. (1974). Southern Iran: Zagros Mountains. *Geological Society, London, Special Publications*, *4*(1), 199–211. https://doi.org/10.1144/GSL.SP.2005.004.01.11

Flament, N., Gurnis, M., & Muller, R. D. (2013). A review of observations and models of dynamic topography. *Lithosphere*, *5*(2), 189–210. https://doi.org/10.1130/L245.1

Flament, Nicolas, Gurnis, M., Williams, S., Seton, M., Skogseid, J., Heine, C., & Dietmar Müller, R. (2014). Topographic asymmetry of the South Atlantic from global models of mantle flow and lithospheric stretching. *Earth and Planetary Science Letters*, *387*, 107–119. https://doi.org/10.1016/j.epsl.2013.11.017

Folguera, A., Zapata, T., & Ramos, V. A. (2006). Late Cenozoic extension and the evolution of the Neuquén Andes. *SPECIAL PAPERS-GEOLOGICAL SOCIETY OF AMERICA*, *407*, 267.

Forsyth, D., & Uyedat, S. (1975). On the Relative Importance of the Driving Forces of Plate Motion *, (2241).

Forte, A. M., Moucha, R., Simmons, N. A., Grand, S. P., & Mitrovica, J. X. (2010). Deep-mantle contributions to the surface dynamics of the North American continent. *Tectonophysics*, *481*(1–4), 3–15. https://doi.org/10.1016/j.tecto.2009.06.010

Forte, A M, Peltier, W. R., Dziewonski, A. M., & Woodward, R. L. (1993). Dynamic surface topography: A new interpretation based upon mantle flow models derived from seismic tomography. *Geophysical Research Letters*, *20*(3), 225–228. https://doi.org/10.1029/93GL00249

Forte, Alessandro M, & Mitrovica, J. X. (1996). New inferences of mantle viscosity from joint inversion of long-wavelength mantle convection and post-glacial rebound data. *Geophysical Research Letters*, *23*(10), 1147–1150.

Forte, Alessandro M, Mitrovica, J. X., & Espesset, A. (2002). Geodynamic and seismic constraints on the thermochemical structure and dynamics of convection in the deep mantle. *Philosophical Transactions. Series A, Mathematical, Physical, and Engineering Sciences*, *360*(1800), 2521–2543. https://doi.org/10.1098/rsta.2002.1079

François, T., Agard, P., Bernet, M., Meyer, B., Chung, S.-L., Zarrinkoub, M. H., et al. (2014). Cenozoic exhumation of the internal Zagros: First constraints from low-temperature thermochronology and implications for the build-up of the Iranian plateau. *Lithos*, *206–207*(1), 100–112. https://doi.org/10.1016/j.lithos.2014.07.021

Fukao, Y., & Obayashi, M. (2013). Subducted slabs stagnant above, penetrating through, and trapped below the 660 km discontinuity. *Journal of Geophysical Research: Solid Earth*, *118*(11), 5920–5938. https://doi.org/10.1002/2013JB010466

Fukao, Y., Obayashi, M., Inoue, H., & Nenbai, M. (1992). Subducting slabs stagnant in the mantle transition zone. *Journal of Geophysical Research: Solid Earth*, *97*(B4), 4809–4822.

Funiciello, F., Moroni, M., Piromallo, C., Faccenna, C., Cenedese, A., & Bui, H. A. (2006). Mapping mantle flow during retreating subduction: Laboratory models analyzed by feature tracking. *Journal of Geophysical Research: Solid Earth*, *111*(3), 1–16. https://doi.org/10.1029/2005JB003792

Funiciello, Francesca, Morra, G., Regenauer-Lieb, K., & Giardini, D. (2003). Dynamics of retreating slabs: 1. Insights from two-dimensional numerical experiments. *Journal of Geophysical Research: Solid Earth*, *108*(B4), 1–17. https://doi.org/10.1029/2001JB000898

Funiciello, Francesca, Faccenna, C., Giardini, D., & Regenauer-Lieb, K. (2003). Dynamics of retreating slabs: 2. Insights from three-dimensional laboratory experiments. *Journal of*

Geophysical Research: Solid Earth, *108*(B4). https://doi.org/10.1029/2001JB000896

Garel, F., Goes, S., Davies, D. R., Davies, J. H., Kramer, S. C., & Wilson, C. R. (2014). Interaction of subducted slabs with the mantle transition-zone: A regime diagram from 2-D thermo-mechanical models with a mobile trench and an overriding plate. *Geochemistry, Geophysics, Geosystems*, *15*(5), 1739–1765. https://doi.org/10.1002/2014GC005257

Gavillot, Y., Axen, G. J., Stöckli, D. F., Horton, B. K., & Fakhari, M. D. (2010). Timing of thrust activity in the High Zagros fold-thrust belt, Iran, from (U-Th)/He thermochronometry. *Tectonics*, *29*(4). https://doi.org/10.1029/2009TC002484

Gerya, T. V, & Yuen, D. A. (2003). Characteristics-based marker-in-cell method with conservative finite-differences schemes for modeling geological flows with strongly variable transport properties. *Physics of the Earth and Planetary Interiors*, *140*(4), 293–318. https://doi.org/https://doi.org/10.1016/j.pepi.2003.09.006

Ghasemi, H., Juteau, T., Bellon, H., Sabzehei, M., Whitechurch, H., & Ricou, L.-E. (2002). The mafic–ultramafic complex of Sikhoran (central Iran): a polygenetic ophiolite complex. *Comptes Rendus Geoscience*, *334*(6), 431–438.

Ghazi, J. M., Moazzen, M., Rahgoshay, M., & Shafaii Moghadam, H. (2012). Geochemical characteristics of basaltic rocks from the Nain ophiolite (Central Iran); constraints on mantle wedge source evolution in an oceanic back arc basin and a geodynamical model. *Tectonophysics*, *574–575*, 92–104. https://doi.org/10.1016/j.tecto.2011.10.001

Goes, S., Agrusta, R., van Hunen, J., & Garel, F. (2017). Subduction-transition zone interaction: A review. *Geosphere*, *13*(3), 644–664. https://doi.org/10.1130/GES01476.1

Golonka, J. (2004). Plate tectonic evolution of the southern margin of Eurasia in the Mesozoic and Cenozoic. *Tectonophysics*, *381*, 235–273. https://doi.org/10.1016/j.tecto.2002.06.004

Green, T., Abdullayev, N., Hossack, J., Riley, G., & Roberts, A. M. (2009). Sedimentation and subsidence in the South Caspian Basin, Azerbaijan. *Geological Society, London, Special Publications*, *312*(1), 241–260. https://doi.org/10.1144/SP312.12

Gripp, A. E., & Gordon, R. G. (2002). Young tracks of hotspots and current plate velocities. *Geophysical Journal International*, *150*(2), 321–361.

Gudmundsson, Ó., & Sambridge, M. (1998). A regionalized upper mantle (RUM) seismic model. *Journal of Geophysical Research: Solid Earth*, *103*(B4), 7121–7136. https://doi.org/10.1029/97JB02488

Guest, B., Axen, G. J., Lam, P. S., & Hassanzadeh, J. (2006). Late Cenozoic shortening in the west-central Alborz Mountains, northern Iran, by combined conjugate strike-slip and thin-skinned deformation. *Geosphere*, *2*(1), 35–52. https://doi.org/10.1130/GES00019.1

Guest, B., Stockli, D. F., Grove, M., Axen, G. J., Lam, P. S., & Hassanzadeh, J. (2006). Thermal histories from the central Alborz Mountains, northern Iran: Implications for the spatial and temporal distribution of deformation in northern Iran. *Bulletin of the Geological Society of America*, *118*(11–12), 1507–1521. https://doi.org/10.1130/B25819.1

Guillaume, B., Martinod, J., & Espurt, N. (2009). Variations of slab dip and overriding plate tectonics during subduction: Insights from analogue modelling. *Tectonophysics*, *463*(1–4), 167–174. https://doi.org/10.1016/j.tecto.2008.09.043

Guillaume, B., Moroni, M., Funiciello, F., Martinod, J., & Faccenna, C. (2010). Mantle flow and dynamic topography associated with slab window opening: Insights from laboratory models. *Tectonophysics*, *496*(1–4), 83–98. https://doi.org/10.1016/j.tecto.2010.10.014

Gurnis, M. (1990). Bounds on Global Dynamic Topography from Phanerozoic Flooding of Continental Platforms. *Nature*. https://doi.org/10.1038/344754a0

Gurnis, Michael. (1992). Eustatic and Epeirogenic Motions by Mantle Convection. *GSA TODAY*, *2*(7).

Gurnis, Michael, Mitrovica, J. X., Ritsema, J., & Van Heijst, H. J. (2000). Constraining mantle density structure using geological evidence of surface uplift rates: The case of the African Superplume. *Geochemistry, Geophysics, Geosystems*, *1*(7). https://doi.org/10.1029/1999GC000035

Hager, B. H. (1984). Subducted slabs and the geoid: constraints on mantle rheology and flow. *Journal of Geophysical Research*, *89*(B7), 6003–6015. https://doi.org/10.1029/JB089iB07p06003

Hager, B. H., & Richards, M. A. (1989). Long-Wavelength Variations in Earth's Geoid: Physical Models and Dynamical Implications. *Philosophical Transactions of the Royal Society A: Mathematical, Physical and Engineering Sciences*, *328*(1599), 309–327. https://doi.org/10.1098/rsta.1989.0038

Hager, Bradford H., & O'Connell, R. J. (1981). A simple global model of plate dynamics and mantle convection. *Journal of Geophysical Research: Solid Earth*, *86*(B6), 4843–4867. https://doi.org/10.1029/JB086iB06p04843

Hager, Bradford H., R.W., C., Richards, M. A., Comer, R. P., & Dziewonski, A. M. (1985). Lower mantle heterogeneity, dynamic topography and the geoid. *Nature*, *313*(6003), 541–545. https://doi.org/10.1038/313541a0

Haxby, W. F., & Turcotte, D. L. (1978). On isostatic geoid anomalies. *Journal of Geophysical Research: Solid Earth, 83*(B11), 5473-5478.

Hayes, G. P., Wald, D. J., & Johnson, R. L. (2012). Slab1. 0: A three-dimensional model of

global subduction zone geometries. *Journal of Geophysical Research: Solid Earth*, *117*(B1).

Heine, C., Müller, R. D., Steinberger, B., & DiCaprio, L. (2010). Integrating deep Earth dynamics in paleogeographic reconstructions of Australia. *Tectonophysics*, *483*(1–2), 135–150. https://doi.org/10.1016/j.tecto.2009.08.028

Hess, H. H. (1964). Seismic anisotropy of the uppermost mantle under oceans. *Nature*, *203*(4945), 629.

van der Hilst, R. D., Widiyantoro, S., & Engdahl, E. R. (1997). Evidence for deep mantle circulation from global tomography. *Nature*, *386*(6625), 578–584. https://doi.org/10.1038/386578a0

Hirth, G., & Kohlstedt, D. L. (1995). of the partially molten upper mantle 2 . Defonnation in the dislocation creep regime, *100*(95), 441–449.

Hirth, G., & Kohlstedt, D. L. (2003). Rheology of the Upper Mantle and the Mantle Wedge : A View from the Experimentalists upper mantle . We first analyze experimental data to provide a critical review of flow. *Geophysical Monograph Series*, *138*, 83–105. https://doi.org/10.1029/138GM06

Husson, L, & Ricard, Y. (2004). Stress balance above subduction: Application to the Andes. *Earth and Planetary Science Letters*, *222*(3–4), 1037–1050. https://doi.org/10.1016/j.epsl.2004.03.041

Husson, L. (2012). Trench migration and upper plate strain over a convecting mantle. *Physics of the Earth and Planetary Interiors*, *212–213*, 32–43. https://doi.org/10.1016/j.pepi.2012.09.006

Husson, L., Guillaume, B., Funiciello, F., Faccenna, C., & Royden, L. H. (2012). Unraveling topography around subduction zones from laboratory models. *Tectonophysics*, *526–529*, 5–15. https://doi.org/10.1016/j.tecto.2011.09.001

van Hunen, J., Van den Berg, A. P., & Vlaar, N. J. (2002). The influence of rheological weakening and yield stress on the interaction of slabs with the 670 km discontinuity. *Earth and Planetary Science Letters*, *199*(3–4), 447–457. https://doi.org/10.1016/S0012-821X(02)00586-1

Isacks, B., & Molnar, P. (1969). Mantle earthquake mechanisms and the sinking of the lithosphere. *Nature*, *223*(5211), 1121.

Isacks, B., & Molnar, P. (1971). Distribution of stresses in the descending lithosphere from a global survey of focal-mechanism solutions of mantle earthquakes. *Reviews of Geophysics*, *9*(1), 103–174.

Isacks, B., Oliver, J., & Sykes, L. R. (1968). Seismology and the new global tectonics. *Journal of Geophysical Research*, *73*(18), 5855–5899.

Ita, J., & King, S. D. (1998). The influence of thermodynamic formulation on simulations of subduction zone geometry and history. *Geophysical Research Letters*, *25*(9), 1463–1466.

Jamshidi, K., Ghasemi, H., Troll, V. R., Sadeghian, M., & Dahren, B. (2015). Magma storage and plumbing of adakite-type post-ophiolite intrusions in the Sabzevar ophiolitic zone, northeast Iran. *Solid Earth*, *6*(1), 49–72. https://doi.org/10.5194/se-6-49-2015

Jarrard, R. D. (1986). Relations among subduction parameters. *Reviews of Geophysics*, *24*(2), 217–284. https://doi.org/10.1029/RG024i002p00217

Kaban, M. K., Schwintzer, P., & Reigber, C. (2004). A new isostatic model of the lithosphere and gravity field. *Journal of Geodesy*, *78*(6), 368–385. https://doi.org/10.1007/s00190-004-0401-6

Kameyama, M., Yuen, D. A., & Karato, S.-I. (1999). Thermal-mechanical effects of low-temperature plasticity (the Peierls mechanism) on the deformation of a viscoelastic shear zone. *Earth and Planetary Science Letters*, *168*(1–2), 159–172.

Karato, S.-I., Paterson, M., & Fitzgerald, D. (1986). Rheology of Synthetic Olivine Aggregates ' for hot pressing . The Specimens were then sleeve and for temperature is jacket 1) and were hot pressed. *Journal of Geophysical Research*, *91*(B8), 8151–8176. https://doi.org/10.1029/JB091iB08p08151

Karato, S.-I., & Wu, P. (1993). Rheology of the Upper Mantle: A Synthesis. *Science*, *260*(5109), 771 LP – 778. https://doi.org/10.1126/science.260.5109.771

Karato, Shun ichiro. (2010). Rheology of the Earth's mantle: A historical review. *Gondwana Research*, *18*(1), 17–45. https://doi.org/10.1016/j.gr.2010.03.004

Kargaranbafghi, F., Foeken, J. P. T., Guest, B., & Stuart, F. M. (2012). Cooling history of the Chapedony metamorphic core complex, Central Iran: Implications for the Eurasia-Arabia collision. *Tectonophysics*, *524–525*, 100–107. https://doi.org/10.1016/j.tecto.2011.12.022

Katsura, T., & Ito, E. (1989). The system Mg_2SiO_4-Fe_2SiO_4 at high pressures and temperatures: Precise determination of stabilities of olivine, modified spinel, and spinel. *Journal of Geophysical Research: Solid Earth*, *94*(B11), 15663–15670. https://doi.org/10.1029/JB094iB11p15663

Kay, S. M., Godoy, E., & Kurtz, A. (2005). Episodic arc migration, crustal thickening, subduction erosion, and magmatism in the south-central Andes. *Geological Society of America Bulletin*, *117*(1–2), 67–88.

Kincaid, C., & Olson, P. (1987). An experimental study of subduction and slab migration.

Journal of Geophysical Research: Solid Earth, *92*(B13), 13832–13840. https://doi.org/10.1029/JB092iB13p13832

King, S D. (2001). Subduction zones: Observations and geodynamic models. *Physics of the Earth and Planetary Interiors*, *127*(1–4), 9–24. https://doi.org/10.1016/S0031-9201(01)00218-7

King, S D. (2007). Mantle downwellings and the fate of subducting slabs: Constraints from seismology, geoid topography, geochemistry, and petrology.

King, S D. (2002). Geoid and topography over subduction zones: The effect of phase transformations. *Journal of Geophysical Research: Solid Earth*, *107*(B1), ETG 2-1–ETP 2-10. https://doi.org/10.1029/2000JB000141

King, S D. (2016). Reconciling laboratory and observational models of mantle rheology in geodynamic modelling. *Journal of Geodynamics*, *100*, 33–50. https://doi.org/10.1016/j.jog.2016.03.005

Kohlstedt, D. L., Evans, B., & Mackwell, S. J. (1995). Strength of the lithosphere: Constraints imposed by laboratory experiments. *Journal of Geophysical Research: Solid Earth*, *100*(B9), 17587–17602.

Koshnaw, R. I., Stockli, D. F., & Schlunegger, F. (2018). Timing of the Arabia-Eurasia continental collision-Evidence from detrital zircon U-Pb geochronology of the Red Bed Series strata of the northwest Zagros hinterland, Kurdistan region of Iraq. *Geology*, *47*(1), 47–50. https://doi.org/10.1130/G45499.1

Kreemer, C., Holt, W. E., & Haines, A. J. (2003). An integrated global model of present-day plate motions and plate boundary deformation. *Geophysical Journal International*, *154*(1), 8–34.

Lallemand, S., Heuret, A., & Boutelier, D. (2005). On the relationships between slab dip, back-arc stress, upper plate absolute motion, and crustal nature in subduction zones. *Geochemistry, Geophysics, Geosystems*, *6*(9). https://doi.org/10.1029/2005GC000917

Lambeck, K., & Nakada, M. (1990). Late Pleistocene and Holocene sea-level change along the Australian coast. *Palaeogeography, Palaeoclimatology, Palaeoecology*, *89*(1–2), 143–176.

Lee, C., & King, S. D. (2011). Dynamic buckling of subducting slabs reconciles geological and geophysical observations. *Earth and Planetary Science Letters*, *312*(3–4), 360–370. https://doi.org/10.1016/j.epsl.2011.10.033

Leterrier, J. (1985). Mineralogical, geochemical and isotopic evolution of two Miocene mafic intrusions from the Zagros (Iran). *Lithos*, *18*(C), 311–329. https://doi.org/10.1016/0024-

4937(85)90034-9

Li, C., van der Hilst, R. D., Engdahl, E. R., & Burdick, S. (2008). A new global model for P wave speed variations in Earth's mantle. *Geochemistry, Geophysics, Geosystems*, *9*(5). https://doi.org/10.1029/2007GC001806

Litasov, K. D., & Ohtani, E. (2007). and Deep Water Cycle, *2421*(08), 115–156. https://doi.org/10.1130/2007.2421(08).

Lithgow-Bertelloni, C. (1997). Cenozoic subsidence and uplift of continents from time-varying dynamic topography. *Geology*, *25*(8), 735–738. https://doi.org/10.1130/0091-7613(1997)025<0735:CSAUOC>2.3.CO;2

Lithgow-Bertelloni, C., & Silver, P. (1998). Dynamic topography, plate driving forces and the African superswell. *Nature*, *395*(September), 345–348. https://doi.org/10.1038/26212

Liu, L., Spasojevic, S., & Gurnis, M. (2008). Reconstructing Farallon Plate Subduction Beneath North America Back to the Late Cretaceous. *Science*, *322*(5903), 934–938. https://doi.org/10.1126/science.1162921

Madanipour, S., Ehlers, T. A., Yassaghi, A., & Enkelmann, E. (2017). Accelerated middle Miocene exhumation of the Talesh Mountains constrained by U-Th/He thermochronometry: Evidence for the Arabia-Eurasia collision in the NW Iranian Plateau. *Tectonics*, *36*(8), 1538–1561.

Madanipour, S., Yassaghi, A., Ehlers, T. A., & Enkelmann, E. (2018). *Tectonostratigraphy, structural geometry and kinematics of the NW Iranian Plateau margin: Insights from the Talesh Mountains, Iran*. *American Journal of Science* (Vol. 318). https://doi.org/10.2475/02.2018.02

Mammadov, P. Z. (2008). The subsidence evolution of the South Caspian Basin. In *EAGE International Conference on Petroleum Geology and Hydrocarbon Potential of Caspian and Black Sea Regions*.

Mao, W., & Zhong, S. (2018). Slab stagnation due to a reduced viscosity layer beneath the mantle transition zone. *Nature Geoscience*, 41–43. https://doi.org/10.1038/s41561-018-0225-2

Martinod, J., Guillaume, B., Espurt, N., Faccenna, C., Funiciello, F., & Regard, V. (2013). Effect of aseismic ridge subduction on slab geometry and overriding plate deformation: Insights from analogue modeling. *Tectonophysics*, *588*, 39–55. https://doi.org/10.1016/j.tecto.2012.12.010

Martinod, J., Regard, V., Letourmy, Y., Henry, H., Hassani, R., Baratchart, S., & Carretier, S. (2016). How do subduction processes contribute to forearc Andean uplift? Insights from

numerical models. *Journal of Geodynamics*, *96*, 6–18.

Mattei, M., Cifelli, F., Muttoni, G., & Rashid, H. (2015). Post-Cimmerian (Jurassic-Cenozoic) paleogeography and vertical axis tectonic rotations of Central Iran and the Alborz Mountains. *Journal of Asian Earth Sciences*, *102*, 92–101. https://doi.org/10.1016/j.jseaes.2014.09.038

Mattei, M., Cifelli, F., Alimohammadian, H., Rashid, H., Winkler, A., & Sagnotti, L. (2017). Oroclinal bending in the Alborz Mountains (Northern Iran): New constraints on the age of South Caspian subduction and extrusion tectonics. *Gondwana Research*, *42*, 13–28. https://doi.org/10.1016/j.gr.2016.10.003

Mazhari, S. A., Bea, F., Amini, S., Ghalamghash, J., Molina, J. F., Montero, P., et al. (2013). The Eocene bimodal Piranshahr massif of the Sanandaj − Sirjan Zone , NW Iran : a marker of the end of the collision in the Zagros orogen. *Journal of the Geological Society, London*, *166*, 53–69. https://doi.org/10.1144/0016-76492008-022

McKenzie, D P. (1977). The initiation of trenches: a finite amplitude instability. *Island Arcs, Deep Sea Trenches and Back-arc Basins*, *1*, 57–61.

McKenzie, D P. (1969). Speculations on the consequences and causes of plate motions. *Geophysical Journal International*, *18*(1), 1–32.

McQuarrie, N. (2004). Crustal scale geometry of the Zagros fold – thrust belt , Iran. *Journal of Structural Geology*, *26*, 519–535. https://doi.org/10.1016/j.jsg.2003.08.009

McQuarrie, N., & van Hinsbergen, D. J. J. (2013). Retrodeforming the Arabia-Eurasia collision zone: Age of collision versus magnitude of continental subduction. *Geology*, *41*(3), 315–318. https://doi.org/10.1130/G33591.1

van Der Meer, D. G., Spakman, W., Van Hinsbergen, D. J. J., Amaru, M. L., & Torsvik, T. H. (2010). Towards absolute plate motions constrained by lower-mantle slab remnants. *Nature Geoscience*, *3*(1), 36–40. https://doi.org/10.1038/ngeo708

Mitrovica, J. X., Beaumont, C., & Jarvis, G. T. (1989). Tilting of continental interiors by the dynamical effects of subduction. *Tectonics*, *8*(5), 1079–1094. https://doi.org/10.1029/TC008i005p01079

Mitrovica, J X, & Forte, A. M. (2004). A new inference of mantle viscosity based upon joint inversion of convection and glacial isostatic adjustment data. *Earth and Planetary Science Letters*, *225*(1–2), 177–189.

Mitrovica, J X, Pysklywec, R. N., Beaumont, C., & Rutty, A. (1996). The Devonian to Permian sedimentation of the Russian Platform: An example of subduction controlled long-wavelength tilting of continents. *J. Geodyn.*, *22*(112), 79–96.

https://doi.org/10.1016/0264-3707(96)00008-7

Monsef, I., Rahgoshay, M., Mohajjel, M., & Moghadam, H. S. (2010). Peridotites from the Khoy Ophiolitic Complex, NW Iran: Evidence of mantle dynamics in a supra-subduction-zone context. *Journal of Asian Earth Sciences*, *38*(3–4), 105–120.

Moresi, L., & Solomatov, V. S. (1995). Numerical investigation of 2D convection with extremely large viscosity variations. *Physics of Fluids*, *7*(9), 2154–2162.

Moresi, L., & Gumis, M. (1996). Dynamic Flow Models. *Earth and Planetary Science Letters*, *38*(95), 15–28.

Moritz, R., Ghazban, F., & Singer, B. S. (2006). Eocene gold ore formation at Muteh, Sanandaj-Sirjan tectonic zone, western Iran: A result of late-stage extension and exhumation of metamorphic basement rocks within the Zagros orogen. *Economic Geology*, *101*(8), 1497–1524. https://doi.org/10.2113/gsecongeo.101.8.1497

Morley, C. K., Kongwung, B., Julapour, A., Abdolghafourian, M., Hajian, M., Waples, D., et al. (2009). Structural development of a major late Cenozoic basin and transpressional belt in central Iran: The Central Basin in the Qom-Saveh area. *Geosphere*, *5*(4), 325–362. https://doi.org/10.1130/GES00223.1

Mouthereau, F. (2011). Timing of uplift in the Zagros belt/Iranian plateau and accommodation of late Cenozoic Arabia-Eurasia convergence. *Geological Magazine*, *148*(5–6), 726–738. https://doi.org/10.1017/S0016756811000306

Müller, R. D., Sdrolias, M., Gaina, C., & Roest, W. R. (2008). Age, spreading rates, and spreading asymmetry of the world's ocean crust. *Geochemistry, Geophysics, Geosystems*, *9*(4), 1–19. https://doi.org/10.1029/2007GC001743

Myhill, R. (2012). Slab buckling and its effect on the distributions and focal mechanisms of deep-focus earthquakes. *Geophysical Journal International*, *192*(2), 837–853.

Nouri, F., Azizi, H., Golonka, J., Asahara, Y., Orihashi, Y., Yamamoto, K., et al. (2016). Age and petrogenesis of Na-rich felsic rocks in western Iran: Evidence for closure of the southern branch of the Neo-Tethys in the Late Cretaceous. *Tectonophysics*, *671*, 151–172. https://doi.org/10.1016/j.tecto.2015.12.014

Omrani, H. (2018). Island-arc and Active Continental Margin Adakites from the Sabzevar Zone, Iran. *Petrology*, *26*(1), 96–113. https://doi.org/10.1134/S0869591118010058

Omrani, H., Moazzen, M., & Oberhänsli, R. (2018). Geodynamic evolution of the Sabzevar zone, northern central Iranian micro-continent. *Mineralogy and Petrology*, *112*(1), 65–83. https://doi.org/10.1007/s00710-017-0505-3

Omrani, J., Agard, P., Whitechurch, H., Benoit, M., Prouteau, G., & Jolivet, L. (2008). Arc

magmatism and subduction history beneath the Zagros Mountains, Iran: A new report of adakites and geodynamic consequences. *Lithos*, *113*(3–4), 847–849. https://doi.org/10.1016/j.lithos.2009.04.012

Panasyuk, S. V., & Hager, B. H. (2000). Models of isostatic and dynamic topography, geoid anomalies, and their uncertainties. *Journal of Geophysical Research*, *105*(B12), 28199–28209. https://doi.org/10.1029/2000JB900249

Pang, K. N., Chung, S.-L., Zarrinkoub, M. H., Khatib, M. M., Mohammadi, S. S., Chiu, H. Y., et al. (2013). Eocene-Oligocene post-collisional magmatism in the Lut-Sistan region, eastern Iran: Magma genesis and tectonic implications. *Lithos*, *180–181*, 234–251. https://doi.org/10.1016/j.lithos.2013.05.009

Pang, K. N., Chung, S.-L., Zarrinkoub, M. H., Chiu, H. Y., & Li, X. H. (2014). On themagmatic record of the Makran arc, southeastern Iran: Insights fromzircon U-Pb geochronology and bulk-rock geochemistry. *Geochemistry, Geophysics, Geosystems*, (15), 2151–2169. https://doi.org/10.1002/2015GC005918.Received

Pari, G., & Peltier, W. R. (1995). The heat flow constraint on mantle tomography-based convection models: Towards a geodynamically self-consistent inference of mantle viscosity. *Journal of Geophysical Research: Solid Earth*, *100*(B7), 12731–12751. https://doi.org/10.1029/95JB01078

Paul, A., Kaviani, A., Hatzfeld, D., Vergne, J., & Mokhtari, M. (2006). Seismological evidence for crustal-scale thrusting in the Zagros. *Geophysical Journal International*, *166*, 227–237. https://doi.org/10.1111/j.1365-246X.2006.02920.x

Paulson, A., Zhong, S., & Wahr, J. (2007). Inference of mantle viscosity from GRACE and relative sea level data. *Geophysical Journal International*, *171*(2), 497–508.

Peltier, W. R. (1981). Ice age geodynamics. *Annual Review of Earth and Planetary Sciences*, *9*(1), 199–225.

Peltier, W. R. (1998). Postglacial variations in the level of the sea: Implications for climate dynamics and solid-earth geophysics. *Reviews of Geophysics*, *36*(4), 603–689.

Pérez-Peña, J. V., Azor, A., Azañón, J. M., & Keller, E. A. (2010). Active tectonics in the Sierra Nevada (Betic Cordillera, SE Spain): Insights from geomorphic indexes and drainage pattern analysis. *Geomorphology*, *119*(1), 74–87. https://doi.org/https://doi.org/10.1016/j.geomorph.2010.02.020

Le Pichon, X. (1968). Sea-floor spreading and continental drift. *Journal of Geophysical Research*, *73*(12), 3661–3697.

Pirnia, T., Arai, S., & Torabi, G. (2013). Better picture of the mantle section of the Nain

ophiolite inferred from detrital chromian spinels. *Journal of Geology*, *121*(6), 645–661. https://doi.org/10.1086/673175

Pirnia, T., Saccani, E., & Arai, S. (2018). Spinel and plagioclase peridotites of the Nain ophiolite (Central Iran): Evidence for the incipient stage of oceanic basin formation. *Lithos*, *310–311*, 1–19. https://doi.org/10.1016/j.lithos.2018.04.001

Pirouz, M., Avouac, J. P., Hassanzadeh, J., Kirschvink, J. L., & Bahroudi, A. (2017). Early Neogene foreland of the Zagros, implications for the initial closure of the Neo-Tethys and kinematics of crustal shortening. *Earth and Planetary Science Letters*, *477*, 168–182. https://doi.org/10.1016/j.epsl.2017.07.046

Pysklywec, R., & Mitrovica, J. (1997). Mantle avalanches and the dynamic topography of continents. *Earth and Planetary Science Letters*, *148*(3–4), 447–455. https://doi.org/10.1016/S0012-821X(97)00045-9

Pysklywec, R. N., & Mitrovica, J. X. (1999). The Role of Subduction-Induced Subsidence in the Evolution of the Karoo Basin. *The Journal of Geology*, *107*(2), 155–164. https://doi.org/10.1086/314338

Regenauer-Lieb, K., & Yuen, D. A. (2003). Modeling shear zones in geological and planetary sciences: solid-and fluid-thermal–mechanical approaches. *Earth-Science Reviews*, *63*(3–4), 295–349.

Rezaeian, M., Carter, A., Hovius, N., & Allen, M. B. (2012). Cenozoic exhumation history of the Alborz Mountains, Iran: New constraints from low-temperature chronometry. *Tectonics*, *31*(2), 1–20. https://doi.org/10.1029/2011TC002974

Ribe, N. M. (2003). Periodic folding of viscous sheets. *Physical Review E - Statistical Physics, Plasmas, Fluids, and Related Interdisciplinary Topics*, *68*(3), 6. https://doi.org/10.1103/PhysRevE.68.036305

Ricard, Y., Fleitout, L., & Froidevaux, C. (1984). Geoid heights and lithospheric stresses for a dynamic earth. *Annales Geophysicae*. Retrieved from http://adsabs.harvard.edu/abs/1984AnGeo...2..267R

Ricard, Yanick, & Vigny, C. (1989). Mantle dynamics with induced plate tectonics. *Journal of Geophysical Research: Solid Earth*, *94*(B12), 17543–17559.

Ricard, Yanick, Richards, M., Lithgow-Bertelloni, C., & Le Stunff, Y. (1993). A geodynamic model of mantle density heterogeneity. *Journal of Geophysical Research: Solid Earth*, *98*(B12), 21895–21909. https://doi.org/10.1029/93JB02216

Richards, M. A., & Hager, B. H. (1984). Geoid anomaly in a dynamic Earth. *Journal of Geophysical Research*, *89*, 5987–6002.

Ritsema, J., Van Heijst, H. J., & Woodhouse, J. H. (2004). Global transition zone tomography. *Journal of Geophysical Research: Solid Earth*, *109*(B2).

Rossetti, F., Nasrabady, M., Vignaroli, G., Theye, T., Gerdes, A., Razavi, M. H., & Vaziri, H. M. (2010). Early Cretaceous migmatitic mafic granulites from the Sabzevar range (NE Iran): Implications for the closure of the Mesozoic peri-Tethyan oceans in central Iran. *Terra Nova*, *22*(1), 26–34. https://doi.org/10.1111/j.1365-3121.2009.00912.x

Rossetti, F., Nasrabady, M., Theye, T., Gerdes, A., Monié, P., Lucci, F., & Vignaroli, G. (2014). Adakite differentiation and emplacement in a subduction channel: The late paleocene Sabzevar magmatism (NE Iran). *Bulletin of the Geological Society of America*, *126*(3–4), 317–343. https://doi.org/10.1130/B30913.1

Rubie, D. C., & Ross II, C. R. (1994). Kinetics of the olivine-spinel transformation in subducting lithosphere: Experimental constraints and implications for deep slab processes. *Physics of the Earth and Planetary Interiors*, *86*(1–3), 223–243.

Saccani, E., Delavari, M., Beccaluva, L., & Amini, S. (2010). Petrological and geochemical constraints on the origin of the Nehbandan ophiolitic complex (eastern Iran): Implication for the evolution of the Sistan Ocean. *Lithos*, *117*(1–4), 209–228. https://doi.org/10.1016/j.lithos.2010.02.016

Saccani, E., Allahyari, K., & Rahimzadeh, B. (2014). Petrology and geochemistry of mafic magmatic rocks from the Sarve-Abad ophiolites (Kurdistan region, Iran): Evidence for interaction between MORB-type asthenosphere and OIB-type components in the southern Neo-Tethys Ocean. *Tectonophysics*, *621*, 132–147. https://doi.org/10.1016/j.tecto.2014.02.011

Saidi, A., Brunet, M., & Ricou, L. (1997). Continental accretion of the Iran Block to Eurasia as seen from Late Paleozoic to Early Cretaceous subsidence curves Continental accretion of the Iran Block to Eurasia as seen from Late Paleozoic to Early Cretaceous subsidence curves. *Geodinamica Acta*, *10*(5), 189–208. https://doi.org/10.1080/09853111.1997.11105302

Satolli, S., Pace, P., Viandante, M. G., & Calamita, F. (2014). Lateral variations in tectonic style across cross-strike discontinuities: An example from the central Apennines belt (Italy). *International Journal of Earth Sciences*, *103*(8), 2301–2313. https://doi.org/10.1007/s00531-014-1052-3

Schellart, W. P., Freeman, J., Stegman, D. R., Moresi, L., & May, D. (2007). Evolution and diversity of subduction zones controlled by slab width. *Nature*, *446*(7133), 308.

Sembroni, A., Molin, P., Pazzaglia, F. J., Faccenna, C., & Abebe, B. (2016). Evolution of

continental-scale drainage in response to mantle dynamics and surface processes: An example from the Ethiopian Highlands. *Geomorphology*, *261*, 12–29. https://doi.org/10.1016/j.geomorph.2016.02.022

Sengör, A. M. C., Yilmaz, Y., & Sungurlu, O. (1984). Tectonics of the Mediterranean Cimmerides: nature and evolution of the western termination of Paleo-Tethys. *Geological Society of London Special Publication*, *17*(1), 77–112.

Sepahi, A. A., & Athari, S. F. (2006). Petrology of major granitic plutons of the northwestern part of the Sanandaj-Sirjan Metamorphic Belt, Zagros Orogen, Iran: with emphasis on A-type granitoids from the SE Saqqez area. *Neues Jahrbuch Für Mineralogie - Abhandlungen*, *183*(1), 93–106. https://doi.org/10.1127/0077-7757/2006/0063

Seton, M., Müller, R. D., Zahirovic, S., Gaina, C., Torsvik, T., Shephard, G., et al. (2012). Global continental and ocean basin reconstructions since 200Ma. *Earth-Science Reviews*, *113*(3–4), 212–270. https://doi.org/10.1016/j.earscirev.2012.03.002

Shabanian, E., Acocella, V., Gioncada, A., Ghasemi, H., & Bellier, O. (2012). Structural control on volcanism in intraplate post collisional settings: Late Cenozoic to Quaternary examples of Iran and Eastern Turkey. *Tectonics*, *31*(3), 1–25. https://doi.org/10.1029/2011TC003042

Shafaii Moghadam, H., & Stern, R. J. (2015). Ophiolites of Iran: Keys to understanding the tectonic evolution of SW Asia: (II) Mesozoic ophiolites. *Journal of Asian Earth Sciences*, *100*, 31–59. https://doi.org/10.1016/j.jseaes.2014.12.016

Shafaii Moghadam, H., Whitechurch, H., Rahgoshay, M., & Monsef, I. (2009). Significance of Nain-Baft ophiolitic belt (Iran): Short-lived, transtensional Cretaceous back-arc oceanic basins over the Tethyan subduction zone. *Comptes Rendus - Geoscience*, *341*(12), 1016–1028. https://doi.org/10.1016/j.crte.2009.06.011

Shafaii Moghadam, H., Corfu, F., Chiaradia, M., Stern, R. J., & Ghorbani, G. (2014). Sabzevar Ophiolite, NE Iran: Progress from embryonic oceanic lithosphere into magmatic arc constrained by new isotopic and geochemical data. *Lithos*, *210–211*, 224–241. https://doi.org/10.1016/j.lithos.2014.10.004

Shafaii Moghadam, H., Rossetti, F., Lucci, F., Chiaradia, M., Gerdes, A., Martinez, M. L., et al. (2016). The calc-alkaline and adakitic volcanism of the Sabzevar structural zone (NE Iran): Implications for the Eocene magmatic flare-up in Central Iran. *Lithos*, *248–251*, 517–535. https://doi.org/10.1016/j.lithos.2016.01.019

Sherkati, S., Letouzey, J., & Frizon de Lamotte, D. (2006). Central Zagros fold-thrust belt (Iran): New insights from seismic data , field observation , and sandbox modeling.

Tectonics, *25*(January), 1–27. https://doi.org/10.1029/2004TC001766

Sigloch, K., & Mihalynuk, M. G. (2013). Intra-oceanic subduction shaped the assembly of Cordilleran North America. *Nature*, *496*(7443), 50.

Sigmundsson, F. (1991). Post-glacial rebound and asthenosphere viscosity in Iceland. *Geophysical Research Letters*, *18*(6), 1131–1134.

Simmons, N. A., Forte, A. M., Boschi, L., & Grand, S. P. (2010). GyPSuM: A joint tomographic model of mantle density and seismic wave speeds. *Journal of Geophysical Research: Solid Earth*, *115*(B12).

Stampfli, G. M., & Borel, G. D. (2002). A plate tectonic model for the Paleozoic and Mesozoic constrained by dynamic plate boundaries and restored synthetic oceanic isochrons. *Earth and Planetary Science Letters*, *196*, 17–33.

Stark, P. B., & Frohlich, C. (1985). The depths of the deepest deep earthquakes. *Journal of Geophysical Research: Solid Earth*, *90*(B2), 1859–1869.

Steinberger, B. (2007). Effects of latent heat release at phase boundaries on flow in the Earth's mantle, phase boundary topography and dynamic topography at the Earth's surface. *Physics of the Earth and Planetary Interiors*, *164*(1–2), 2–20. https://doi.org/10.1016/j.pepi.2007.04.021

Steinberger, B., & Calderwood, A. R. (2006). Models of large-scale viscous flow in the Earth's mantle with constraints from mineral physics and surface observations. *Geophysical Journal International*, *167*(3), 1461–1481. https://doi.org/10.1111/j.1365-246X.2006.03131.x

Steinberger, B., Schmeling, H., & Marquart, G. (2001). Large-scale lithospheric stress field and topography induced by global mantle circulation. *Earth and Planetary Science Letters*, *186*(1), 75–91. https://doi.org/https://doi.org/10.1016/S0012-821X(01)00229-1

Stocklin, J., & Nabavi, M. H. (1973). Tectonic map of Iran. *Geological Survey of Iran*.

Stoneley, R. (2015). The geology of the Kuh-e Dalneshin area of southern Iran , and its bearing on the evolution of southern Tethys. *Journal of the Geological Society, London*, *l*(Falcon 1974), 509–526.

Taylor, B., & Karner, G. D. (1983). On the evolution of marginal basins. *Reviews of Geophysics*, *21*(8), 1727–1741.

Torsvik, T. H., Van der Voo, R., Preeden, U., Mac Niocaill, C., Steinberger, B., Doubrovine, P. V, et al. (2012). Phanerozoic Polar Wander, Palaeogeography and Dynamics. *Earth-Science Reviews*, *114*(3–4), 325–368. https://doi.org/10.1016/j.earscirev.2012.06.007

Tosi, N., ˇadek, O., & Martinec, Z. (2009). Subducted slabs and lateral viscosity variations:

Effects on the long-wavelength geoid. *Geophysical Journal International*, *179*(2), 813–826. https://doi.org/10.1111/j.1365-246X.2009.04335.x

Tosi, N., Yuen, D. A., de Koker, N., & Wentzcovitch, R. M. (2013). Mantle dynamics with pressure- and temperature-dependent thermal expansivity and conductivity. *Physics of the Earth and Planetary Interiors*, *217*, 48–58. https://doi.org/10.1016/j.pepi.2013.02.004

Tosi, N., Maierová, P., & Yuen, D. A. (2015). Influence of Variable Thermal Expansivity and Conductivity on Deep Subduction. *Subduction Dynamics*. https://doi.org/doi:10.1002/9781118888865.ch6

Turcotte, D., & Schubert, G. (2002). *Geodynamics* (2nd ed.). Cambridge University Press.

Verdel, C., Wernicke, B. P., Ramezani, J., Hassanzadeh, J., Renne, P. R., & Spell, T. L. (2007). Geology and thermochronology of Tertiary Cordilleran-style metamorphic core complexes in the Saghand region of central Iran. *Bulletin of the Geological Society of America*, *119*(7–8), 961–977. https://doi.org/10.1130/B26102.1

Verdel, C., Wernicke, B. P., Hassanzadeh, J., & Guest, B. (2011). A Paleogene extensional arc flare-up in Iran. *Tectonics*, *30*(3), 1–20. https://doi.org/10.1029/2010TC002809

Wang, H., Agrusta, R., & van Hunen, J. (2015). Advantages of a conservative velocity interpolation (CVI) scheme for particle-in-cell methods with application in geodynamic modeling. *Geochemistry, Geophysics, Geosystems*, *16*(6), 2015–2023. https://doi.org/10.1002/2015GC005824

Watts, A. B. (1978). An analysis of isostasy in the world's oceans 1. Hawaiian-Emperor Seamount Chain. *Journal of Geophysical Research: Solid Earth*, *83*(B12), 5989–6004. https://doi.org/10.1029/JB083iB12p05989

Wilmsen, M., Wiese, F., Seyed-emami, K., & Fu, F. T. (2005). First record and significance of Turonian ammonites from the Shotori Mountains , east-central Iran. *Cretaceous Research*, *26*, 181–195. https://doi.org/10.1016/j.cretres.2004.10.004

Wilmsen, M., Fürsich, F. T., Seyed-emami, K., & Majidifard, R. (2009). An overview of the stratigraphy and facies development of the Jurassic System on the Tabas Block , east-central Iran. *Geological Society of London Special Publication*, 323–343.

Wilmsen, M., Theodor, F., & Majidifard, R. (2015). Journal of Asian Earth Sciences An overview of the Cretaceous stratigraphy and facies development of the Yazd Block , western Central Iran. *Journal of Asian Earth Sciences*, *102*, 73–91. https://doi.org/10.1016/j.jseaes.2014.07.015

Wilmsen, M., Berensmeier, M., Theodor, F., Mahmoud, F., Majidifard, R., & Schlagintweit, F. (2018). A Late Cretaceous epeiric carbonate platform : the Haftoman Formation of Central

Iran. *Facies*, *64*(2), 1–24. https://doi.org/10.1007/s10347-018-0523-6

Xu, W., Lithgow-Bertelloni, C., Stixrude, L., & Ritsema, J. (2008). The effect of bulk composition and temperature on mantle seismic structure. *Earth and Planetary Science Letters*, *275*(1–2), 70–79. https://doi.org/10.1016/j.epsl.2008.08.012

Yamato, P., Husson, L., Becker, T. W., & Pedoja, K. (2013). Passive margins getting squeezed in the mantle convection vice. *Tectonics*, *32*(6), 1559–1570. https://doi.org/10.1002/2013TC003375

Yang, T., Gurnis, M., & Zahirovic, S. (2016). Mantle-induced subsidence and compression in SE Asia since the early Miocene. *Geophysical Research Letters*, *43*(5), 1901–1909. https://doi.org/10.1002/2016GL068050

Zarrinkoub, M. H., Pang, K. N., Chung, S.-L., Khatib, M. M., Mohammadi, S. S., Chiu, H. Y., & Lee, H. Y. (2012). Zircon U-Pb age and geochemical constraints on the origin of the Birjand ophiolite, Sistan suture zone, eastern Iran. *Lithos*, *154*, 392–405. https://doi.org/10.1016/j.lithos.2012.08.007

Zhao, D. (2009). Multiscale seismic tomography and mantle dynamics. *Gondwana Research*, *15*(3–4), 297–323. https://doi.org/10.1016/j.gr.2008.07.003

Zhong, S., & Gurnis, M. (1992). Viscous flow model of a subduction zone with a faulted lithosphere: Long and short wavelength topography, gravity and geoid. *Geophysical Research Letters*, *19*(18), 1891–1894. https://doi.org/10.1029/92GL02142

Zhong, S., & Gurnis, M. (1994). Controls on trench topography from dynamic models of subducted slabs. *Journal of Geophysical Research*, *99*(B8), 15683. https://doi.org/10.1029/94JB00809

Zhong, S., Gurnis, M., & Hulbert, G. (1993). Accurate determination of surface normal stress in viscous flow from a consistent boundary flux method. *Physics of the Earth and Planetary Interiors*, *78*(1), 1–8. https://doi.org/https://doi.org/10.1016/0031-9201(93)90078-N

Zhong, S., Gurnis, M., & Moresi, L. (1996). Free-surface formulation of mantle convection—I. Basic theory and application to plumes. *Geophysical Journal International*, *127*(3), 708–718. https://doi.org/10.1111/j.1365-246X.1996.tb04049.x